ION BEAM MIXING AND ELECTROCATALYSIS OF PLATINUM-IRON ALLOYS

by

© MARK G. FERNANDES B.Tech.

A Thesis

Submitted to the Faculty of Graduate Studies

in Partial Fulfilment of the Requirements

for the Doctor of Philosophy

McMaster University

October 1986

ION BEAM MIXING AND ELECTROCATALYIS OF PLATINUM IRON ALLOYS

DOCTOR OF PHILOSOPHY (1986) McMASTER UNIVERSITY

(Materials Science and Engineering) Hamilton, Ontario.

TITLE: Ion Beam Mixing and Electrocatalysis in Platinum-Iron alloys.

AUTHOR: Mark G. Fernandes, B.Tech. (I.I.T. Kharagpur)

SUPERVISORS: Dr. D.A. Thompson

Dr. W.W. Smeltzer

NUMBER OF PAGES: xii , 181

ABSTRACT

The experimental work pertaining to this thesis can be divided into two parts: a) The study of the ion beam mixing process in the platinum-iron system and b) Electrocatalysis measurements on the mixed platinum-iron alloys. The ion beam mixing was studied using a 120 keV Fe^+ ion over a range of temperatures from 298 K to 523 K. A thin film of platinum was evaporated onto an oxide free substrate of iron to form a bi-layer sample. In order to check whether the interface was clean and oxide free, Auger electron spectrometry was used along with sputtering. The mixing was studied primarily using RBS. The TEM was also used to characterize the samples before and after mixing.

At low temperatures (<373 K), the mixing is very small and found to take place by collisional processes. At higher temperatures (>473 K) iron moves rapidly into the platinum. The activation energy for the platinum migration into iron was found to be ~0.5 eV. This suggests that the vacancy mechanism is operating above 423 K. The films produced by mixing at low temperatures are highly stressed and there are a considerable amount of twins formed. It was also found that the grain size increases witn dose and temperature.

The surface concentration of Pt in the mixed films is high ~90%. This results in an improvement of ~25% in the overvoltage for the ion beam mixed films compared to an iron electrode. Ion beam mixed films were found to be more stable than iron electrodes simply coated with films with an evaporated platinum layer. This appears to be the result of the improved adhesion between the platinum and iron as a result of the ion beam mixing process. For unmixed samples, an oxide layer is able to form on the iron surface at the platinum/iron interface, possibly because of cracks in the platinum layer, and this results in platinum pealing off the electrode leaving just the iron electrode.

ACKNOWLEDGEMENTS

I wish to thank my supervisors, Dr. D.A. Thompson and Dr. W.W. Smeltzer, for their continuous support and guidance throught the course of the research.

It has been a pleasure to work with Dr. J.A. Davies, whose comments and continued interest regarding this work have been invaluable.

I would also like to thank D.V Stevanovic and B. Diacon and B. McClelland for their help in running and maintaining the equipment.

INDEX

LIST OF FIGURES

CHAPTER 1

INTRODCTION

The major application of ion beams for the modification of materials is the processing of semiconductor devices. Typical doping concentrations are of the order of 10^{-4} to 10^{-1} at. %. The use of ion beams is increasingly being expanded to other technological applications. High dose implants of up to 10 atom percent can be used to modify the surface properties of metals; however this process has several practical disadvantages. In order to achieve the large doses (10^{18} atoms/cm^2) required, the currents produced by the implanters have to be very large. Also the maximum surface concentration of the implanted species is determined by the sputtering rate of the target material.

The ion beam mixing (IM) technique is a prospective way of circumventing the drawbacks inherent to the implantation process. In this technique the surface of a material is coated with a thin film of the alloying material (solute) to form a layered sample. An ion beam of sufficient energy, such that the ions penetrate through the surface film and into the substrate, is then directed onto the surface of the

sample. Using this technique, it is possible to produce a surface alloy of any desired composition. Typical doses required are only about 10^{15} to $5x10^{16}$. The parameters that determine the thickness of the evaporated solute are, the energy of the beam and the atomic numbers and masses of the beam and solute atoms.

The IM technique can also be used to produce metastable and amorphous phases which cannot be produced by the other processes. The alloyed region is usually a few hundred nanometers thick. By contrast, splat cooling techniques used to produce amorphous phases in some systems can produce alloys that are about 1 to 20 μm thick.

The purpose of this work is to study the IM process using platinum as the evaporated (solute) material and iron as a (solvent) substrate, and to explore the potential of forming a surface alloy that acts as a good electrocatalyst for the production of hydrogen. Platinum is known to be a good catalyst for the liberation of hydrogen in alkaline solutions, but any large scale industrial process involving platinum electrodes would be prohibitively expensive. By using IM to alloy the suface of iron with platinum it should be possible to produce a catalytically active surface behaving very much like platinum but at a much lower cost.

Chapter 2 deals with the theories of the atom relocation process via ion bombardment. Included in this section are the theories relating to the basic electrodic

process. In chapter 3 a brief review is presented of the literature in the fields of IM and electo-catalysis. Chapter 4 deals with the sample preparation and analysis techniques used in this work. The sequence of unit operations and the process conditions are listed.

The analysis and discussion of the experimental results are dealt with concurrently in chapter 5. There are several approaches used to obtain composition profiles from RBS spectra. In this work RBS spectra are simulated using a composition profile. The simulated spectra are then compared to the experimental data obtained. If the fit is not adequate, the initial composition profile is adjusted until the fit is acceptable.

Chapter 6 contains a brief summary along with some conclusions and suggestions for further work.

CHAPTER 2

PRINCIPLES OF ION BEAM MIXING AND ELECTROCATALYSIS

2.1 Atomic Collisions in Solids

2.1.1 Introduction

When an energetic atom enters a solid, it loses its energy to the atoms in the solid, finally coming to rest with a mean energy equal to the thermal energy associated with the atoms of the solid.

The first section deals primarily with the mechanisms of energy loss, and the spatial distribution of the energy deposition. There is also a section devoted to the theory of electrodic processes in electrolysis, and the mechanism of hydrogen liberation from alkaline solutions.

A solid contains atoms with their associated electrons. In a classical collision process, the nature of the collision is determined by the relative atomic numbers and masses of the bodies involved. The mathematical description of the collisions accordingly differs. The collisions are classified as nuclear (elastic) and electronic (inelastic) processes respectively. The mathematical uncoupling of the processes allows the partitioning of the energy loss into nuclear and electronic parts. The electrons in most mater-

ials have a high mobility and their displacement does not result in any permanent disorder. Energy deposited into nuclear processes produces changes to the structure and properties of the material involved. The partitioning of energy is applied in determining the extent of the damage produced.

The energy lost to the solid takes place through a number of randomly occuring binary collisional events. These are distributed over a volume surrounding the path taken by the incident atom. When the number of particles involved is large, a statistical description is used to characterize the spatial distribution of the energy deposition. This chapter presents the mathematical formalism developed by Lindhard and co-workers to describe the energy loss mechanisms and deposited energy distributions.

2.1.2 The binary collision

A solution to the problem of a binary collision between two atoms requires a determination of the scattering cross-section and the velocity vectors of the atoms after the collision. As the atoms or ions approach each other the resulting coulombic forces between them are responsible for the scattering process. Since the forces are mutual i.e. internal, the problem is one of scattering in a central force field.

A two body problem in the laboratory (L) frame,

can be reduced to an equivalent one body problem (Goldstein 1980) of scattering from a fixed center of force in the center of mass (G) frame of reference. It is assumed that the velocities of the atoms are such that relativistic effects are not important, and the atoms in the target are considered stationary.

A particle in a G frame will have a reduced mass M_0 given by

$$M_0 = \frac{M_1 \ M_2}{M_1 + M_2} \qquad (2.1)$$

where: the M's refer to the masses of the atoms and

the subscripts 1 and 2, in this chapter, refer to the projectile and target atoms respectively.

The equation for the orbit of a particle in a central force field is

$$\frac{d^2u}{d\theta^2} + u + \frac{1}{M \ v_0^2 \ p^2} \frac{dV(1/u)}{du} = 0 \qquad (2.2)$$

$$\text{where } u = \frac{1}{R}$$

where: R is the distance between the particles

p is the impact parameter (c.f.) fig 2.1a

V(R) is a function that defines the interaction potential which is given by

$$V(R) = (Z_1 \ Z_2 \ e^2/R \ ) \ U \qquad (2.2a)$$

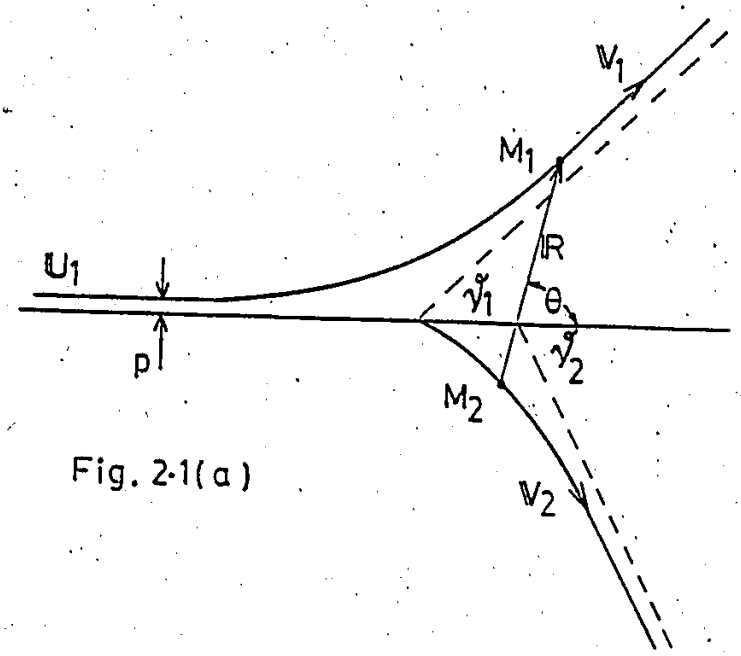

Fig. 2·1(a)

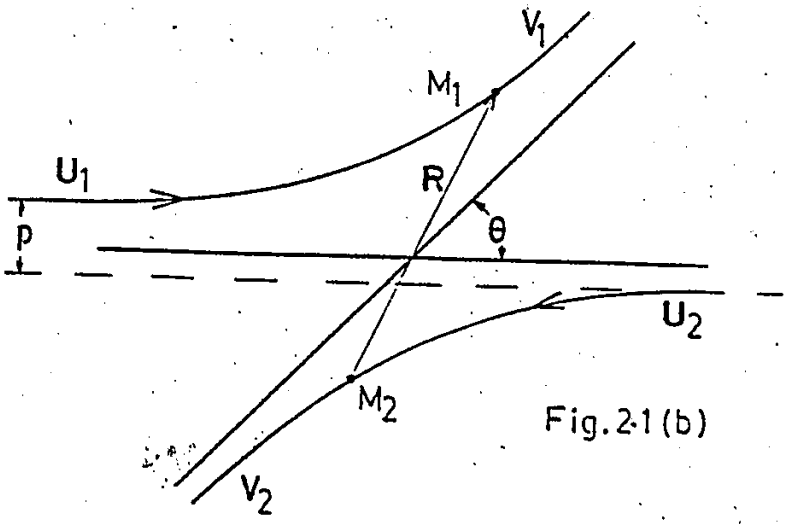

Fig. 2·1 (b)

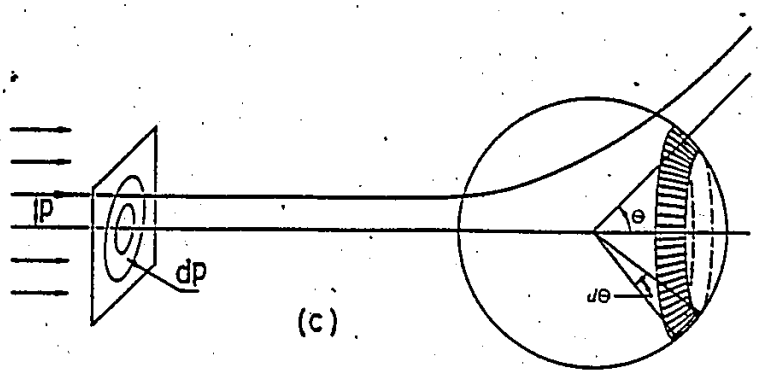

Figure 2.1 (a) Binary collision in the laboratory (L) system. (b) Binary collision in the center of mass (CM) system. (c) Scattering of an incident beam of particles by a center of force.

Bold letters are vectors in the CM system.

the Z's stand for the atomic numbers; e is the electronic charge; U is the screening function which has the property that U tends to unity as $R \to 0$, and must vanish as $R \to \infty$. $d\theta$ is the angle swept out by R in the G frame, and v is the velocity of the particle in the G frame.

The equation gives

$$\theta = \theta\ (Z_1,\ Z_2,\ M_0\ v^2,\ p/a) \qquad (2.3)$$

Using similarity properties and screened potentials (Lindhard et al. 1968), reduced the number of variables to two. These are commonly termed reduced variables.

$$\theta = \theta\ (\ \varepsilon,\ p/a) \qquad (2.4)$$

where: a is the Thomas-Fermi screening distance given by

$$a = 0.8853\ a_0\ (\ Z_1^{2/3} + Z_2^{2/3}\ )^{1/2}$$

and a_0 is the Bohr radius $\hbar^2/(me^2)$ and

$$\varepsilon = \frac{a\ M_0}{2\ Z_1 Z_2 e^2\ v^2}$$

If two collisions have the same value of ε and also the same value of p/a, then the collisions are similar, in the sense that the deflections are the same, and their orbits in space and time are identical when measured in reduced coordinates.

The differential cross-section given by

$$d\sigma = 2\pi\ p\ dp = 2\pi\ \sigma(\theta)\ \mathrm{Sin}\ \theta\ d\theta \qquad (2.5)$$

is such that a particle having an impact parameter between p and p+dp is deflected through an angle between θ and $\theta+d\theta$, Fig. 2.1c.

From equation (2.4) and (2.5)

$$d\sigma = \pi a^2 F(\epsilon, \sin \theta/2)\, d\Omega \qquad (2.6)$$

where: $d\Omega$ is the solid angle contained between θ and $\theta+d\theta$

Using perturbation theory, and extrapolating to a wide angle approximation, LSS showed that equation (2.6) could be reduced to an equation with one independent parameter t.

$$d\sigma = \frac{\pi a^2 dt\, f(t^{1/2})}{2\, t^{3/2}} \qquad (2.7)$$

where: $t = \epsilon^2 \sin^2(\theta/2)$

The function $f(t^{1/2})$ is plotted fig. 2.2. The wide angle extrapolation may introduce an error of about 10 percent. However, the simple formulation and the low probability of the wide angle scattering make this approximation attractive. Winterbon et al. (WSS) (1970) give a numerical approximation to the $f(t^{1/2})$ over its entire range by

$$f(t^{1/2}) = \lambda\, t^{1/6}\left(1 + (2\lambda\, t^{2/3})^{2/3}\right)^{-3/2} \qquad (2.8)$$

where λ is 1.309.

WSS also gave an approximation applicable over parts of the curve;

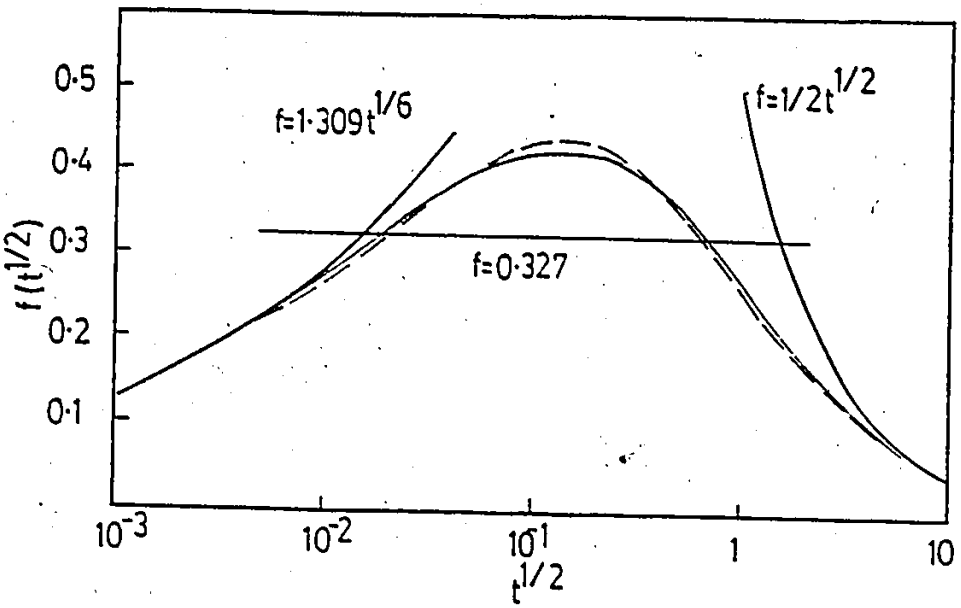

Figure 2.2 The universal scattering function, $f(t^{1/2})$ calculated from the Thomas-Fermi potential (continuous solid line). The numerical approximation to the $f(t^{1/2})$; equation 2.8 (dashed line). Power cross-section approximation equation (2.9) for m = 1/3, 1/2 and 1. (broken line)

$$f\,(t^{1/2}) = \lambda_m\, t^{1/2 - m} \qquad (2.9)$$

for: $t < 10^{-2}$ $\quad \lambda_{1/3} = 1.309$; $m = 1/3$

$10^{-2} < t < 1$ $\quad \lambda_{1/2} = 0.327$; $m = 1/2$

$t > 1$ $\quad \lambda_1 = 0.500$; $m = 1$

where m is the power in the interaction potential and $V(R) \propto R^{-1/m}$.

For large values of t, the ϵ is large, and the distance of nearest approach is small. The screening U in equation 2.2a is $\simeq 1$ as $R \to 0$ so that the potential can be taken as

$$V(R) = \frac{Z_1 Z_2 e^2}{R} \qquad (2.10)$$

With this substitution and equation (2.5), equation (2.2) can be solved to give the Rutherford cross-section in the G system.

$$\sigma(\theta) = \frac{1}{4}\left\{\frac{Z_1 Z_2 e^2}{2E}\right\}^2 \csc^4(\theta/2) \qquad (2.11)$$

The symmetry of the two body collisional process in the G frame, allows for a quick determination of the velocity vectors after the collision. Fig. 2.1a and 2.1b show the collisional process in the L frame and G frame respectively.

The velocity of the center of mass is given by

$$u_g = \frac{M_0 u_1}{M_2} . \qquad (2.12)$$

By subtracting u_g from the velocities in the L frame, the velocities of the atoms in the G frame are obtained as.

$$U_1 = \frac{M_0 u_1}{M_1} \qquad U_2 = u_g$$

From the law of conservation of energy and momentum;

$$U_1 = V_1 \quad \text{and} \quad u_g = V_2$$

$$V_1 = \frac{M_0 u_1}{M_1} \qquad V_2 = \frac{M_0 u_1}{M_2}$$

Using fig 2.3 these vectors may be converted to the L frame and the energy of the particles in the L frame can be determined (Goldstein 1980)

The energy of the scattered particle T is given by

$$T = \gamma E_1 \sin^2 (\theta/2) \qquad (2.13)$$

where: $$\gamma = \frac{4 M_1 M_2}{(M_1 + M_2)^2}$$

and E_1 is the energy of M_1 before the collision.

2.1.3 The stopping cross section

The stopping power of a material is the average energy lost per unit path length and is given by (dE/dR).

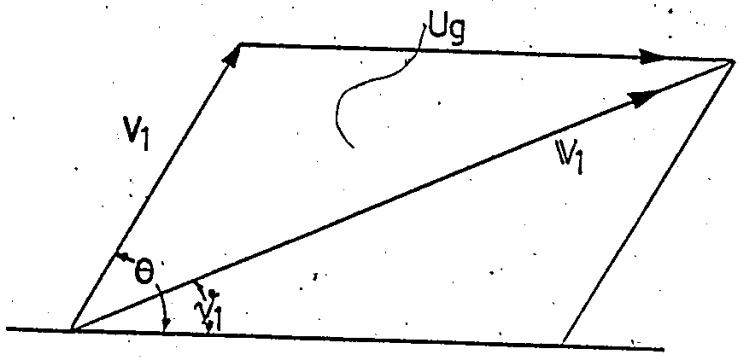

Figure 2.3 Vector diagram relating vectors in the center of mass and laboratory frames.

The stopping cross section (S) is the average energy lost per collision. If there are N atoms or scattering centers per cm^3, and T_m is the maximum energy lost per collision, then Lindhard et al. (1963), also called (LSS), give

$$\frac{dE}{dR} = N\,S = -\int_0^{T_m} T_{(n+e)}\, d\sigma \qquad (2.14)$$

where $d\sigma$ is the differential cross section for energy transfer $T_{(n+e)}$ to the nuclei and atomic electrons. The projectile loses energy to the nuclei and electrons in the target material. The energy lost to the nucleus alone is denoted by T. The stopping cross section (S) can be separated into nuclear (S_n) and electronic (S_e) parts.

The complete interaction between atoms is described by a screened Coulombic interaction containing elastic parts and a velocity dependent inelastic part. For low velocity high Z (atomic number) atoms, the energy lost to inelastic collisions is small. High velocity low Z atoms by contrast lose most of their energy to inelastic electronic excitations. The total stopping cross section (S(E)) is the sum of the nuclear and electronic parts:

$$S(E) = S_n(E) + S_e(E) \quad \text{and in} \qquad (2.15a)$$

reduced energy units (LSS)

$$S(\varepsilon) = S_n(\varepsilon) + S_e(\varepsilon) \qquad (2.15b)$$

The nuclear stopping cross section can be obtained as in WSS by substituting into equation 2.14

$$d\sigma = C\, E^{-m}\, T^{-1-m}\, dT \qquad (2.16)$$

where: $$C = \frac{\pi}{2}\, \lambda_m\, a^2 \left(\frac{M_1}{M_2}\right)^m \frac{Z_1\, Z_2\, e^2}{a}$$

and T is the energy transfered to the nucleus. With the aid of equation 2.9, this yields

$$S_n(E) = \frac{C}{1-m}\, \gamma^{1-m}\, E^{1-2m} \qquad (2.17)$$

Alternatively, in reduced coordinates, equation 2.7 can be substituted into equation 2.14 to yield

$$S_n(\varepsilon) = \lambda_m \frac{\varepsilon^{1-2m}}{2(1-m)} \qquad (2.18)$$

In the range where the projectile velocity $v \leq v_0\, Z_1^{2/3}$, the electronic stopping cross section is given by LSS as

$$S_e(E) = \xi\, 8\pi\, e^2\, a_0 \frac{Z_1\, Z_2}{Z^2} \frac{v}{v_0} \qquad (2.19)$$

where: $v_0 = \frac{e^2}{\hbar}$; $\xi = Z_1^{1/6}$; $Z^2 = \left(Z_1^{2/3} + Z_2^{2/3}\right)^{3/2}$

In terms of reduced parameters the electronic stopping is given by LSS as

$$S_e(\varepsilon) = k\, \varepsilon^{1/2} \qquad (2.20)$$

$$\text{where: } k = \frac{\xi \; (0.0793) \; Z_1^{1/2} \, Z_2^{1/2} \, (M_1 + M_2)}{/(\; Z_1^{2/3} + Z_2^{2/3} \;)^{3/4} \; M_1^{3/2} \; M_2^{1/2}}$$

The value of k is usually between 0.1 and 0.2, however for $Z_1 << Z_2$ it can take values larger than unity. Fig. 2.4 shows the stopping power for nuclear and electronic stopping in terms of reduced coordinates. Equation 2.20 gives S_e in terms of a monotonically increasing function of Z_1. However in practice S_e is known to oscillate with increasing Z_1 and has deviations that are as much as 20% from the value in equation 2.20.

2.1.4 The range and energy deposition distribution functions

The relative importance of the two energy loss mechanisms changes rapidly with energy, and the atomic numbers of the incident (Z_1) and target (Z_2) atoms. Nuclear stopping dominates at low energies and high Z_1 (implantation regime; $\varepsilon < 10$), whereas electronic stopping dominates at low Z_1 and high energies (analysis regime; $\varepsilon > 10$). In the regime of RBS analysis the energy deposited into nuclear processes is small; therefore, the technological importance of this regime in materials modification is reduced. High Z particles with energies in the range of tens of KeV to about 0.5 MeV are commonly used to modify the properties of

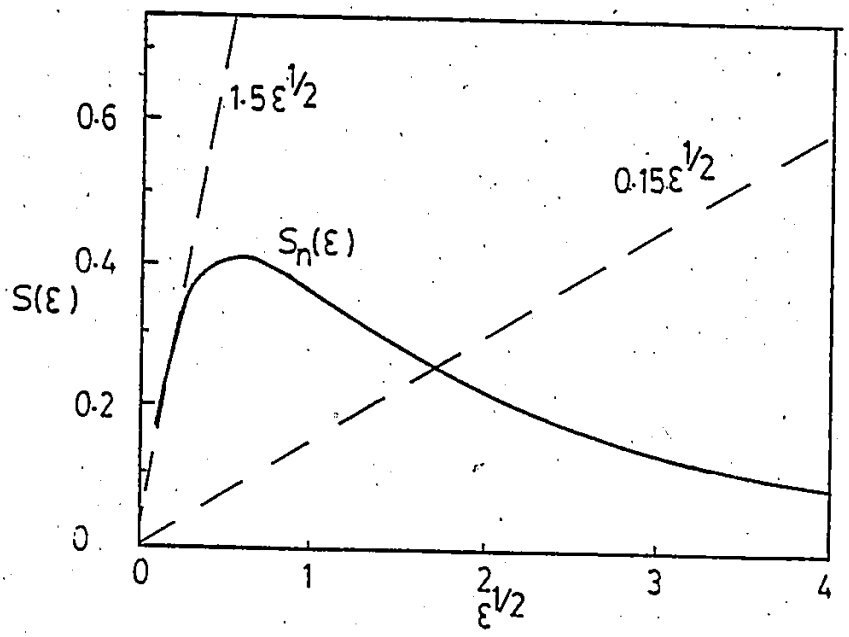

Figure 2.4 Nuclear S_n and electronic stopping functions in reduced units. Electronic stopping curves for k = 0.15 and 1.5.

materials.

There are two approaches commonly used to calculate the range and energy deposition distributions: 1) the unified range and energy relationships using a Boltzmann transport equation (LSS and WSS) or, 2) Monte Carlo techniques used to simulate atomic trajectories pioneered by Robinson and Oen (1962) and the more recent TRIM code developed by Ziegler et al. (1985). The first approach is described below and an outline of the approach used by the TRIM code is presented later on.

The LSS theory assumes that a projectile loses energy by a series of binary collisions with the target atoms. Correlation effects due to the ordered lattice are neglected and the atoms in the solid are assumed to be randomly distributed. Lindhard and Thomsen (1962) have shown that the energy deposited by the projectile (E) can be partitioned into nuclear (ν) and electronic (η) parts, so that

$$\nu(E) + \eta(E) = E \qquad (2.21)$$

The deposited energy or damage distribution function, $F(r,v)$, is defined (WSS) so that $F(r,v)d^3r$ is the average amount of energy deposited in the volume element (r,d^3r) after all recoiling atoms have slowed down beyond a certain energy limit, chosen such that, below this energy, the particle does not propagate any significant distance.

From the definition of energy conservation

$$\int \dot{F}(r,v)d^3r = E, \qquad (2.22)$$

the transport equation gives

$$F(r,v) = N|\delta r| \int d\sigma \; | \; F(r,v') + \bar{F}(r,v'') \; | + | \; (1 - N|\delta r| \int d\sigma) \; F(r-\delta r,v) \; | \qquad (2.23)$$

where v is the velocity of the incident atom

v' is the velocity of the scattered particle

v'' is the velocity of the recoiling atom

$d\sigma$ is the differential scattering cross section

and $N|\delta r| \int d\sigma$ is the probability of a collision in $|\delta r|$

Equation (2.23) states that the distribution function F, is a superposition of the probability of the occurence of a collisional event in space $|\delta r|$ around r, defined by F(r,v') for the projectile, and $\bar{F}(r,v'')$ for the scattered atom if a collision has taken place. If no collision has taken place, the particle moves a distance $|\delta r|$ and has the same velocity v.

The equation is formulated for a monoatomic medium characterized by Z_2 and N. It ignores scattering caused by the electrons of the medium; however because of their negligible mass the distribution will not be significantly affected. Even for high Z particles at KeV energies, a substantial fraction of the energy may be lost into electronic processes (~30%). By substituting $\nu(E)$ for E in equation (2.22), a normalization for nuclear processes can be

achieved.

Expanding the second term on the right of equation (2.23) and substituting $v/[v] = \delta r/[\delta r]$ we obtain;

$$\frac{-v}{|v|}\frac{\delta}{\delta r}F(r,v) = N\int d\sigma \left[F(r,v) - F(r,v') - \xi \bar{F}(r,v'') \right] \qquad (2.24)$$

$\xi = 0$ for range distributions; $\xi = 1$ for damage distributions.

In terms of the depth x, (Fig. 2.5) and energy E, equation (2.24) becomes

$$-\cos(\theta)\frac{\delta F}{\delta x} = N\int d\sigma \left[F(x,E,\theta) - F(x,E',\theta') - \xi \bar{F}(x,E'',\theta'') \right] \qquad (2.25)$$

By using Legendre polynomials the angular variable can be eliminated (WSS). Taking moments in x the equation can be reduced to a single variable E. The n^{th} moment in x is given by;

$$\langle x^n \rangle = \int x^n F(x,E) d^3x \qquad (2.26)$$

Winterbon (1975) has solved equation 2.25 using the (T-F) model of the atom and the power law approximation. The solution gives the moments in the cascade in terms of a factor E^{2m}, where m is the power law exponent. The first four moments for several projectile-target combinations, having mass ratios (M_2/M_1) between 0.1 and 10.0, have been tabulated. A procedure to interpolate between the mass

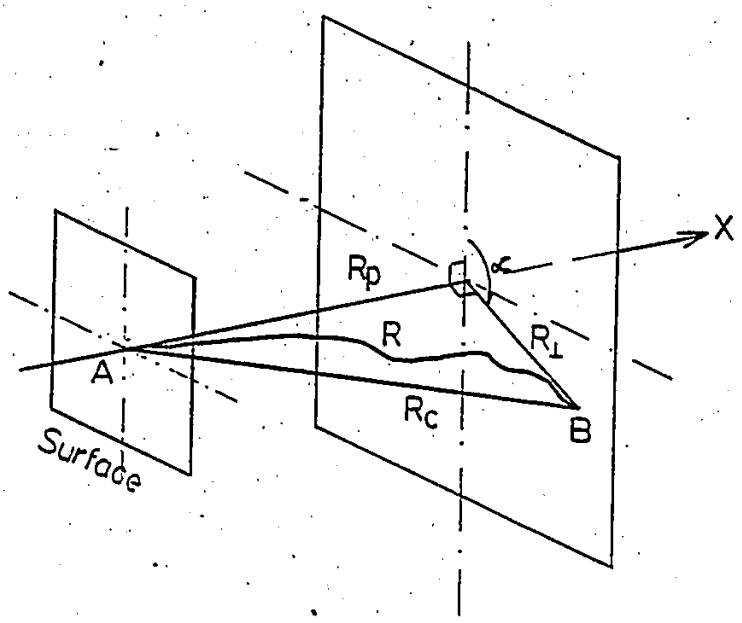

Figure 2.5 The particle enters the solid at A and comes to rest at B. The sketch illustrates the concepts of the Range R, the path range R_p, the chord range and R_c and the range perpendicular to the direction of the beam $R_\perp$.

ratios for any projectile-target combination is outlined.

In theory one would require an infinite number of moments to construct a distribution; however for distributions that are near Gaussian the first four moments generally suffice. Single variate distributions can be constructed from a limited number of moments using the Pearson or Edgeworth formalism (Kendall 1969). Baroody (1965) has shown that the Edgeworth expansion is sufficiently accurate to plot the distributions of KeV ions in solids. The Edgeworth series for a projectile injected normal to the target in the x direction is givin by

$$F(x,E) = \frac{\tilde{g}}{2\,\pi^{1/2}\,\mu_2^{1/2}} \exp\left(\frac{-z^2}{2}\right) f(z); \text{ where}$$

$$f(z) = 1 - \left(\frac{\mu_3}{6\,\mu_2^{3/2}}\right)\left(3z - z^3\right) + \frac{1}{24}\left(\frac{\mu_4}{\mu_2^2} - 3\right)$$

$$\left(3 - 6z^2 + z^4\right) - \left(\frac{\mu_3^2}{72\mu^3}\right)\left(15 - 45z^2 + 15z^4 - z^6\right)$$

$$\text{and } z = \frac{x - \langle x\rangle}{\mu_2^{1/2}} \qquad \text{where } \mu_n = \langle \left(x - \langle x\rangle\right)^n \rangle$$

and $\langle x\rangle$ is the mean of the distribution function having variance μ_2; skewness $\mu_3 / \mu_2^{3/2}$ and kurtosis μ_4 / μ_2^{2} ; and $\tilde{g} = 1$, for range, $\nu(E)$ for damage and $\eta(E)$ for ionization.

The distributions intersect the surface (ordinate) at a non zero value. Fig. (2.6a and 2.6b) show the range and

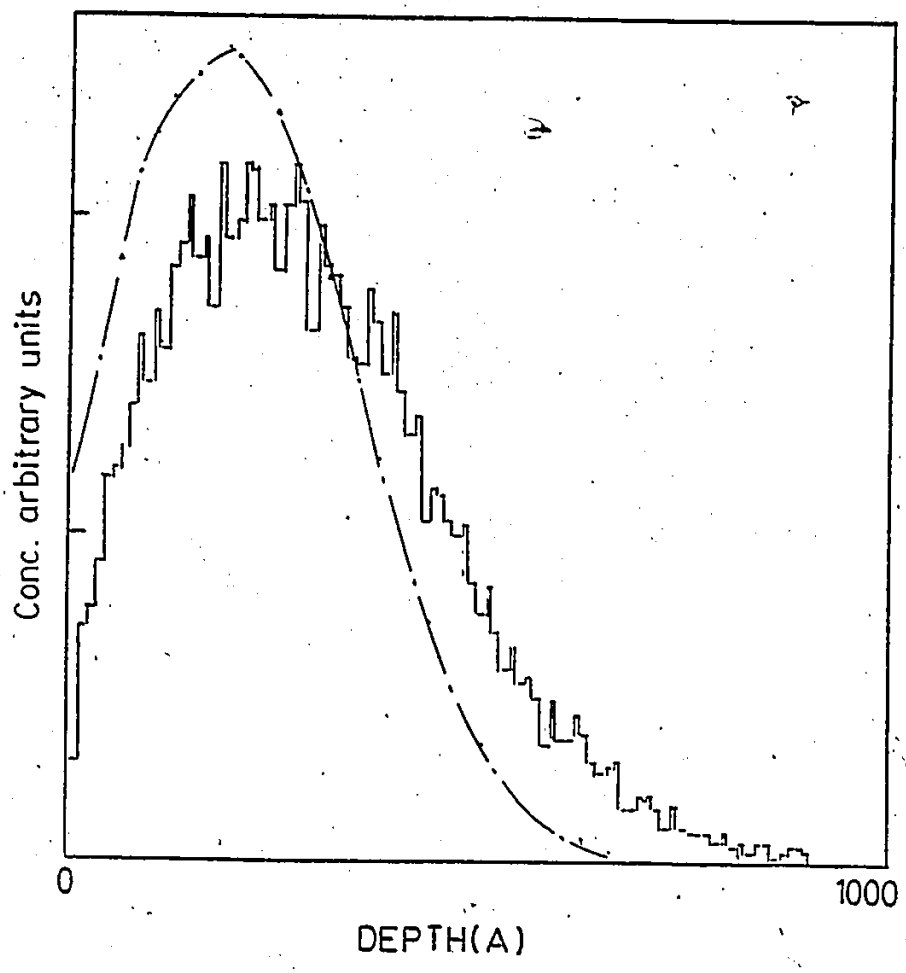

Figure 2.6 (a) Range of 120 keV Fe^+ calculated using equation (2.25) and (2.26) (Winterbon 1975) (broken line), and using the TRIM code (solid line) Ziegler et al. (1975).

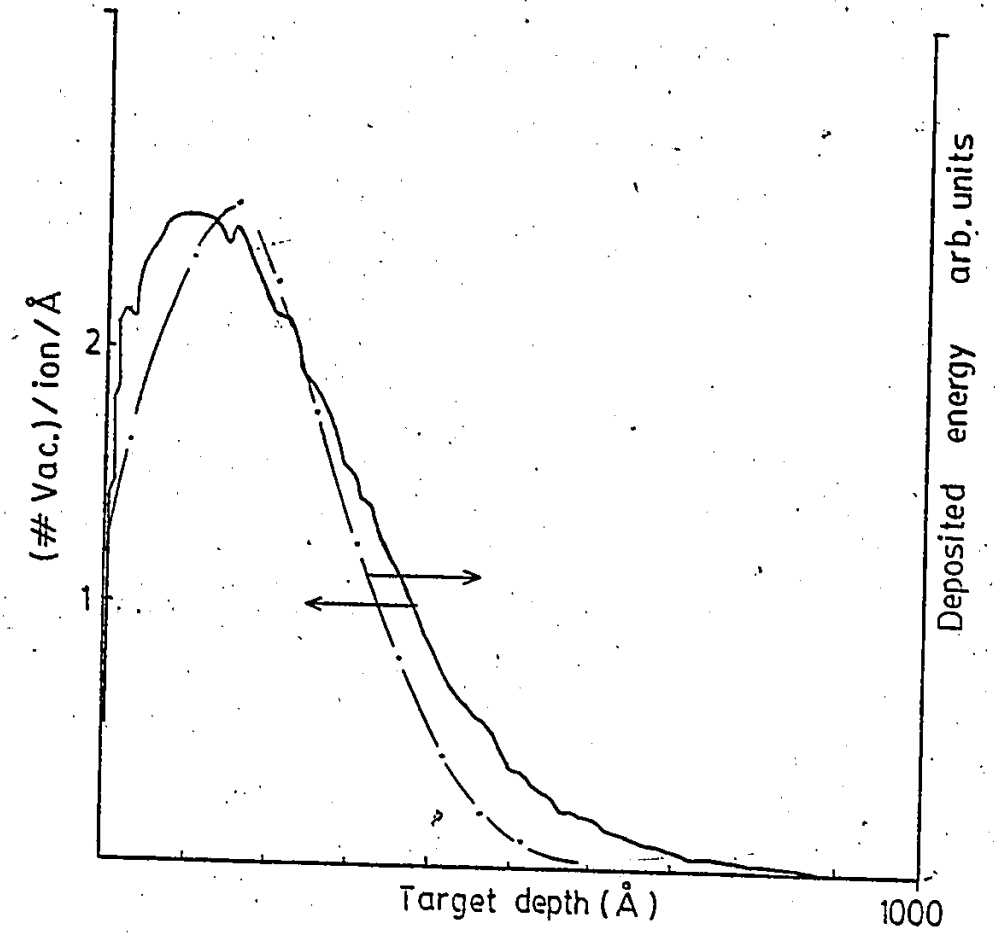

Figure 2.6 (b) Energy deposition distribution function calculated using equation (2.25) and (2.26) (Winterbon 1975) (broken line), and the damage profile generated using the TRIM code (Ziegler et al. 1975) (solid line).

damage distributions for 120 KeV Fe^+ in platinum. If the gaussian (broken line) were extrapolated before the surface, the area enclosed would represent the number of reflected Fe^+ fig. (2.6a) and the energy related to the backscattered or sputtered ions fig. (2.6b). In the calculation, there is no bar to allowing a particle to move back and forth across the surface; however in an experiment any particle moving out of a solid can not move back into it again. Hence the area at negative depths is expected to be larger, while the value of the distribution at the surface will be smaller. Surface corrections developed are believed to be inaccurate (Bottiger et al 1971). A fundamental difference between the range and damage distributions is that, for a single particle the range is a delta function, and the damage is distributed over the ion track. The calculations done above are averaged over an infinite number of trials and bear little resemblance with a single cascade.

The accuracy of the moments calculated is subject to discussion. Approximations used in the generation of the moments cause an inaccuracy of~ 1% (Winterbon 1975) for the mean range, and the inaccuracy is doubled for sucessive moments. The inaccuracies introduced by interpolation can be rather severe. If the straggling is .01 times that of the tabulated value for a particular case, and it has a error of 1%, then the interpolated straggling would have an error of 100%. The interpolated damage distributions are less accurate than those for the range, as the mass values affect the

ratio of the electronic (η) and the nuclear (ν) stopping. In the region where the electronic stopping is proportional to $E^{1/2}$, and the target is truly random, an inaccuracy of 10% is expected.

LSS have solved an equation similar to 2.23 and have compared their results to the experimentally measured ranges of Davies et al. (1960) and Davies and Sims (1961). At higher energies the theory matches the experimental results closely. At low energies the experimental ranges are greater than those theoretically predicted; however, the higher experimental ranges are believed to be a result of channeling.

Computers can be used to simulate projectile trajectories in solids using Monte Carlo techniques. The advantage of this technique over the analytical formulations is that the elastic scattering can be treated rigorously, and that surfaces and interfaces can be dealt with explicitly. The accuracy of the results depends on the scattering potentials used. The ranges of a large number of particles must be simulated in order to develop sufficient statistics. Fig. (2.6b) shows the range and damage distributions calculated by the TRIM program (Ziegler et al. 1975). The target is assumed to be amorphous. The "histories" of a large number of individual particles are followed until the energy of each particle reaches a specified value or the particle leaves the target. The projectile changes direction and

loses a discrete amount of energy as a result of binary nuclear collision; between collisions, the particle moves in straight free flight path, continuously losing energy by inelastic electron excitations. The TRIM code uses accurate analytical formulations for the scattering integrals which result in considerable computation saving.

There are several criteria that can be used to study the displacement of atoms in a solid. The next section examines how an appropriate choice from these criteria can yield values that echo reality.

2.1.5 The number of displaced atoms

The defects produced in solids, by charged particle irradiation, are caused by the coulombic interaction between the projectile and target atoms. Atoms displaced directly by the projectile atom are called primary knock-on atoms (pka). The fraction of defects produced as a result of pka's is small, and most are produced at the end of the trajectory. The primary atoms go on to produce successive generations of collisions; these are collectively referred to as a collision cascade.

The majority of the defects resulting from the cascade are produced by atoms with an energy a few times that of the displacement energy. Consequently, the resulting interstitials are usually only a few interatomic spaces away from the vacancy created. Most of the displaced atoms are

not homogeneously distributed, but tend to be clustered into small subcascade regions. The interstitial vacancy pairs are called Frenkel defects or i-v pairs. The important factors in the formation of i-v pairs are the threshold displacement energy (E_d), and the recombination radius (r_v). Both factors depend on the nature of the solid and are anisotropic: r_v is also dependent on the temperature of the solid. In metals E_d can vary from about 12 to 80 eV, depending on the metal and lattice direction. The average is usually taken to be about 25 eV (Kinchin and Pease 1955). Assuming that r_v is isotropic at room temperature in metals, r_v is ususlly taken to be about 1 nm.

The approach used by Kinchin and Pease (1955) to determine the number of displaced atoms per ion assumes a coulombic interaction with a sharp cutoff at the T-F screening radius. For impact parameters greater than the T-F screening radius, a hard sphere collision is assumed. Further, only atoms with an energy greater then $2E_d$ are presumed to create additional displacements. Atoms with energies between E_d and $2E_d$ can be displaced but cannot further increase the number of displaced atoms. Using such a formalism the number of atoms displaced (N_d) is given by

$$N_d = \frac{E}{2\,E_d} \qquad (2.28)$$

The assumptions made in obtaining (2.28) tend to overestimate the number of displaced atoms. Sigmund (1969)

uses a transport equation similar to (2.23)

$$0\int^{E} d\sigma\, dT[(F(E,E_0) - F(E-T,E_0) - F(T-U,E_0) - \delta(T-E_0)] = 0 \qquad (2.29)$$

where U is the binding energy of an atom to its lattice site and T is the energy transfered as a result of the collision. Equation (2.29) holds for elastic collisions, so that, by replacing E with $\nu(E)$, the energy deposited into inelastic events is ignored. Using the power approximation the number of displaced atoms is given by

$$N_d(E) = \int_{E_d}^{E} E\, dE_0\ \ F(E,E_0) \qquad (2.30)$$

Equation (2.30) has been evaluated by Sigmund (1969) using m=0 in the power approximation to yield

$$N_d(E) = \frac{6}{\pi}\ \frac{E}{U}\ \ln\left(1 + \frac{U}{E_d}\right) \qquad (2.31)$$

In semiconductors: $U = E_d$ where E_d is taken as $4E_b$; E_b is the binding energy; then

$$N_d(E) = \frac{0.42\ \nu(E)}{E_d} \qquad (2.31a)$$

In metals where U is only a few eV, and negligible compared to E_d, (2.30) yields

$$N_d(E) = \frac{0.61\ \nu(E)}{E_d} \qquad (2.31b)$$

This is an upper limit to the number of atoms

displaced. In heavy metals the defect densities may become larger than the stability limit determined by the recombination volume (r_v). In such an oversaturated cascade the number of surviving defects is determined by the volume associated with the primary damage. Athermal and subthreshold (Wollenburger 1968) recombinations will reduce the number of defects calculated using (2.31). Quantitative information on the extent of recombination in dense cascades is not available.

Robinson (1974) has simulated such cascades using Monte Carlo techniques. This approach is superior to the analytical approaches used above in that the effects of crystal structure are included, and more realistic atomic scattering laws can be used. The cascades can also be simulated using different criteria for defect formation and recombination. A formulation similar to (2.28) is used;

$$N_d(E) = \kappa \frac{\nu(E)}{2 E_d} \qquad (2.32)$$

where κ is defined as the displacement effiency.

Simulations in Au, Fe and Cu give a value of $\kappa \equiv 0.86$. This is about 30% below the value obtained in (2.31b), the difference is largely attributed to the effect of replacement collisions. The introduction of a recombination volume r_v can bring about severe changes to the values calculated by the above formulation. Cascades simula-

ted upto 10 KeV recoils indicate that the E_d may be linearly dependent on N(E): i.e.

$$\frac{\nu(E)}{N_d} = \alpha + \beta \nu(E) \qquad (2.33)$$

the α and β are empirical constants (and are positive).

Equation (2.33) suggests that as $\nu(E)$ increases the E_d increases, which is contrary to physical expectancy. It is believed that in low energy high Z cascades there may be some overlap between the various branches of the cascade increasing the number of spontaneous recombinations. At higher energies the cascade volume increases as E^2. It is expected that the effect of athermal recombination will be reduced at the beginning of the trajectory as the subcascades are separated, and recombinations due to subcascade overlap will be limited to the end of the trajectory.

From the perspective of IM studies, it would be useful to determine the fraction of displaced atoms undergoing small-distance relocation as a result of nuclear collisions in a cascade to the number of surviving defects that participate in longer-distance atom relocation. Equation (2.32) is useful in calculating the total number of displaced atoms; however, the values calculated by (2.33) are the number of surviving defects that would be associated with a longer range diffusive type relocation. By using a combination of binary collision (BC) scattering events as in

the TRIM program, and applying molecular dynamic (MD) considerations to the lower energy recoils (< .1 KeV), where many-body collisions are important, realistic cascades can be generated and the extent of short range relocation determined. MD can then be used in a manner similar to Jacucci (1984) and Murch and Rothman (1984) to study atom relocation distances for the surviving defects in the cascades produced. The numbers obtained by such studies would be useful in understanding the IM process.

2.2 Ion Beam Mixing

2.2.1 Introduction

Ion beam mixing (IM) is a process of atom relocation in a solid, as a consequence of irradiation with an ion beam. There are several mechanisms by which atoms can relocate under the influence of an ion beam. These are contiguous with the times involved in the relocation process (Matteson and Nicolet 1983).

A KeV ion in a solid comes to rest in about 10^{-13} s. The collision cascade set up by the projectile lasts for about 10^{-12} s. This period forms a temporal benchmark for defining the "prompt regime". The IM processes in this regime are as a result of the motion gained through nuclear collisions. Atoms displaced by collisions between projectile and target atoms usually have a high energy, and are disp-

laced in the net direction of the beam. This atom relocation process is called recoil mixing. Atoms displaced by collisions between host atoms in a cascade are assumed to be randomly directed, and have energies of the order of a few times the displacement energy. The mixing resulting from this process is called cascade mixing. The atom relocation processes in the prompt regime are collectively referred to as ballistic mixing.

Processes occuring in time scales between 10^{-12} seconds and a few minutes fall into the "delayed regime". These are thermally activated, and have a relocation length that depends on the sink density. The defects may be classified as mobile or immobile, depending on the temperature. The mobile defects annihilate at sinks; some defects may associate to form metastable and immobile defect complexes. Thermodynamic forces play an important role in defect migration and atom relocation. The process of atom relocation in this regime is called radiation enhanced diffusion.

The microstructural damage and chemical changes caused by the ion beam would leave the material in a higher energy state. These long lasting effects belong to the "persistent regime".

2.2.2 Ballistic mixing

Ballistic mixing in solids has generally been modelled by calculating the number of atoms set in motion using damage theory, and estimating the mean relocation

distance from the range of the struck atom in the cascade, or using a thermal diffusion like model.

Using the mean energy of the projectile in the layer, and a minimum cut off energy transfered to the recoiling atom; the number of atoms crossing the interface D can be calculated (Nelson 1969) as;

$$D(E,E_0) = \frac{4\pi a_0^2 D N E_R Z_1 Z_2 M_1 \Phi}{(M_I + M_2)(Z_1^{2/3} + Z_2^{2/3})^{1/2}} X$$

$$\left[\frac{1}{E_2^2} - \frac{1}{\tilde{E}_r^2} \right] \qquad (2.34)$$

where $\tilde{E}$ is the maximum energy transferable, D is the interatomic spacing and Φ is the fluence.

This approach yields an upper limit to the number of recoil implanted atoms. For $5x10^{15}$ Fe^+ ions at 120 KeV, D is found to be about 10^{15} atoms in (2.34). When spread over a distance given by the range of the struck atoms, this concentration is found to be very small and is barely detectible by RBS.

Sigmund (1972) has derived an expression for the flux of moving particles (H) in a random homogeneous medium. The expression gives

$$H\, dE\, d\Omega = \frac{3}{2\pi^3} \frac{\eta}{E^2} \frac{F_D(E_i, \eta_i, x)\, dE\, d\Omega}{N C_0} \qquad (2.35a)$$

where $F_D(E_i, \eta_i, x)$ is the distribution function for the deposited energy of a projectile with initial energy E_i at an angle η_i to the surface, η_i is the direction cosine of the velocity of recoils at a depth x, $d\Omega$ is an elemental solid angle around E, and $C_0 = \lambda_0 a_0^2/2$ where $\lambda_0 = 24$ and $a_0 = 0.219$ Å. H has a velocity spectrum that goes as E^{-2}. Fisher (1978) assumes that there is a potential barrier U_{pb} at the planar interface between the metals; he uses the following expression to calculate the flux of particles (H) recoil implanted from the surface film,

$$H\, dE\, d\Omega = \frac{3}{2\pi^3 (E + U_{pb})^3} \frac{nE}{N C_0} \frac{F_D(E_i, \eta_i, x)\, dE\, d\Omega}{} \qquad (2.35b)$$

The depth distribution of the recoiled species, given by H dE dΩ can be regarded as an implantation source function and each recoil from the film will possess a range probability function for slowing down given by $F_R(E,\eta,x)$. The distribution n(x) can now be expressed as

$$n(x) = \int \int H\, F_R(E, \eta, x)\, dE\, d\Omega \qquad (2.35c)$$

where $d\Omega = 2\pi \sin\theta\, d\theta$ and $\eta = \cos\theta$ where θ is the angle between the normal to the interface and the velocity vector. A solution of (2.35c) requires the distribution functions, and methods of numerical integration.

The number of atoms involved in cascade mixing is very large. About 1000 atoms are displaced by a single 120

KeV Fe^+ ion. Most of these move only a few atomic spaces away from their lattice sites. In platinum an interstitial would have to move away about 1 nm. (a radius encompassing about 48 atomic volumes) to avoid athermal recombination (Wollenberger 1968).

There have been several attempts to calculate the composition profiles produced by cascade mixing. Many of these deal with the loss of resolution caused by the spreading of markers in SIMS and Auger profiles. Sigmund and Grass-Marti (SGM) (1981) have formulated a relocation function to calculate the spreading of thin buried markers. The varience (σ) is given by

$$\sigma = \frac{1}{3} \Gamma_0 \frac{F_D}{N} \xi_{12} \frac{R_c^2}{E_c} \Phi \qquad (2.36)$$

where $\Gamma_0 = 0.608$; $F_D(x)$ is the energy deposited per unit depth, $\xi_{12} = 4 M_1 M_2/(M_1 + M_2)^2$, E_c is the threshold displacement energy, and R_c^2 is the mean square range associated with E_c. The variance calculated by the SGM formulation is found to be about a factor of 3 less than the values obtained in low temperature experiments. Moller (1986) has used a computer code similar to TRIM to calculate the spreading of a platinum marker in silicon. The program was run for 300 KeV Xe^+ and a dose of 2×10^{16} ions/cm^2. It took ~5 hours on a CRAY 1 computer to generate a profile of

the marker. The result was found to be in close agreement with experiment. It is believed that the lack of the inclusion matrix recoils in the spreading of the marker is responsible for the low values obtained by the SGM theory.

Collins (1985) has used the SGM relocation function, and formulated an equation to calculate the distribution of an extended evaporated layer. His equation has no analytical solution, and numerical integration is required to generate the composition profiles.

Haff and Switkowski (1977) calculated a value of cascade "ballistic diffusion" (D_B) using a phenomenological approach. They assume that, during the cascade process, the atoms are similar to those in a gas with a randomly directed mean speed. The approach gives

$$D_B = \frac{l\ d}{N\ E_d} \left(\frac{dE}{dx}\right) \Phi \qquad (2.37)$$

where l is the interatomic spacing

d the width of the cascade and Φ is the fluence.

Myers (1980) uses a thermal diffusion-like model for cubic solids and gives

$$D_B = \frac{\lambda^2}{6} P(x) \qquad (2.38)$$

where λ is the RMS separation for i-v pairs and P is the Kinchin-Pease relationship given by

$$P(x) = \frac{0.8}{2 N E_d} \left(\frac{dE}{dx} \right)_n \Phi$$

It should be noted that equations (2.37) and (2.38) give a linear relationship with dose rate. For a 120 Kev Fe^+ beam at 1 μA on Pt, equation (2.37) gives $D_B = 6.6 \times 10^{-15}$ cm^2/sec. The corresponding value using (2.38) is 6.8×10^{-15} cm^2/sec.

Averback (1986) caried out experiments on the Cu-Mo, Cu-Nb and the Cu-Bi systems at 6 K and 295 K. Mo and Nb have similar masses and ballistic effects would predict the same amount of mixing at 6 K. However the amount of mixing in the Cu-Mo system is less than that in the Cu-Nb system. It should be noted that the heats of mixing of the two systems vary considerably. The Cu-Mo system has a large positive heat of mixing, and the Cu-Nb system has a very small positive heat of mixing. At 295 K the amounts of mixing in all three systems are less than even at 6 K, indicating that a diffusive process may be acting to cause demixing.

Bottiger et al. (1983) caried out experiments of ion beam mixing of buried platinum layers in iron. His results suggest that interstitial atoms contribute to mixing above 20 K.

The applicability of the formulations for ballistic mixing are extremely limited. They find some credence at very low temperatures, below which all diffusion related phenomena are "frozen" out. However, as evidenced by Aver-

back, even at 6 K ballistic effects alone are insufficient. The inclusion of the thermodynamic properties of the materials is necessary.

Manning (1984) uses a Boltzmann transport equation to calculate D_B. His result is similar to that obtained by Haff and Switkowski (1977). Manning suggests that, by using an appropriate E_d for each species in a target, chemical effects could be incorporated into cascade mixing. The energy deposited into nuclear processes can be partitioned between the various species in the target. However, the cross section for energy deposition varies monotonically with atomic number, which is not congruent to chemical effects.

2.2.3 Radiation enhanced diffusion

It is generally accepted that substitutional atoms in a metal diffuse via the thermally activated motion of equilibrium vacancies with a diffusion coefficient that is proportional to the concentration of these defects. The number of vacancies depends on the thermodynamic properties and temperature of the metal. Under irradiation by an ion beam, the number of defects produced is in excess of the equilibrium number; these defects are mostly interstitials and vacancies. The defects may be classified as mobile or immobile depending on the temperature. Mobile defects diffuse and anneal at sinks. The sinks are immobile point defects, dislocations, grain boundaries, or the external

surface.

A system of equations linking the production and annihilation rates of point defects may be set up. This treatment assumes that the major contribution to radiation enhanced diffusion is caused by the presence of simple point defects.

$$\frac{dC_v}{dt} = K_0 - K_{iv}C_iC_v - K_{sv}S\,C_{sv} + D_v\nabla^2C_v$$

$$\frac{dC_i}{dt} = K_0 - K_{iv}C_iC_v - K_{si}S\,C_{si} + D_i\nabla^2C_i \qquad (2.40)$$

where: $C_{v,i}$ are the volume concentrations of interstitials, vacancies, S is the number of fixed sinks per unit area, K_o is the production rate of Frenkel pairs per unit time, K_{vi} is the rate term for recombination of Frenkel pairs, $K_{sv,i}$ is the sink strength for vacancies = interstitials, and $D_{v,i}$ is the diffusion coefficient of vacancies, interstitials. The last term is needed to take into account diffusion to extended sinks which are usually internal or external surfaces. The production rate of surviving Frenkel defects in a dense cascade is extremely difficult to quantify. The number of Frenkel pairs formed can be calculated from the Kinchen-Pease theoretical equation (2.28). However a formulation like equation (2.33) would be more appropriate.

The recombination term given by Wait (1957), is

$$K_{iv} = 4 \pi r_{iv} \left(\frac{D_i + D_v}{\Omega} \right) \qquad (2.41)$$

and the sink strength is given by

$$K_{sv,i} = 4 \pi r_{sv,i} \left(\frac{D_{v,i}}{\Omega} \right) \qquad (2.42)$$

where Ω is the atomic volume. The time to reach steady state is given by Lam (1975) as

$$\theta = \frac{1}{2\nu(K_{sv} S)} \qquad (2.43)$$

Equation (2.40) can be solved analytically under certain conditions. In regions far away from the surfaces, the last term vanishes. In the steady state, where the rate of removal of vacancies and interstitials is the same, then

$$D_v C_v = D_i C_i \qquad (2.44)$$

and equations (2.40) can be solved to give

$$C_v = \frac{K_{si} S}{2 K_{iv}} \left[\frac{-1 + (1 + 4 K K_{iv})^{-1/2}}{K_{sv} K_{si} S^2} \right] \qquad (2.45)$$

$$C_i = \frac{D_v C_v}{D_i} \qquad (2.46)$$

The diffusion coefficient under irradiation D_{irr} is given by

$$D_{irr} = F_v C_v D_v + F_i C_i D_i \qquad (2.47a)$$

where F_v and F_i are constants, and under steady state conditions

$$D_{irr} = (F_v + F_i) C_v D_v , \qquad (2.47b)$$

where F_v and F_i are constants.

When mutual recombination is the dominant mechanism for the annihilation of defects ($S = 0$), the diffusion coefficient is given by

$$D_{irr} = (F_v + F_i) \frac{K_0 K_{si}}{(K_{iv} K_{sv})^{1/2}} . \qquad (2.48)$$

When annihilation at fixed sinks is the dominant mechanism for removal of defects, the diffusion coefficient is given by

$$D_{irr} = (F_v + F_i) \frac{K_0 D_v}{K_{sv} S} \qquad (2.48)$$

It is worth noting that, for annihilation to fixed sinks, the relationship between D_{irr} and dose rate is linear.

2.2.4 The influence of thermodynamic properties on the rates of mixing

Cascade theory predicts that the rates of IM carried out on bi-layers with similar atomic sizes are expected to be similar. Experiments carried out by Westendorp et al. (1981) and Johnson et al. (1985) on metallic systems having

similar atomic sizes show rates of mixing that vary considerably. Johnson's experiments at 77 K showed that the inclusion of thermodynamic properties in the prompt regime (PR) is necessary for predicting the rates of mixing. Delayed effects which are of a diffusive type often result in thermodynamically stable structures. The phases produced by mixing in the prompt regime are either stable or metastable and are thought to result from the fast quenching of atoms in the collision cascade.

A semi-empirical formulation developed by Johnson uses the heats of mixing (ΔH_m) and the cohesive energy (ΔH_{coh}) to predict the rates of mixing. The ΔH_m tends to bias the random mixing process in a way similar to Darken's analysis for chemical interdiffusion. Using the approximation of regular solutions, one can write

$$\tilde{D} = \tilde{D}^0 \left[1 + \frac{d\ln \gamma}{d\ln C_A} \right] = \tilde{D}^0 \left[1 + \frac{2\delta H_m}{k_B T} \right] \quad (2.50)$$

where $\delta H_m = 2\,\delta\, C_a C_b$ and $\delta = Z \left[V_{AB} + (V_{AA}+V_{BB}) \right] / 2$.

The V's represent the potential energies of interaction of the respective pairs and Z is the co-ordination number.

Experiments done on systems having $\Delta H_m \cong 0$ show that the rates of mixing are related to the cohesive energy and can be given by the following relationship.

$$\frac{4 D t}{\Phi} \alpha \left(\Delta H_{coh} \right)^{-2} \qquad (2.51)$$

Using (2.50) and (2.51) Johnson et al. give the following relationship for the rates of mixing.

$$4 D t = \frac{K_1 \varepsilon^2}{\rho^{5/3} \Delta H_{coh}^2} \left[1 + \frac{K_2 \Delta H_m}{\Delta H_{coh}} \right] \qquad (2.52)$$

where K_1 and K_2 are empirical constants equal to .037 and 27 respectively, ε is the energy deposited per unit path length, and ρ is the atomic density.

The expression (2.52) is useful in determining the rates of mixing in the PR. In the delayed regime (DR) the rates of mixing for a system having a negative ΔH_m will be higher due to the additional diffusive biased motion. The rates of mixing in the DR are proportional to the concentration and mobility of the point defects.

The transport of atoms under point defect (interstitial and vacancy) gradients is extremely complex. Howard and Lidiard (1965) have shown that an impurity which is strongly bound to a vacancy moves in the same direction as the vacancy flux. However, for weak interactions between impurities and vacancies, and where vacancy exchanges with the host atoms are large, the impurity atoms move up the vacancy gradient. Johnson and Lam (1976) attempted to study the flux of solute atoms under the influence of interstitial and

vacancy gradients. They suggest that the sense of motion of solute atoms is related to the binding interactions between solute atoms and defect fluxes; however, their treatment is exceedingly complex.

2.3 The Electrolysis of Water in Alkaline Solutions

2.3.1 Introduction

The production of hydrogen by the electrolysis of water is an industrial process. The basic electroytic cell consists of a pair of electrodes immersed in a conducting electrolyte, which is dissolved in water. A membrane, which should be stable in the electrolyte, is used to separate the electrodes. A d.c. power supply is used to drive the cell. Because the cell has no moving parts, it is reliable and trouble free. Industrial cells require a cooling system to carry away the excess heat produced during operation.

Electrolysis cells are classified according to the electrolyte, electrodes and the temperature and pressure of operation. The electrolyte must exhibit high ionic conductivity and must not chemically decompose under the cell voltage, so that only water is decomposed. It should not be volatile and should have a strong resistance to pH changes. Strong acids like sulphuric acids and strong bases like potassium hydroxide meet these criteria. Acid electrolytes present severe corrosion problems and are not usually selected. The most common electrolyte used in industry is a

potassium hydroxide solution. Industrial cells using a KOH solution usually operate at a current density of 0.2 to 0.4 A/cm^2. The concentration of the KOH solution is usually about 30 wt.%, since the conductivity of KOH is a maximum at this concentration. The potential drop due to the resistance of the electrolyte is calculated as an IR drop in the system. (I is the current in amperes and R is the resistance of the electrolyte in ohms.)

The electrodes must be good electronic conductors and must have a good catalytic surface for the discharge of hydrogen and hydroxyl ions. A separator is required to prevent the hydrogen and oxygen gases from mixing together inside the cell. The separator must be porous, so that an ionic conducting low resistance path can be formed between the electrodes; it should not react with or be soluble in the electrolyte.

The current efficiency of most electrolysis processes is usually close to 100%. There may be a small loss of efficiency due to parallel reactions, recombination of soluble reaction products, or a slight shorting of current between the electrodes of the cell. Besides the IR drop, there are other losses which cause the operating potential to be greater than the minimum theoretical value (E_{rev}) necessary for the decomposition of water, which is given by

$$E_{rev} = - \Delta G^0 / nF = 1.23 \text{ V} \qquad (2.53)$$

where ΔG^0 is the free energy change for the following reaction at 25°C and 1 atm. pressure

$$H_2O \longrightarrow H_2 + \frac{1}{2} O_2 \qquad \begin{matrix}\Delta H^0 \\ 68.3\end{matrix} \quad \begin{matrix}\Delta G^0 \\ 56.69\end{matrix} \text{ kcal/mole.}$$

F is the Faraday constant and n is the number of electrons taking part in the reaction

The actual voltage (E) in a practical operating cell is given by

$$E = E_{rev.} + \Sigma \eta + IR \qquad (2.54)$$

where $\Sigma\eta = \eta_{cathode} + \eta_{anode} + \eta_{mt}$; η is the overvoltage. The η for the anode and cathode represents the potential difference between the operating voltage of the electrode, and the potential of a non-polarizable electrode. The (η_{mt}) is the overvoltage caused by mass transport of the gaseous products away from the electrode surface.

The voltage effiency of an electrolysis cell decreases as the current is increased. The operating voltage is plotted against the current density to give a characteristic curve, commonly called a polarization curve. This curve is the most important parameter in the design of an electrolyzer system. In this work, the polarization curve of the "half-cell", i.e. the overvoltage between the non-polarizable reference or reversible hydrogen electrode (RHE) and the cathode is determined. The details involved in obtaining this curve are described in chapter 4.

The energy effiency ε_{th} of an electrolytic cell is defined as

$$\varepsilon_{th} = \frac{\Delta H}{\Delta G^0 + \text{losses}} = \frac{\Delta H}{n F \{ E_{rev} + \Sigma \eta + IR \}} \qquad (2.55)$$

According to the definition in (2.55) a cell operating with a voltage less than 1.48 V would have a theoretical effiency of greater than 100%. which means that the cell would cool during its operation, and would absorb heat from its surroundings. However typical operating cells have an IR drop and overvoltage that cause the cell to operate at a voltage of 1.8 to 2.0 volts and an efficiency of 70 to 82%.

2.3.2 The polarization curve

At the instant of immersion of an electrode into an electrolyte, the nature of the reaction is determined by the electrochemical potential of the reacting species (M) that is transferred across the interface for the reaction

$$M^+ + e^- \longrightarrow M \qquad (2.56)$$

The electrochemical potential ($^{M}_{\Delta}S\ \eta_{M^+}$) of the specie M^+ across the metal solution interface is given by the sum of the chemical and electrical potentials as

$$^{M}_{\Delta}S\ \eta_{M^+} = {}^{M}_{\Delta}S\ \mu + F\ {}^{M}_{\Delta}S\ \phi \qquad (2.57)$$

where F is the Faraday constant, $^{M}_{\Delta}S_{\mu_{A^+}}$ is the chemical potential between the metal and solution and $^{M}_{\Delta}S_{\phi}$ is the

electrical potential between the metal and solution.

For equilibrium ${}^{M}_{\Delta}S_{\eta_{M^+}} = 0$. Under conditions of a zero field the gradient of the chemical potential acts as the driving force for the reaction. The rate of the forward reaction ($\vec{k}_c$) is given by

$$\vec{k}_c = \frac{k\,T}{h} \exp\left(\frac{-\Delta G^{0\ddagger}_c}{R\,T}\right) \qquad (2.58)$$

where k is the Boltzmann constant,

T is the absolute temperature,

h is the Planck constant,

$\Delta G^{0\ddagger}$ is the activation energy fig 2.7a,

and R is the gas constant.

The velocity of the reaction ($\vec{v}$) is given by

$$\vec{v}_c = \vec{k}_c\, C_{M^+} \qquad (2.59)$$

where C_{M^+} is the concentration of M at the plane A which is called the outer Helmholtz plane (OHP) (Bockris and Reddy 1970). At this stage the introduction of an electric field fig. 2.7b at the electrode solution interface will cause the activation barrier of the reaction 2.56 to be modified as in fig. 2.7c. The symmetry factor, β , in fig. 2.7b is defined as the ratio of the distance from the plane A to the top of the barrier to the complete distance across the barrier:

$$\beta = \frac{x_2}{x_1 + x_2} \qquad (2.60)$$

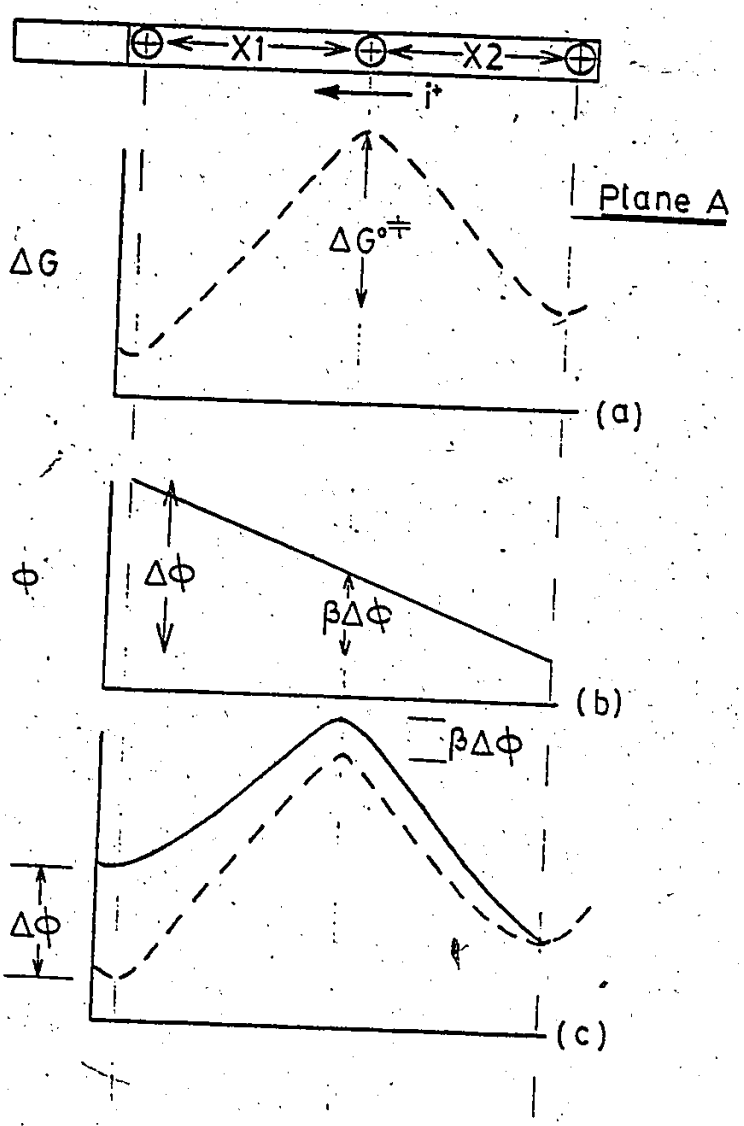

Figure 2.7 (a) Chemical activation barrier for the reaction in equation (2.56).

(b) Electric field extends out from the electrode surface to the outer Helmholtz plane A.

(c) Modified electrochemical barrier.

where the distances X_1 and X_2, are defined in fig. 2.7a.

The activation barrier under the influence of the electric field is given by the the sum of the chemical and electrical parts

$$\Delta G^{0\ddagger} = \Delta G_c^{0\ddagger} + \beta F \Delta\phi \quad . \qquad (2.61)$$

From equation (2.58) and using the activation barrier of (2.61), we get the velocity of the reaction due to electrical and chemical ($\vec{v}_e$) parts as

$$\vec{v}_e = \vec{k}_c C_{M^+} \exp\left(\frac{-\beta F \Delta\phi}{R T} \right) \quad . \qquad (2.62)$$

The current for the reaction is given by:

$$\vec{i} = \vec{v}_e F \qquad (2.63)$$

where λ is the number of electrons transferred for one rate determining step to occur, and N is Avagadro's number.

In a similar way to (2.62), the velocity of the de-electronation reaction is given by

$$\vec{v}_e = \vec{k}_c C_M \exp\left(\frac{(1-\beta) F \Delta\phi}{R T} \right) \qquad (2.64)$$

The net current is given by the sum of (2.62) and (2.64) combined with (2.63)

$$i = \vec{i} - \vec{i} = F \vec{k}_c C_M \exp\left(\frac{(1-\beta) F \Delta\phi}{R T} \right)$$

$$- F \vec{k}_c C_{M^+} \exp\left(\frac{-\beta F \Delta\phi}{R T} \right) \qquad (2.65)$$

The $\Delta\Phi$ can be split up into the equilibrium potential ($\Delta\Phi_e$) and the overvoltage η

$$\Delta\Phi = \Delta\Phi_e + (\Delta\Phi - \Delta\Phi_e) = \Delta\Phi_e + \eta \; . \qquad (2.66)$$

Substituting (2.66) into (2.65)

$$i = \{ F \vec{k}_c C_M \exp \left(\frac{-(1-\beta) F \Delta\Phi e}{R T} \right) \} \exp \left(\frac{(1-\beta) F \eta}{R T} \right)$$

$$- \{ F \overleftarrow{k}_c C_M + \exp \left(\frac{- \beta F \Delta\Phi e}{R T} \right) \} \exp \left(\frac{- \beta F \eta}{R T} \right)$$

$$\ldots . \qquad (2.67)$$

The terms in the brackets { } have the same magnitude and are equal to the exchange current density i_0. Equation (2.67) is called the Butler-Volmer equation.

In the high field limit where $\eta >> 0.1$ volts, $\vec{i} > \overleftarrow{i}$ and hence

$$i = i_0 \exp \left\{ \frac{(1 - \beta) F \eta}{R T} \right\} \qquad (2.68)$$

This equation is usually written in the logarithmic form and the transfer coefficient, (α), is substituted for $(1- \beta) \lambda$ to give the Tafel equation.

$$\eta = \frac{- 2.303}{\alpha F} RT \log i_0 + \frac{2.303}{\alpha F} RT \log i \qquad (2.69)$$

where η is the voltage between the working electrode and a non-polarized interface.

2.3.3 The mechanism of the hydrogen liberation reaction in alkaline solutions.

Determination of the mechanism of an electrochemical reaction involves the detailing of the various stages of the reaction path (rp) together with the rate determining step (rds). The overall reaction is easily determined by an analytical assay of the reactants and products. The overvoltage in the Tafel plot is substantially caused by the activation process of the rds, and hence a study of the polarization curve can yield information on the reaction mechanism. The rp and rds can be deduced from a determination of the kinetic parameters (Srinivasan et al. 1967) such as: the Tafel slope, exchange current density (i_0), transfer coefficient (α), stoichiometric number (μ), and the order of the reaction (n_i). The stoichiometric number, defined by Bockris and Potter (1952), is the number of times the rds must take place for one act of the overall reaction. In addition to the above parameters, separation factors (S_D and S_T, for deuterium and tritium respectively) which result from a small change in the activation barrier due to isotope effects are useful in determining reaction mechanisms. A study of the adsorbed species, which may be reactants, intermediates or products is useful in determining the rp.

The various stages in the cathodic reduction of water are listed below

1) the transport of the hydrogen-containing water

(H_2O) or hydronium (H_3O^+) molecule to the electrode surface.

2) the transfer of ions or possibly protons to the electrode surface and their discharge by electrons.

3) the combination of hydrogen atoms on the electrode surface to form a molecule of hydrogen.

4) the evolution of hydrogen molecules as gas bubbles.

Experiments done by Eyring et al. (1939) on a variety of electrode surfaces show that the overpotential is dependent on the type of electrode used and hence stage 1) is not the rds. Although stage 4) probably plays some part in increasing the overvoltage at the usual operating current densities (0.2 to 0.4 A/cm^2), its importance is accentuated at higher current densities, where the coverage of the active surface of the electrode by hydrogen bubbles is greater.

The i_0 in equation (2.67) can be split into the entropic and enthalpic parts to give

$$i_0 = B \exp\left(\frac{\Delta H}{R\,T}\right) \qquad (2.70a)$$

$$B = \frac{\lambda\, F}{N}\,\frac{k\, T}{h}\,\exp\left(\frac{\Delta S^{0\ddagger}}{R}\right) \qquad (2.70b)$$

Substituting $C = 10^{15}$ molecules/cm^2, the value of B (Eyring entropy factor) is

$$B = 9.6 \times 10^{8} \exp\left(\frac{\Delta S^{0\ddagger}}{R}\right) . \qquad (2.70c)$$

Using equation (2.70a), Eyring et al. have shown that the value of B is a constant in solutions of varying pH and on several electrode materials. This suggests that the species representing the concentration C in (2.70b) is the same in all aqueous solutions and all electrodes. Hence it is inferred that the discharge of hydrogen ions probably involves a water molecule.

A possible mechanism for the rp has been postulated by Eyring et al.; fig. 2.8, elucidates the mechanism. It is assumed that the electrode is substantially coated with a unimolecular layer of water molecules, which are in equilibrium with the metal. Adjacent to this layer is a somewhat diffuse layer of water molecules, attached to and in equilibrium with the solution. The potential V acts across both the layers. By calculating the entropy of activation of the activated state, which is the transfer of a proton from a water molecule in solution to the adsorbed OH, the value of B can be calculated. This is compared to the experimental value obtained. Eyring et al. assume that the entropy of activation for the above process will be close to the value for the reaction

$$H_2O + H_2O \longrightarrow H_3O^{+} + OH^{-} \qquad (2.71)$$

The value of $\exp(\Delta S^{0\ddagger}/R)$ is calculated to be 3.3×10^{-8}.

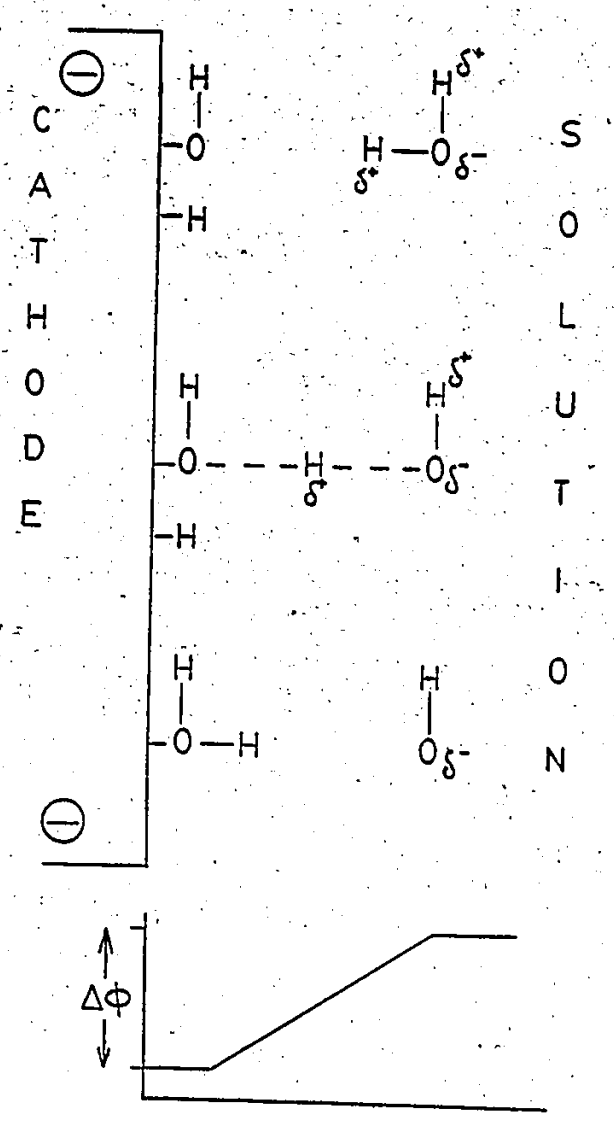

Figure 2.8 Illustration of hydrogen liberation reaction (Eyring et al. 1939). The overvoltage acts over two layers of molecules, and the activacted state lies midway between them. The adsorbed molecule is at the same potential as the electrode surface.

Substituting this in (2.70c), a value of B = 1.5 is obtained. This value is close to the value of about 2.0 obtained in experiment, and hence Eyring et al. assume that the rds is the transfer of a proton from a molecule of water in solution to a molecule of water adsorbed to the electrode surface.

The overall reaction at the cathode is given by

$$2\ H_2O + 2\ e^- \longrightarrow H_2 + 2\ OH^- \quad (2.72)$$

Bockris and Potter (1952) show that in dilute alkaline solutions on nickel electrodes the stoichiometric number $\mu \approx 2$. This suggests that the discharge reaction given by

$$H_2O + e^- \longrightarrow H_{ads} + OH^- \text{ (Volmer)} \quad (2.72a)$$

is the rate controlling step. In order to determine the stoichiometric number, the Tafel parameters have to be determined at low overpotentials, where parallel reactions like oxidation and dissolution occur. Hence the stoichiometric numbers are not available on many metallic surfaces. The rp is that in (2.72a) followed by either the electrochemical desorption reaction or the recombination desorption reaction on the electrode surface.

$$H_{ads} + H_2O + e^- \longrightarrow H_2 + OH^- \text{ (Heyrovsky)} \quad (2.72b)$$

$$2\ H_{ads} \longrightarrow H_2 \text{ (Tafel)} \quad (2.72c)$$

Equation (2.72a) and (2.72b) have the same Tafel slope and can not easily be distinguished. However, they have widely differing isotope separation factors. The isotope separation factors are defined as

$$S = \frac{\left(\frac{C_H}{C_{T,D}}\right)_{gas}}{\left(\frac{C_H}{C_{T,D}}\right)_{soln.}} \qquad (2.73)$$

where the C stands for the concentration and the subscripts H,T and D stand for hydrogen, tritium and deuterium, respectively. The separation factors for the various rate determining reactions are listed below, Bockris and Srinivasan (1964a,b,c,d)

	S_D	S_T
Slow discharge, fast recombination	3.0	4.6
Slow discharge, electrochemical desorption	3.7	6.2
Fast discharge, slow recombination on Ni	5.8	13.0
Fast discharge, slow recombination on Pt	5.5	11.1
Fast discharge, slow electrochemical desorp.	9.1	23.0

Using separation factors Bockris and Srinivasan (1964) have also shown that in alkaline solutions the hydrogen liberation reaction for platinum follows a fast discharge slow electrochemical desorption mechanism.

CHAPTER 3

LITERATURE REVIEW

3.1 The Formation of Phases in Implantation and Ion Beam Mixing

3.1.1 Stable and metastable phases

The equilibrium phase diagram predicts whether a system will be a single phase or multi-phase alloy. For non-equilibrium systems, TTT curves are usually used to predict the fraction of the phases formed after a particular thermal history; these curves are constructed empirically. Classical nucleation and growth theory is useful in regions near the end of the miscibility gap; however, at higher supersaturations spinodal decomposition is applicable.

Radiation enhanced diffusion can increase diffusion as the point defect concentration increases, and can cause a reaction to go to completion. Radiation damage can cause precipitates to dissolve as atoms are struck out of the precipitate by a collision cascade (Liou 1979).

Under irradiation the understanding of phase stabi-

lity is not well advanced. The system is far from equilibrium due to the energy gained from particles slowing down. In the steady state no general minimization principle is available to predict the nature of the system. The effect of point defect concentrations on phase stability can be explained in terms of static and dynamic effects. Static effects result from the modification of the thermodynamic potential due to point defect supersaturation. In most situations the concentration of point defects, in the steady state, is not large enough to produce the 10 to 100 kJ/mole required to destabilize an existing phase. Dynamic effects are caused by the segregation of a species under point defect fluxes. In systems that have large differences in the sizes of atoms, the steric effect and the higher heats of formation for interstitials of the larger specie are responsible for segregation of species under interstitial fluxes. The energy of formation of interstitials is substantially due to ion-core interactions. For vacancy fluxes the binding energies associated with the vacancies and atom specie in the material cause segregation. The segregation of atomic species can cause the local concentration to exceed the solubility limit and a new phase can nucleate.

Transformations caused by static effects are important in systems where order-disorder reactions occur. If a system has a high ordering energy and a low ordering rate, the energy required for radiation-induced disorder can reach

the levels required to modify phase stability. Antistructural defects produced by replacement collision sequences and i-v recombination can produce the energy changes required to modify the position of the solvus e.g. from A to A' in Fig. 3.1 (Liou 1979 and Martin 1982).

In IM experiments with a limited composition configuration (Averback 1986), Mayer et al. (1981) have shown that the solid solubility limit can be extended across the entire composition range. The lattice parameters are found to deviate slightly from Vegard's law. In systems with a miscibility gap and different crystal structures, an amorphous phase forms over a limited composition range. The extended solubility is believed to be a result of extremely fast dissipation of energy in the collision cascade (10^{14} K/s). The atoms are assumed to be quenched from a highly energetic state into a non-equillibrium structure. This approach is similar to that used to explain the formation of amorphous phases in the conventional splat-cooling technique.

3.1.2 The formation of amorphous phases.

Amorphous metallic phases are usually produced by splat cooling metal-metalloid systems with deep eutectics. Such systems have positive heats of mixing, causing phase separation in the solid state. In the molten state above the eutectic, it is assumed that there is some association between like atoms. These associations are precursors of the

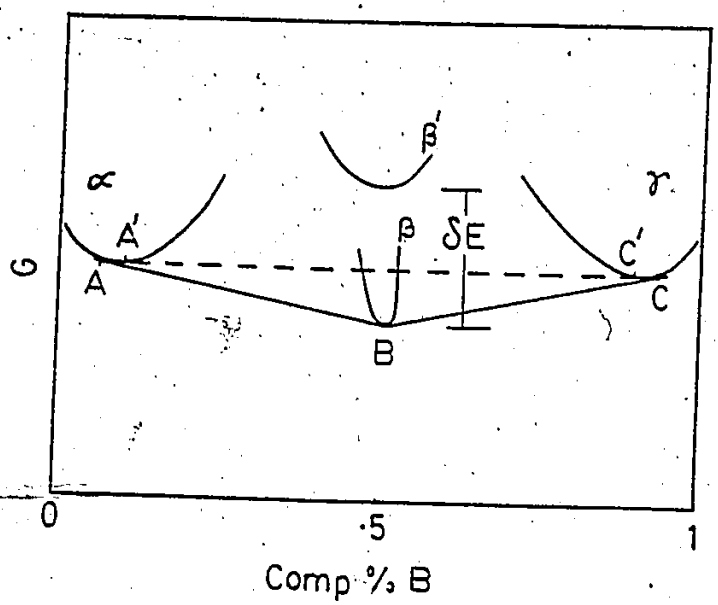

Figure 3.1 Shows how an ordered intermetallic compound β increases its free energy by δE as it disorders under irradiation. A new equilibrum is then indicated by the dashed line A'C' between the α and β phase. The solubility changes from A to A' and from C to C'.

phase separation. Between these associated regions there exist regions containing a random distribution of atom species. When the system is quenched rapidly, the resulting solid retains the structure of the melt, and an amorphous phase is formed.

In IM a similar approach is used to explain the formation of amorphous phases in systems with positive heats of formation. Experiments conducted by Mayer et al. (1981) and Tsaur et al. (1981) show that amorphous phases form in eutectic systems at low temperatures, where diffusion related phenomena are "frozen" out. This is believed to be the case in the temperature-independent region of the Q-curve (Lau et al. 1983). Elemental solids which have different crystal structures must have a two-phase region. The terminal solubilities are extended from both sides and eventually become structurally incompatible, resulting in the formation of an amorphous phase. This can be explained using a free energy diagram such as Fig. 3.2. In regions α and β crystalline phases are formed. However in the central region at [2] the amorphous state has a lower energy than the irradiated material at [1], and hence this phase forms. There are a large number of point defects which, if mobile, could allow for the nucleation and growth of crystalline phases. For the system to move to the equilibrium state at point [3] atomic motion must occur.

Systems which have a large negative energy of mixing

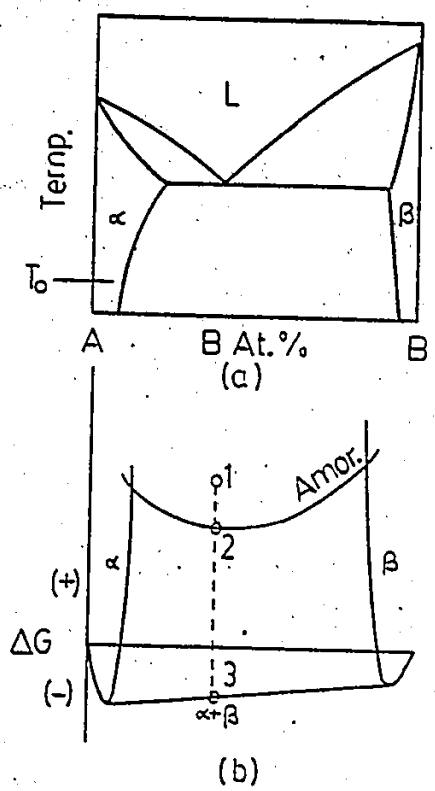

Figure 3.2 Ion beam induced amorphization of eutictic systems.

usually form compound phases. Brimhall (1983) has studied the effect of irradiation on compound phases. His studies suggest that amorphous phases are formed in compounds which have a limited compositional range. Fig. 3.3 shows the phase diagram for the Ni-Al system along with a hypothetical free energy diagram. For line compounds the free energy curve is extremely steep so that a small change in composition will result in a higher free energy than the amorphous state, and hence the crystalline to amorphous transition. Swanson (1971) suggests that a critical defect density C_D must accrue before the transition occurs. This is expressed as

$$E_c + C_D E_D > E_a \qquad (3.1)$$

where E_c is the free energy of the crystal,

E_D is the free energy of a radiation produced defect,

and E_a is the free energy of the amorphous phase.

If radiation can produce this critical defect concentration so that the inequality (3.1) is satisfied, then the structure should relax to the amorphous state. For line compounds the C_D is not expected to be large. At lower temperatures the retention of defects is expected to be greater. Hence low temperatures and a narrow phase extent are expected to favour the crystalline to amorphization transition.

3.1.3 Ion beam mixing of the Pt-Fe system

IM has been carried out in in the Pt-Fe system for

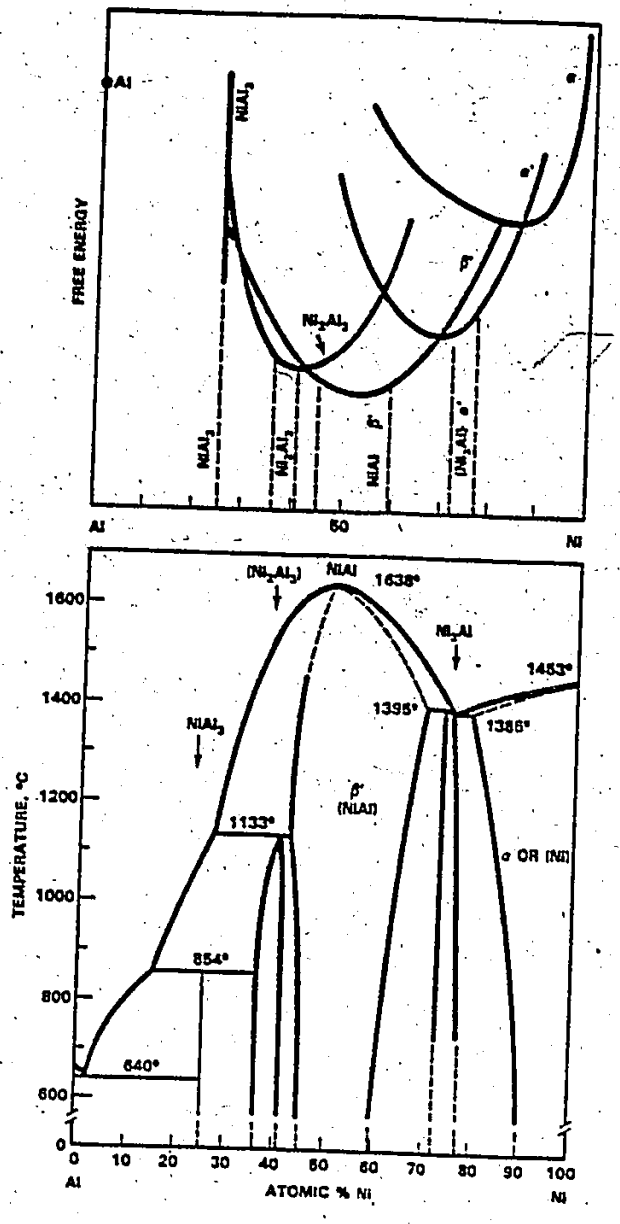

Figure 3.3 Ni-Al phase diagram with hypothetical free energy diagram. The line compound $NiAl_3$ has a steep free energy curve.

thin films (Bottiger et al. 1983) and in bi-layer systems (Battaglin et al. 1984). Thin film markers of ~1 nm. platinum were evaporated on to ~200 nm. of iron followed by evaporation of ~40 nm. of iron on top of the platinum. The mixing was carried out using 150 KeV Ar^+ ions in the temperature range between 18 and 345 K. A large step in the mixing rate was observed above 25 K. It was found that samples contaminated with oxygen gave rates of mixing that were reduced by about 30%. A non-linear dependence of the mixing rate with fluence suggests that ballistic mixing theories are not applicable above 25 K and a diffusive process may be operating.

Platinum-iron bilayers were prepared by evaporating ~80 nm. of Fe and ~20 nm. of Pt on to a Si substrate. Mixing was caried out with 120 KeV Kr^+ at room temperature; the rate of mixing varied linearly with $(dose)^{1/2}$. The occurence of a step in the Fe peak suggests the formation of a phase with definite stoichiometry. The phase was calculated to have a composition of $Pt_{60}Fe_{40}$. X-ray diffraction measurements suggested the formation of a phase with fcc structure, and of the above composition.

3.2.1 Electrocatalysis of the hydrogen liberation reaction.

Electron transfer to an adsorbed species is a radiationless process. During electron transfer the electron

crosses the gap between the electrode and solution levels by a tunnel type mechanism, such that the energy level of the electron in the metal is equal to the energy level of the discharged species.

The concentration of the adsorbed species on the electrode surface depends on the free energy change between the species in the adsorbed state and the unadsorbed state. The free energy of adsorption contains entropic and enthalpic parts. The entropic part represents the loss of translational degrees of freedom between the solution and adsorbed states, and remains almost a constant for different metal systems. The enthalpic term (ΔH^0_{ads}) depends on the nature of the substrate. Conway and Bockris (1957) have shown that there is a statistical correlation between the logarithm of the exchange current density ($\log i_o$) and the work function (ϕ) for one group of metals (line A in fig. 3.4) while another relationship given by line B exists for another group of metals. Although the metals in group B have similar values of ϕ to those in group A, metals in group B are known to have lower values of ΔH^0_{ads} than those in group A.

$\log i_o$ increases linearly with the "percent d-character" (%-d) of the metals for the group A metals. A metal having all of its d-shell electrons filled will have more %-d than a metal with some of its d-shells empty. A metal with some of its d-shells empty will tend to have high

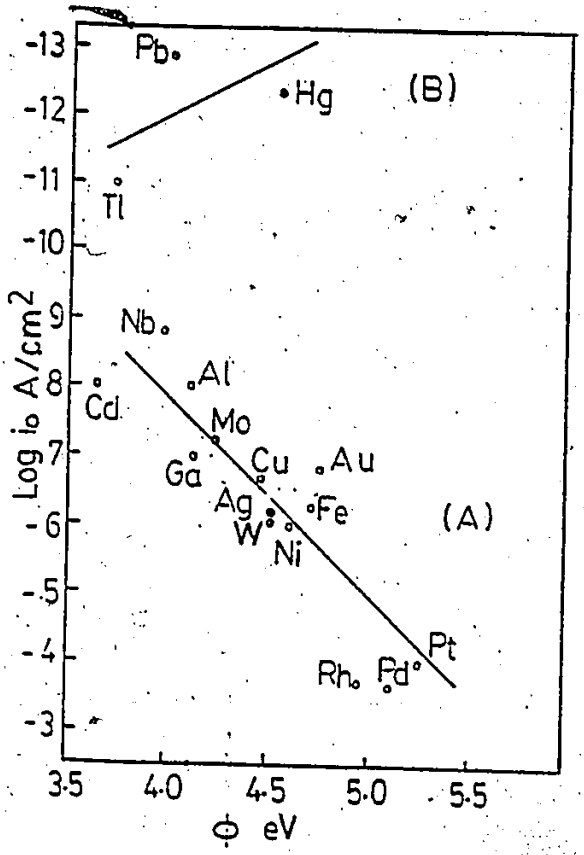

Figure 3.4. Linear dependence between the logarithm of the exchange current density (log i_0 A/cm^2) and the work function ϕ eV, for two groups of metals A and B.

ΔH^0_{ads}, as it can bond strongly with molecules that donate electrons. Metals with high %-d will also tend to have high ϕ, as electrons that have their spins paired are more stable in the metal lattice. Since the ΔH^0_{ads} and the ϕ are related it is expected that a correlation exists between the ΔH^0_{ads} and log i_o. Fig. 3.5 shows this correlation between ΔH^0_{ads} and log i_o.

Eyring (1939) has explained how the value of ΔH^0_{ads} changes i_o, using the concept of the stretching of the proton-water molecular bond to form an activated complex. The heat of activation $\Delta H^{\ddagger}_o$ is used in equation (2.70a). This process is depicted in fig. 3.6. If a metal adsorbs water by forming strong M-H bonds, the oxygen atom of a water molecule attached to the surface will have an increased affinity for the formation of a bond with hydrogen. This has the effect of making curve A in fig. 3.6 less steep and reducing $\Delta H^{\ddagger}_o$. Also metals which adsorb hydrogen atoms strongly will tend to make curve B less steep so that $\Delta H^{\ddagger}_o$ is further diminished. For large ΔH^0_{ads} the value of $\Delta H^{\ddagger}_o$ may be sufficiently reduced, that the rate controlling step may be shifted to the desorption reactions, equations 2.72b or c. The activated state now involves the partial desorption of the adsorbed hydrogen. Indeed this is found to be the case for the group A metals. Tantalum which adsorbs hydrogen more strongly than platinum has a lower exchange current density.

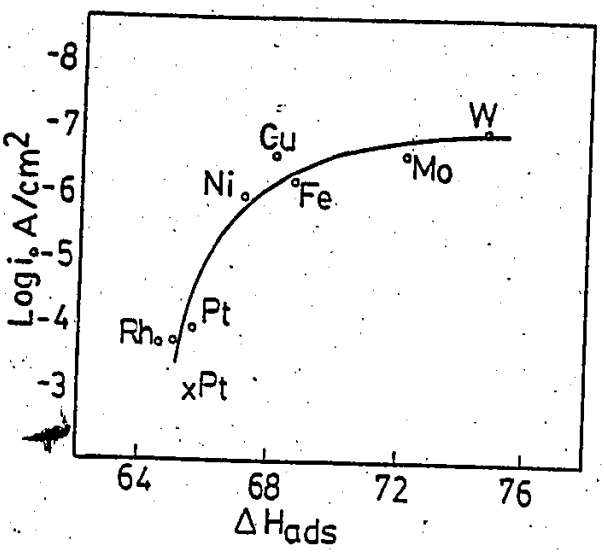

Figure 3.5 Diagram showing the relationship between log i_0 A/cm^2 and ΔH^0_{ads} in kcal/mole for hydrogen on these metals.

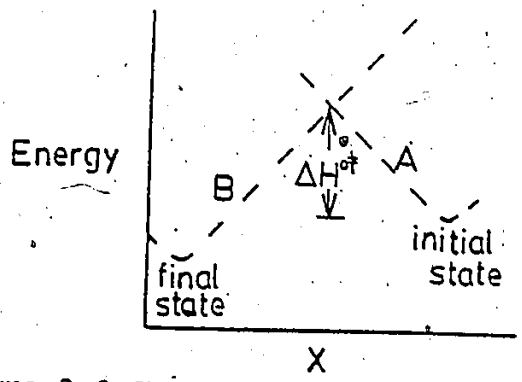

Figure 3.6 Chemical potential barrier versus the H to OH distance X.

initial state: HO --- H + H_2O --- Metal

H_2O ---- } Metal

final state : OH^- + H ---- }

The optimum value of ΔH^0_{ads} can be obtained by constructing volcano plots, where the log i_o is plotted against ΔH^0_{ads} or ΔG^0_{ads}. These are constructed for each reaction path (rp), assuming that each step (2.72a,b and c) is rate determining while the remaining steps remain in equilibrium. The reaction path will be the one whose rds indicates the greatest rate under the same conditions. Parsons (1958) has constructed such plots and concludes that the metals such as those in group B which adsorb hydrogen weakly (ΔG^0_{ads} positive) have low values of i_o ($\sim 10^{-12}$ A/cm^2). Metals which adsorb hydrogen moderately, such as platinum, have high values of i_o ($\sim 10^{-3}$ A/cm^2), and metals that adsorb hydrogen strongly e.g. tungsten and molybdenum have somewhat smaller values ($\sim 10^{-6}$ A/cm^2). The work of Parsons suggests that platinum has an optimum value of ΔH^0_{ads} and is therefore the most effective catalyst for the hydrogen liberation reaction.

3.2.2 Implantation and ion beam mixing in electrocatalysis

Ion implantation and ion beam mixing are used to modify the surface and near surface regions of a solid. If the modified material finds usage at low temperatures where thermal diffusion lengths are negligible, the surface can retain its structure and chemical composition. Equilibrium, metastable and amorphous phases can be formed. Amorphous phases should offer extremely high levels of corrosion resi-

stance due to the lack of grain boundaries or grains of different orientation, and the resulting high uniformity (Grant 1981 and Clayton 1981). The ability of ion beams to readily change the surface of materials, using extremely small quantities of noble metals, is potentially extremely useful in the production of electrocatalysts, where the surface chemistry and structure are of major importance.

There have been a few studies on the use of ion beams to modify electrodes with electrocatalysts. The first of these was by Voinov et al. (1974). They implanted Pt^+ into pyrocarbons and studied the oxidation of hydrogen and the reduction of oxygen in 1M $HClO_3$ solutions. A good correlation was found between the H_2 oxidation and the amount of platinum implanted while for oxygen reduction, no correlation was observed. Grenness et al. (1974) studied the effect of platinum implanted into tungsten electrodes and tungsten oxide (WO_3) coated electrodes in 1M H_2SO_4 solution. The results show that there is an electrocatalytic improvement in the implanted WO_3 coated electrodes after several cathodic sweeps while the implanted tungsten samples showed an improvement only after anodic polarization. It is believed that the activation processes for the tungsten and the tungsten oxide cause the platinum to come to the surface of the solid-solution interface. Hayes et al. (1976) studied the effect of platinum implants into cadmium, copper and gold; the implants did not produce any significant catalytic

change for the hydrogen liberation reaction. Kuhn and Wright (1972) implanted platinum into titanium and found an increase of catalytic activity for the chlorine-liberation reaction in a solution of 2 M sodium chloride with 10^{-2} M hydrochloric acid.

Kasten and Wolf (1980) implanted platinum into iron and found that the catalytic activity for the hydrogen-liberation reaction from sulphuric acid improved considerably; for an implantation of $5x10^{16}$ /cm^2, the catalytic activity is greater than that of smooth platinum. Platinum sputtered onto the iron substrate shows a catalytic activity between that of pure iron and pure platinum, with the catalytic activity increasing as the amount of sputtered platinum is increased. Wolf (1980) reported a small catalytic improvement in the samples subjected to neon damage by an ion dose of $5x10^{17}$ /cm^2 at 240 KeV. The reduction in overpotential was small compared to other implants, indicating that the major cause of reduction in overpotential is a chemical effect. Implants of lead, which is known to be inactive in acids, showed a reduction in catalytic avtivity, whereas gold implants improved the catalytic activity of iron. Akano et al. (1981) showed that a reduction of 20 to 40% of the overpotential for the oxygen-evolution reaction could be obtained by the implantation of silver into nickel electrodes. The experiments were carried out in 30 wt% KOH solution at 80^{o}C. A shift of the implanted silver profile in these

electrodes after anodic polarization indicated growth of a nickel oxide corrosion layer. Subsequent polarization also caused a loss in the total amount of implanted silver by its anodic dissolution. Thompson et al. (1982) implanted Ru^+, Rh^+, Pd^+, Ag^+, Ir^+ and Pt^+ ions into nickel. The same elements were also evaporated onto nickel substrates and ion beam mixing was caried out using 80 KeV Ar^+ ions. The ion beam modified surfaces were tested as anodes in a manner similar to Akano et al. The results showed a small improvement in the ruthenium and platimum samples and a significant improvement for the silver implanted samples; however, only ruthenium and rhodium showed a small improvement for the ion beam mixed samples. The beneficial effect was not long lasting and subsequent RBS analyses showed the formation of a surface oxide layer which was depleted in the alloying element. In addition, some of the alloying element was anodically dissolved into the electrolyte. The loss of the alloying element coupled with its burial beneath the oxide layer was consistent for the elements investigated, except for iridium where loss of this element occured; but its presence at the surface led to no observable oxide corrosion layer.

3.3 The Pt_Fe System

3.3.1 The equilibrum phase diagram

The phase diagram for the platinum iron system is

shown in fig. 3.7. Equilibrium measurements were done down to 600 °C. Speculative equilibria are added on below 600 °C in broken lines.

At high temperatures (above 911 °C) iron and platinum form a continuous f.c.c. solid solution. Three superlattices Fe_3Pt, FePt, and $FePt_3$ form at ~835, ~1300 and ~1350 °C. The Fe_3Pt has an ordered cubic Ll_2 type structure, and the FePt has an ordered tetragonal Ll_0 type structure with a = 3.838 Å and c = 3.715 Å and c/a = 0.968. The $FePt_3$ has an ordered Ll_2 type structure.

3.3.2 The mobility of point defects in platinum and iron

In a solid irradiated at low temperatures (~4 K), the radiation damage produces stable Frenkel pairs. Upon heating the sample, thermal vibrations lead to the mobility of defects and to reactions between them. Isochronal anneals and plots showing the fractional change of recovery as a function of temperature are useful to characterize the various stages of the anneal. These stages are associated with a particular reaction.

In iron, stage I annealing is divided into six principal substages between 33 and 150 K (Neely and Keefer 1967). The last substage in stage I, which is denoted by I_E, is believed to be that of long range migration of interstitials; the four earlier substages are attributed to recombination of close i-v pairs. The activation energy for

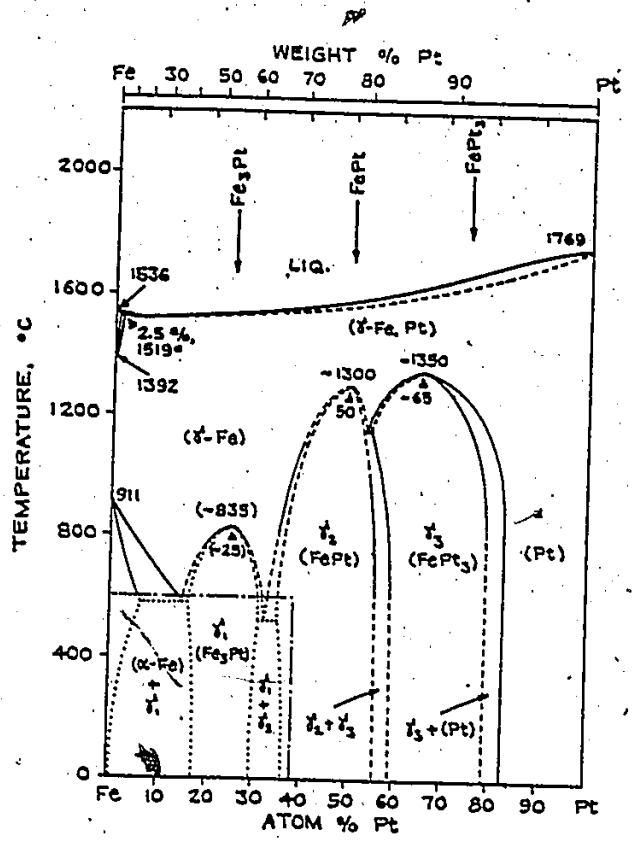

Figure 3.7 Equilibrum phase diagramm for the platinum iron system.

from: The Handbook of Binary Phase Diagrams. Vol. 3

Author: Moffatt W G, General Electric Company

the migration of interstitials is found to be 0.3 eV. Using doping experiments, Takamura (1979) has shown that the vacancies in iron are mobile at about 390 to 430 K; the activation energy for the mobility of vacancies is found to be 1.28 eV.

Frank et al. (1976) and (1979) and Seeger and Frank (1976) have studied the mobility of defects in platinum. They believe that interstitials in platinum have two configurations; one is mobile at stage I temperatures between 20 to 30 K by the crowdion mechanism and has an enthalpy of migration of 0.065 eV . Below 140 K the stage I interstitials are metastable and are converted to the stage III configuration at 140 K. In stage III at 300 to 400 K, the interstitials migrate with an energy of 0.6 to 0.7 eV. Free monovacancy migration takes place between 420 and 650 K and the activation energy for the migration of the vacancies is found to vary from 1.4 eV at 420 K to 1.2 eV at 550 K; it increases to 1.4 eV again at 650 K. A decrease in activation energy at 550 K is attributed to recovery by both monovacancies and divacancies. Recovery proceeds by the movement of monovacancies at 650 K because most of the point defects created by irradiation have been annealed, and the concentration of vacancies at this temperature is so low that divacancies are rarely formed.

CHAPTER 4

PROCEDURES AND TECHNIQUES

4.1 Sample Preparation

4.1.1 The production and characterization of platinum-iron bilayers and electrodes.

The platinum iron bilayers were produced in an evaporation chamber (fig. 4.1) with a base pressure of 2×10^{-7} torr. The evaporation chamber is equipped with an electron gun which has three hearths, so that three consecutive evaporations can be done without breaking the vacuum. The substrates were device-grade silicon which had been oxidized for at least 2 hours at 1383 K in the presence of steam.

The reduction unit, fig. 4.2, and the evaporation chamber were evacuated. The reduction unit was then isolated using the isolation valve. Hydrogen (Canadian Liquid Air UHP) was then passed through the chamber. The heater was turned on and the temperature of the chamber was controlled at 803 K. The hydrogen supply was then turned off and the reduction chamber evacuated via the roughing valve to about 10^{-2} torr. The roughing valve was closed and the isolation

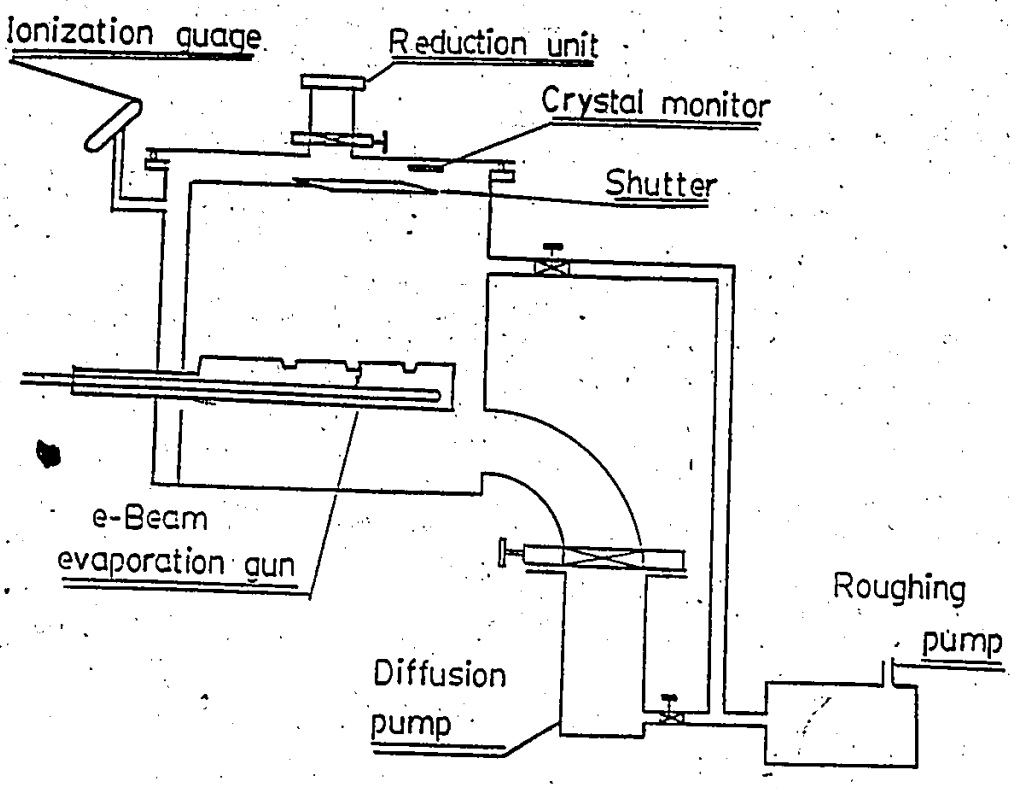

Figure 4.1 Schamatic of the evaporation chamber showing position of the reduction unit.

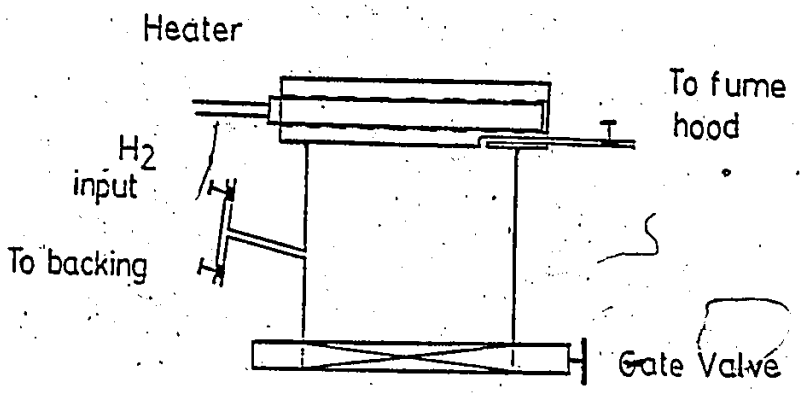

Figure 4.2 Reduction unit showing heater and gas flow lines.

valve was opened. Iron was evaporated using an electron beam evaporator at a rate of about 5 Å/sec. When a steady rate of evaporation was achieved, the shutter was removed and about 750 Å of iron was deposited onto the SiO_2 substrate. The shutter was then replaced, the isolation valve was closed and hydrogen was passed through the reduction chamber for 6 hours at 803 K. This was done in order to allow for some growth of the iron grains. The hydrogen flow was then stopped and the reduction chamber was cooled to room temperature; it was then partially evacuated by the backing line. Platinum evaporation was then started, the shutter was removed and the isolation valve was opened, so that the platinum condensed onto an oxide free surface of iron. The thickness of the platinum film evaporated was about 270 Å.

When preparing iron electrodes, disks about 1 cm. in diameter and 0.1 cm thick were cut from a Marz grade (99.99 % purity) iron rod. These disks were polished mechanically on 1μ diamond paste. The polished samples were mounted on to a sample holder and placed in the reduction chamber. The surface of iron is known to have an oxide layer that grows rapidly to 30 Å at room temperature. The samples were reduced in a hydrogen atmosphere for 6 hrs at 803 K as described above. About 250 to 270 Å of platinum was evaporated onto the surface of the oxide-free iron disks.

The final configuration of the samples is shown in

fig. 4.3 a and b. Auger depth profiles were made on the bilayer samples and the electrodes. These composition profiles are shown in fig. 4.4. There is no increase in the concentration of oxygen at the interface. The carbon concentration was also monitored. If the samples had been stored for some time before profiling, then there was a build up of carbon on the surface of the platinum; however, if the depth profiling was done immediately after the evaporation, there was no evidence of impurities on the surface. On some samples, the ion gun was used to mill a hole through the bilayer films and a line scan was done across the crater. The line scans confirmed that there was no oxide at the iron-platinum interface.

4.1.2 Process conditions for ion beam mixing

Ion beam mixing experiments were carried out in a chamber evacuated to about 10^{-6} torr. The samples were surrounded by a copper cylinder that was cooled to liquid nitrogen temperature. A beam of Fe^{+} ions having a current density of $1.0 \mu A/cm^2$ was directed on to the target with an energy of 120 KeV. The cross-section of the beam was elliptical with a eccentricity of 1.12 and the major axis was 3.7 cm. The targets had a rectangular shape and were 0.3 by 0.6 cm. Since the system did not have an ability to integrate the current accurately, a piece of oxidized silicon was placed above and below the target to monitor the dose. These

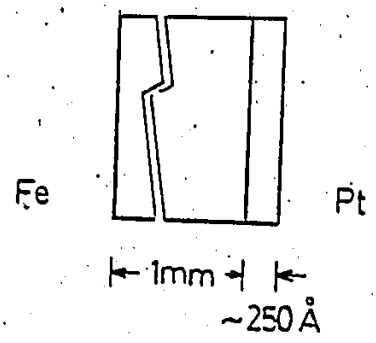

(a)

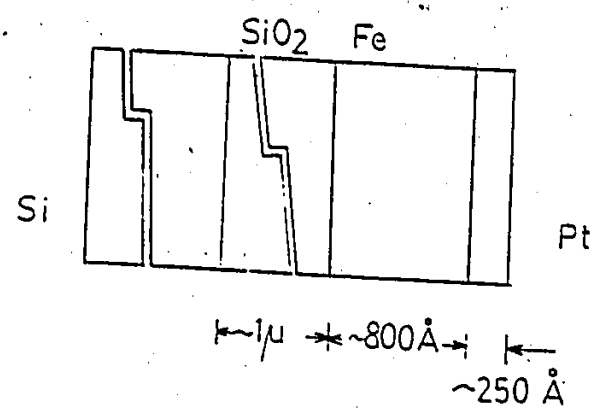

(b)

Figure 4.3 (a) Cross-section of sample used for electrode. (b) Cross-section of sample used for RBS and TEM measurements.

Figure 4.4 Auger sputtering depth profile showing composition as a function of depth. Note that there is no increase in the concentration of oxygen at the interface.

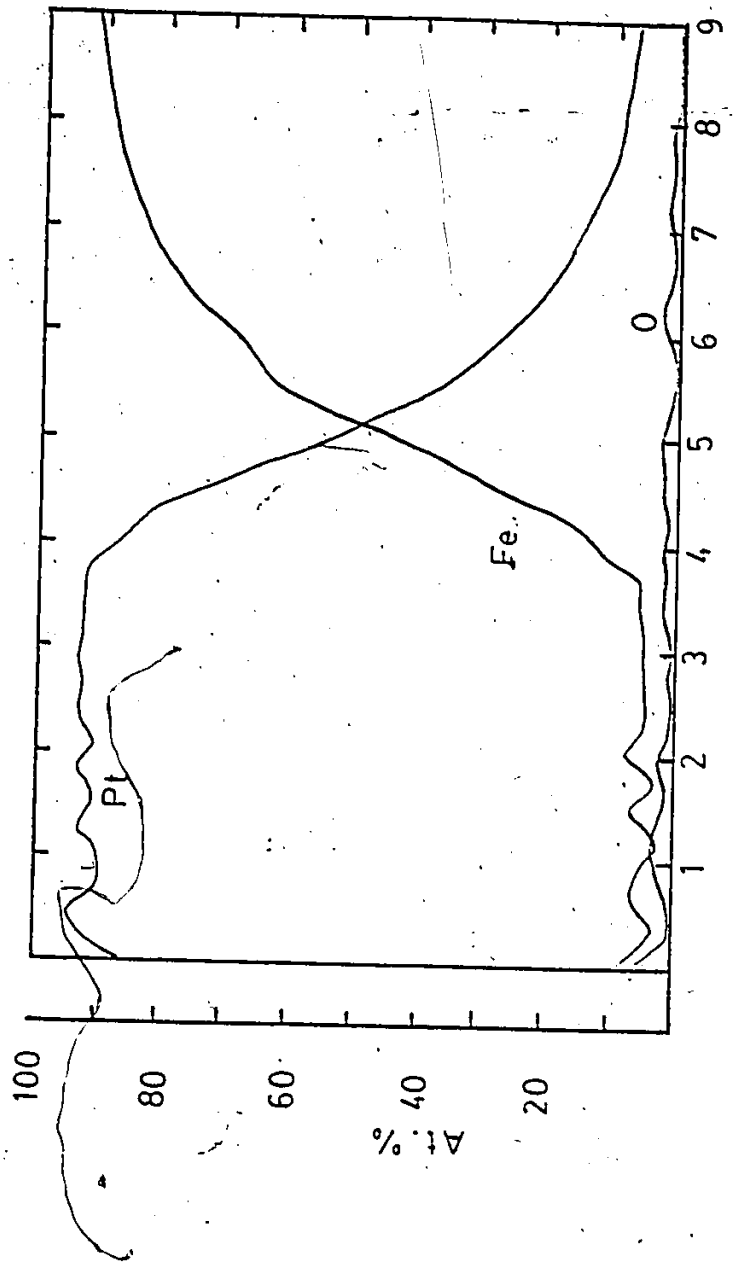
Pt
Fe
Sputter time (min.)
At. %
100
80
60
40
20
0
1
2
3
4
5
6
7
8
9

Si/SiO_2 samples acted as standards in which the implanted Fe dose could be accurately determined by RBS. The variation in the doses monitored at different locations on the silicon was found to be less than 2 percent.

The mixing experiments were carried out over a temperature range between 298 K and 523 K. An anneal carried out at 523 K for 90 minutes showed no detectable change in the RBS spectra, hence in this temperature range thermal diffusion is not important. At 573 K a considerable amount of interdiffusion in the bilayers was observed. The presence of thermal diffusion makes the diffusion process due to the ion beam difficult to study. Hence, ion beam mixing work was limited to a maximum temperature of 523 K. The dose ranged from about 4×10^{15} to 2.5×10^{16} ions/cm^2 and the longest implant took about 1 hour.

All the samples were subjected to the same heat-up and cool-down process and the temperature was maintained at a constant value during implantation. The target required about 7 minutes to heat up to 473 K and cooled to about 423 K in 10 minutes in the vacuum chamber. The temperature of the target was monitored using a chromel-alumel thermocouple.

4.2.1 Rutherford backscattering spectrometry

The implanted samples were characterized by RBS using a helium beam of about 6 nA. at about 2.0 MeV. The

typical analysis dose was 4 μC. Samples were mounted on a multi-sample holder and were analyzed at normal incidence and at sixty degrees to the beam (fig. 4.5 a,b). A gold-coated silicon surface barrier detector placed at a scattering angle of 160 degrees, fig. 4.5c, was used to measure the backscattered yield. The pressure in the analysis chamber was 10^{-6} Torr. A cylindrical copper tube, cooled with liquid nitrogen, surrounded the samples during the analysis. A ring was mounted at the face of the tube and kept at -220 V to prevent secondary electrons from escaping. A battery was used to bias the target to +300 V (cf. fig. 4.5c).

4.2.2 Sample preparation for the TEM and the STEM.

The TEM samples were prepared by etching off the silicon dioxide in a solution of 15% (volume) hydrofluoric acid. This etch also dissolved all the iron leaving only the platinum rich surface layer behind. Attempts were made to use sodium chloride single crystals as substrates in order to obtain TEM samples containing both the Pt rich and underlying Fe layers. However this was not a convenient way to study the mixing process, as the cleaved surfaces had several steps at different inclinations; films evaporated on to these surfaces were not uniformly thick and thus were not useful for RBS analysis. By using flat silicon dioxide surfaces, one could use the same samples for both TEM and

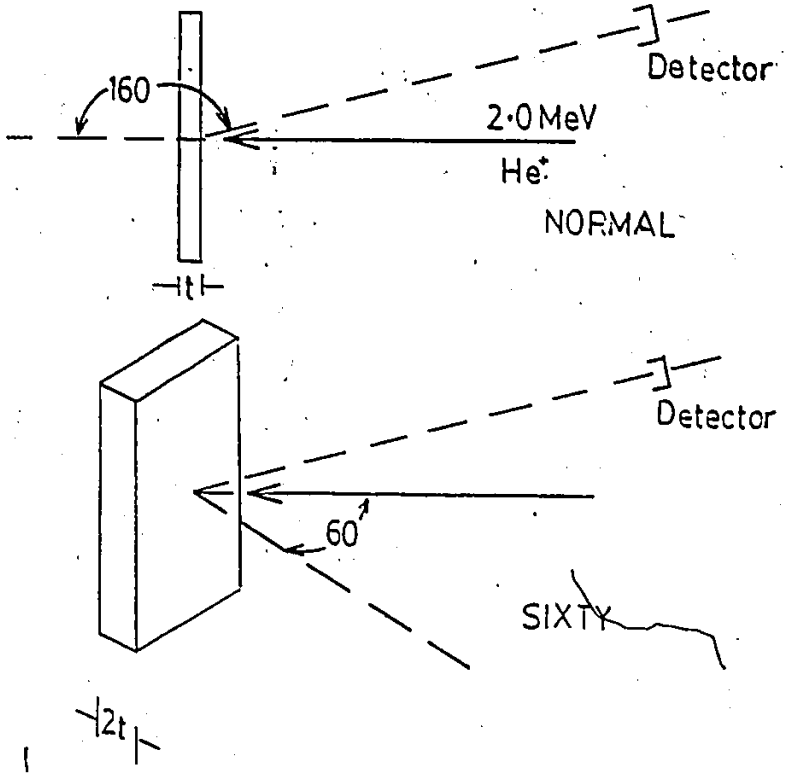

Figure 4.5 (a) Configuration for RBS measurements at normal incidence. (b) Configuration for RBS measurements at sixty degree incidence.

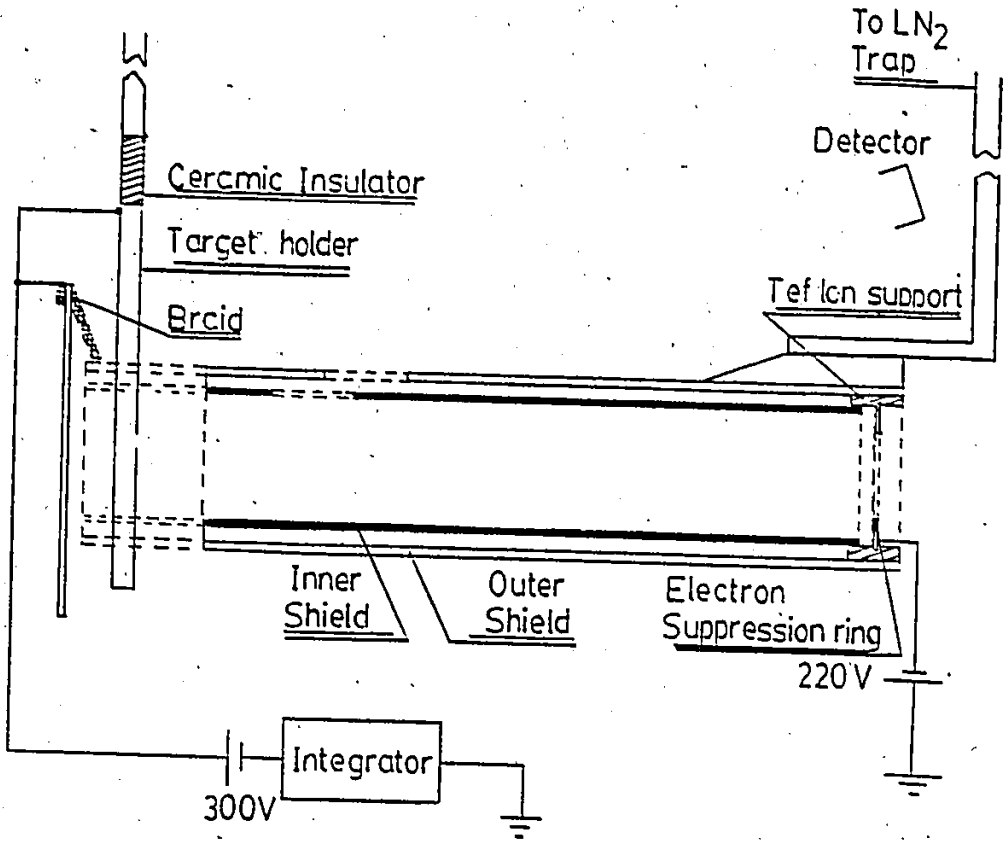

Figure 4.5 (c) Shows target surrounded by the cryo-shield along with the connections for electron suppression.

RBS analyses allowing for better consistency.

4.3.1 Preparation of the potassium hydroxide electrolytic solution

A 30 wt.% potassium hydroxide solution was produced by adding 180 g of KOH pellets to 420 ml. of deionized double distilled water. The pellets were manufactured by the J.T. Baker Chemical Company. This solution was purified using pre-electrolysis at 1 A for 15 days. The cathode was a platinum wire which darkened with time. Every 12 hours it was removed from the solution, dipped into a solution of aqua regia, and then held in the oxidizing region of a bunsen flame and washed in the deionized water before immersion into the solution again. The electrolyte was continuously stirred using a teflon-coated magnetic stirrer. There was some loss of water during the pre-electrolysis; the water was replenished every 24 hours to make up the original volume.

4.3.2 The generation of Tafel plots

The electrolysis cell, the electrode holders and the anode chamber were made of teflon. A large platinum gauze was used as the anode. The cathode holder had a knife edge against which the the electrode rested, defining an exposed area which was 0.2946 cm^2. A detailed diagram of the cell with a schematic of the electronic units used is presented

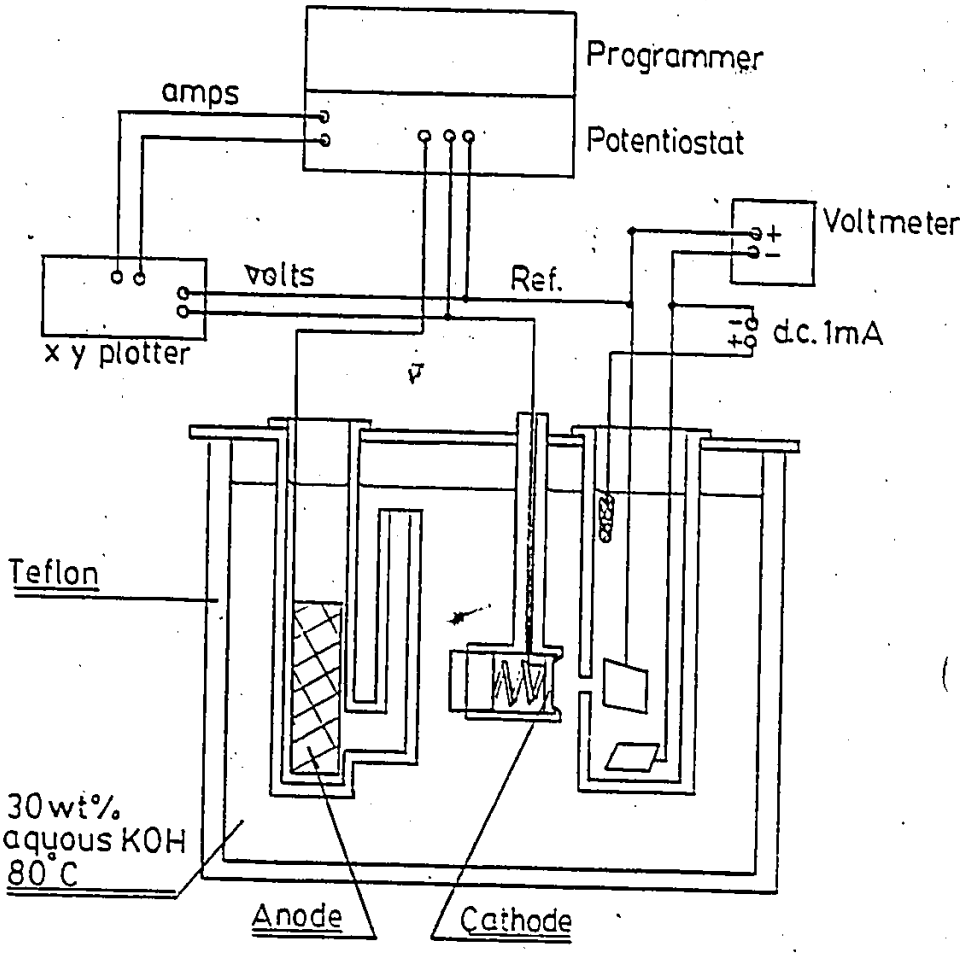

Figure 4.6 Schematic of electrolysis cell showing electrodes and the electronic equipment.

in fig. 4.6. All electrolysis experiments were carried out at 80°C.

A potentiostat manufactured by Princeton Applied Resesrch (model 173) was used for the electrolysis measurements. All measurements were conducted in the "control potential" mode. The potential was set to -1.3 V with respect to the dynamic hydrogen reference electrode. The electrode holder with the electrode was inserted into the electrolyisis chamber but kept above the level of the KOH solution and the potentiostat was turned on just before the electrode was dipped into the solution. This process is necessary to prevent reactions that may occur at low potentials such as metal dissolution and oxidation.

The electrode was held at the potential of -1.3 V for 20 minutes to allow the system to equilibrate. Then the potential was swept at the rate of +2 mV/sec. The sweep was stopped every 100 mV at 1.2 V, 1.1 V etc. for two minutes to record the maximum current density at that overvoltage. The current passing through the electrodes varied continuously as the gas bubbles formed and covered part of the electrode surface. This was particularly noticable at low current densities as evolution of an individual gas bubble from the surface gave a corresponding jump in the current. The potential was swept down to -.001 V versus the RHE and back up again to -1.3 volts. The measurements were repeated about every 6 hours for a period of 4 days. It was possible to

obtain the same curve in the platinum and mixed samples for up to 2 days of electrolysis. However after this period there was an increase in the overpotential, also the surface of the electrode appeared tarnished. This suggests that the surface of the cathode becomes coated with impurities after prolonged exposure to the electrolyte. An EDAX analysis taken from the surface of the electrode in the SEM showed the presence of small quantities of copper; this was not present on the samples before the electrolysis. Tafel plots were obtained for platinum, iron and the mixed samples.

CHAPTER 5

ANALYSIS AND DISCUSSION

5.1 Introduction

The mixing process has been primarily characterized using the RBS technique; additional characterization has been done using the TEM. RBS spectra were taken from the evaporated films before and after mixing. The mixing was studied as a function of dose and temperature.

There are several parameters that may be used to characterize the mixing process. In many situations the choice of an appropriate parameter is extremely difficult. No single parameter appears adequate to characterize the mixing over the entire dose and temperature range. Several workers use parameters from the RBS spectra such as the full width half maximum (FWHM) of a peak to characterize the mixing (Paine et al. 1982). However sputtering effects make this approach unattractive. Picraux et al. (1982) use RBS spectra to estimate the number of atoms of the evaporated layer crossing over to the substrate. Averback et al. (1982) characterize the mixing using the width of the compound formed, but this is only useful in compound-forming systems.

When the atom relocation due to mixing is modelled along the lines of thermal diffusion, the mixing process can be characterized by an effective diffusion coefficient (D_{eff}). By studying the effect of temperature on the mixing process, a relationship between D_{eff} and temperature can be obtained. Arrhenius plots can be constructed to determine the activation energy of the processes, and hence the mechanism of atom relocation can be determined at a particular temperature. For thin buried markers the D_{eff} can be easily related to the FWHM (Paine and Averback 1985). However, for thick layers it is extremely difficult to use a diffusion-type model over the entire dose and temperature range (Averback et al. 1986), as the mixing takes place at different compositions and the damage profile and defect concentrations are not constant over the entire range of mixing.

In thermally diffused systems, there can be a considerable variation in concentration and a Boltzmann-Matano type analysis can be used to obtain diffusion coefficients as a function of concentration. It has long been established that diffusion in most metal systems occurs by the thermally activated motion of vacancies (Huntington and Seitz 1941). The concentration of vacancies, in a material at a particular temperature (T), scales relative to the reduced temperature (T_r), where T_r is (T/T_m), and T_m is the melting point of the material, so that, the diffusion coefficient of the alloy systems in fig. 5.1 will vary as

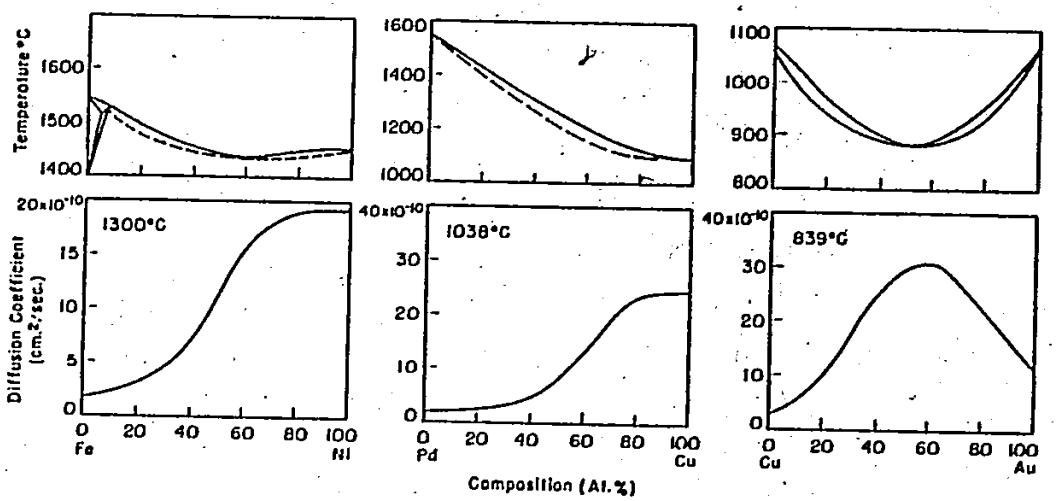

Figure 5.1 Figure shows the variation of diffusion coefficients with composition for the isomorphous systems, along with the phase diagrams.

shown. Averback (1986) suggests using the Boltzmann-Matano analysis for the profiles obtained by mixing. However, the vacancy concentration is not a function of composition in ion beam mixing but is related to the damage profile, and thereby to the depth from the surface; also, the boundary conditions for the Boltzmann-Matano analysis are not applicable to thin films. There are several atom relocation processes occuring simultaneously and these lead to profiles that are not akin to thermal diffusion profiles.

In this work, each run was carried out over four temperature intervals using four doses. This involved a total of 16 samples per run. Each experimental run was repeated three times to check the reproducibility. The widths of the evaporated films were not exactly the same as the electron beam evaporations could only be done with a repeatability of 10%. Hence, the spectra and composition profiles of samples mixed with the same dose and temperature do not overlap. However, empirical parameters such as the number of iron atoms crossing the interface have the same trend, and diffusion coefficients obtained are within experimental error. Electron microscopy is used to characterize the effect of dose and temperature on the structure and morphology of the films.

Electrodes are prepared using ion beam mixing and the catalytic effect is compared to samples of platinum and iron, and to iron samples coated with about 500 Å of

platinum. An increase in catalytic activity is found in the mixed electrodes; the unmixed platinum-coated samples also show an improvement in activity, but the improvement is short lived. RBS analysis done on the electrodes after polarization in the electrolytic cell show that the iron has come to the surface and formed an oxide layer burying the evaporated platinum film.

5.2 Characterization of the mixing process

5.2.1 Determination of composition profiles using RBS.

Figure 5.2a shows RBS spectra taken in the normal and sixty degree geometries, from a sample before mixing. The arrow indicates the channel that counts would appear at if iron were on the surface. Figures 5.3a and 5.4a contain five RBS spectra each, all taken in the sixty degree position. The spectra are taken at 298 and 523 K respectively. The dose varied from 4×10^{15} to 24×10^{15} Fe^+ ions per cm^2. The shapes of the platinum and iron peaks show a consistent change with increasing dose. The edge of the iron peak moves towards the surface and the height of the platinum peak reduces as iron atoms move into the platinum layer. Sputtering effects cause the area of the platinum peak to decrease. The spectra in fig. 5.5 show the effect of temperature on the mixing; the dose in these spectra is approximately 10^{16} Fe^+/cm^2. The rate of mixing increases with temperature.

Composition profiles can be generated from these

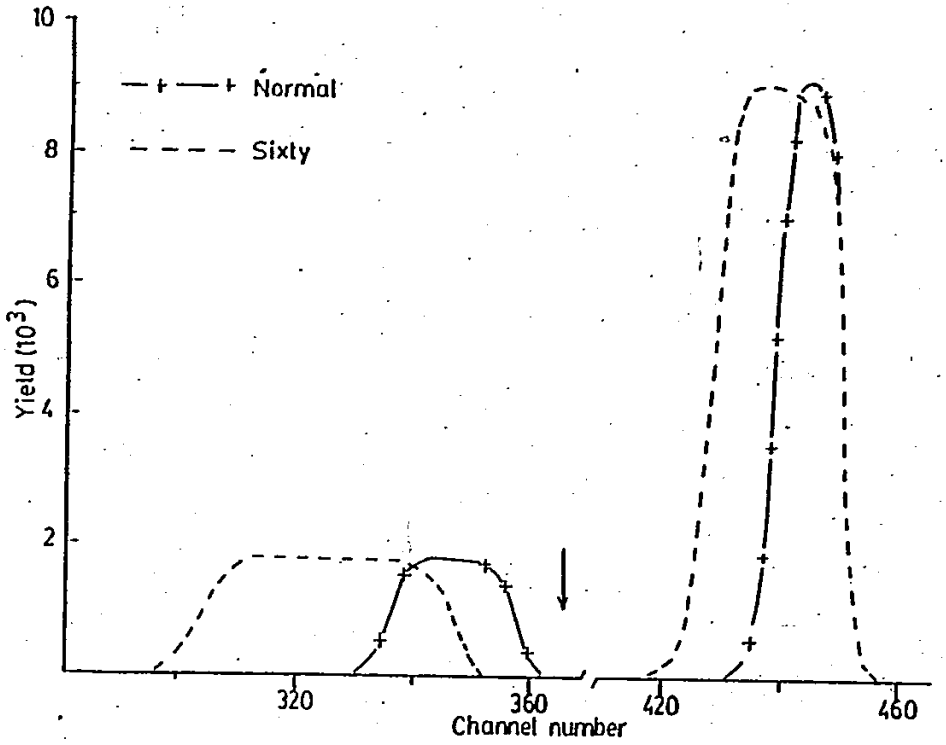

Figure 5.2 (a) RBS spectra at normal and sixty degree incidence of sample before mixing.

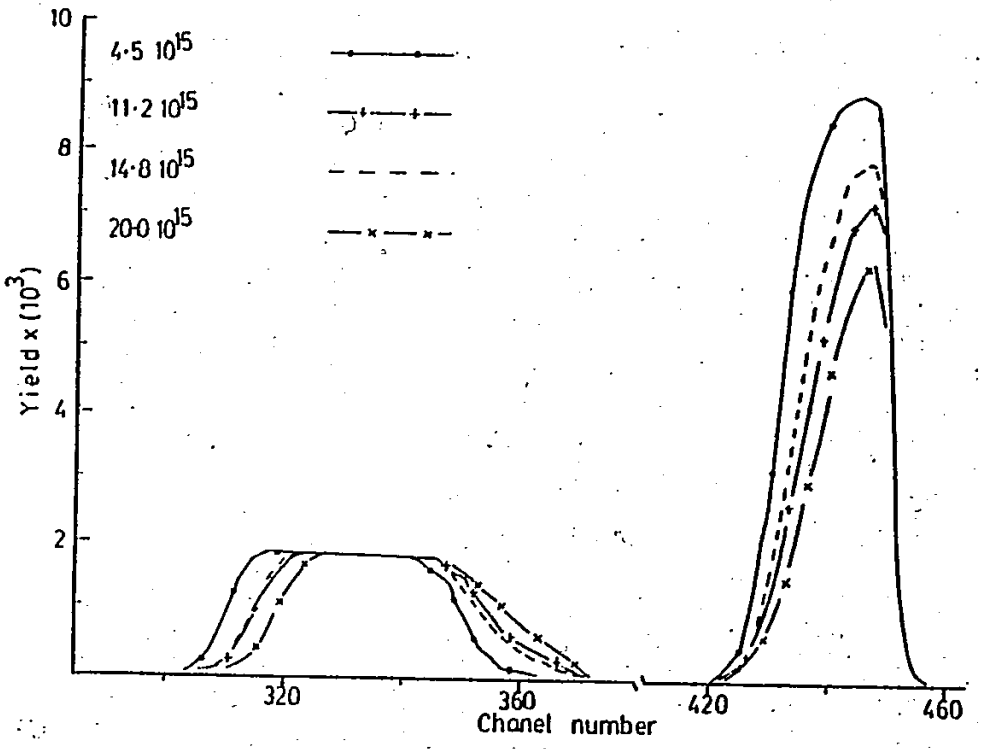

Figure 5.3 (a) RBS spectra of samples mixed at 298 K. Sixty degree configuration.

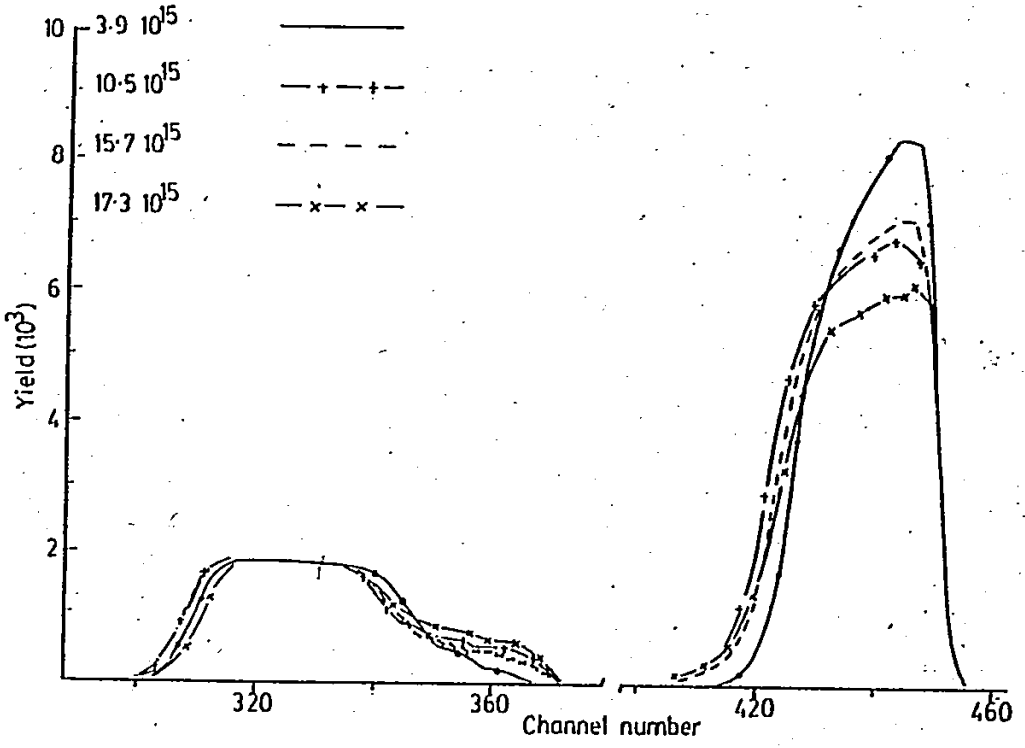

Figure 5.4 (a) RBS spectra of samples mixed at 523 K. Sixty degree configuration.

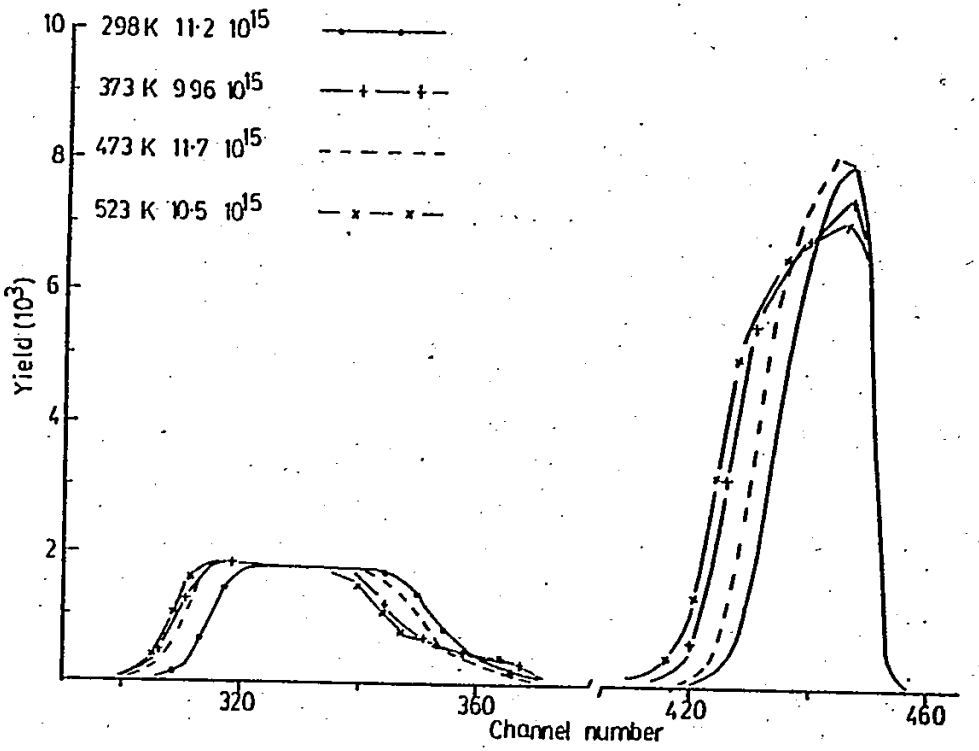

Figure 5.5 RBS spectra of the samples mixed as a function of temperature. The dose is ~10 $10^{15}/cm^2$.

spectra. An RBS computer simulation package used to generate the composition profiles along with some documentation and theory is presented in Appendix 1. An approximate test composition profile is input as layers with a definite stoichiometry. The width of the layers should be chosen such that the width of a channel (~4 keV) is equal to the energy lost in traversing the layer (~30 Å for Pt). Helium atoms backscattered from the atom layer on the surface of platinum towards the detector (through a 160 degree angle) should register the same energy; however, the spectra generated as a result of scattering from the surface atoms is shaped like a Gaussian distribution. This shape is caused by the finite resolution of the detector. The energy of the incident beam is not a unique quantity and has an energy variation that is determined by the design of the accelerator and the stability of the beam transport system. Helium atoms scattered from any layer of atoms within the sample will not have the same unique energy because there is a statistical uncertainty associated with the electronic energy loss that would cause energy straggling. The uncertainties in the above three processes cause any peak in the RBS spectra to be smeared out according to some Gaussian function. In order to obtain a composition profile the spectra have to be deconvoluted or the spectra can be simulated using the appropriate Gaussian "spreading function". Appendix 1 contains a few examples of simulated spectra and the experimental spectra

for a comparison.

The profiles generated from the spectra in fig 5.2a, 5.3a and 5.4a are shown in fig 5.2b, 5.3b and 5.4b respectively. The number of platinum atoms sputtered per cm^2 (N^{Pt}_S) is calculated by determining the number of platinum atoms remaining (N^{Pt}_M) and subtracting it from the number of platinum in the virgin sample (N^{Pt}_V). In those samples where iron atoms reach the surface, the number of iron atoms sputtered is calculated by assuming that platinum and iron have the same sputtering rates, and the rate of sputtering of a species is proportional to the concentration of that species on the surface. The total number of atoms sputtered is then associated with a sputtered thickness using Vegard's law. The number of iron atoms sputtered per cm^2 (N^{Fe}_S) is calculated by assuming that the Pt and Fe atoms sputter at the same rate and the amount of a particular specie sputtered is proportional to the surface concentration. If C^{Pt} is the surface concentration of Pt after mixing, the mean concentration of iron is taken as $(1 - C^{Pt})/2$. Then the number of iron atoms sputtered N^{Fe}_S is given by

$$N_S^{Fe} = \frac{1.0 - C^{Pt}}{2.0} N_S^{Pt} \qquad (5.1)$$

The thickness of iron (in Å) associated with the N^{Fe}_S is given by

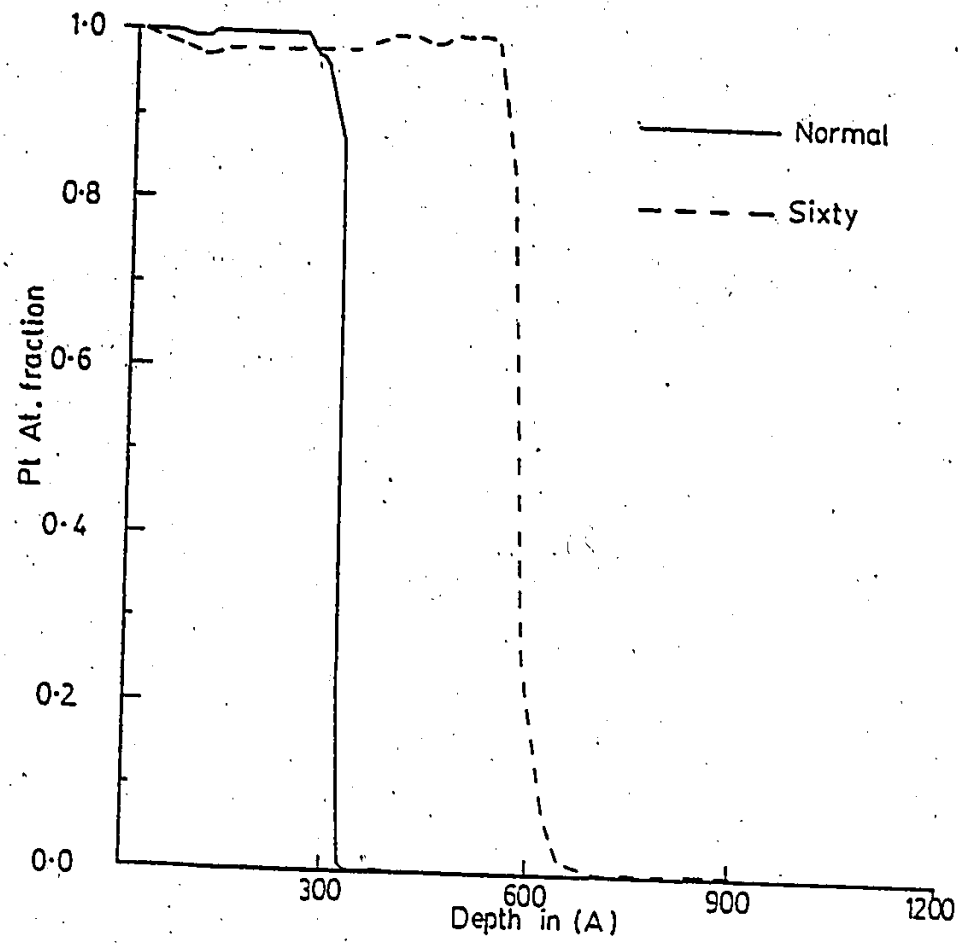

Figure 5.2 (b) Composition profiles generated from the RBS spectra in fig. 5.2 (a).

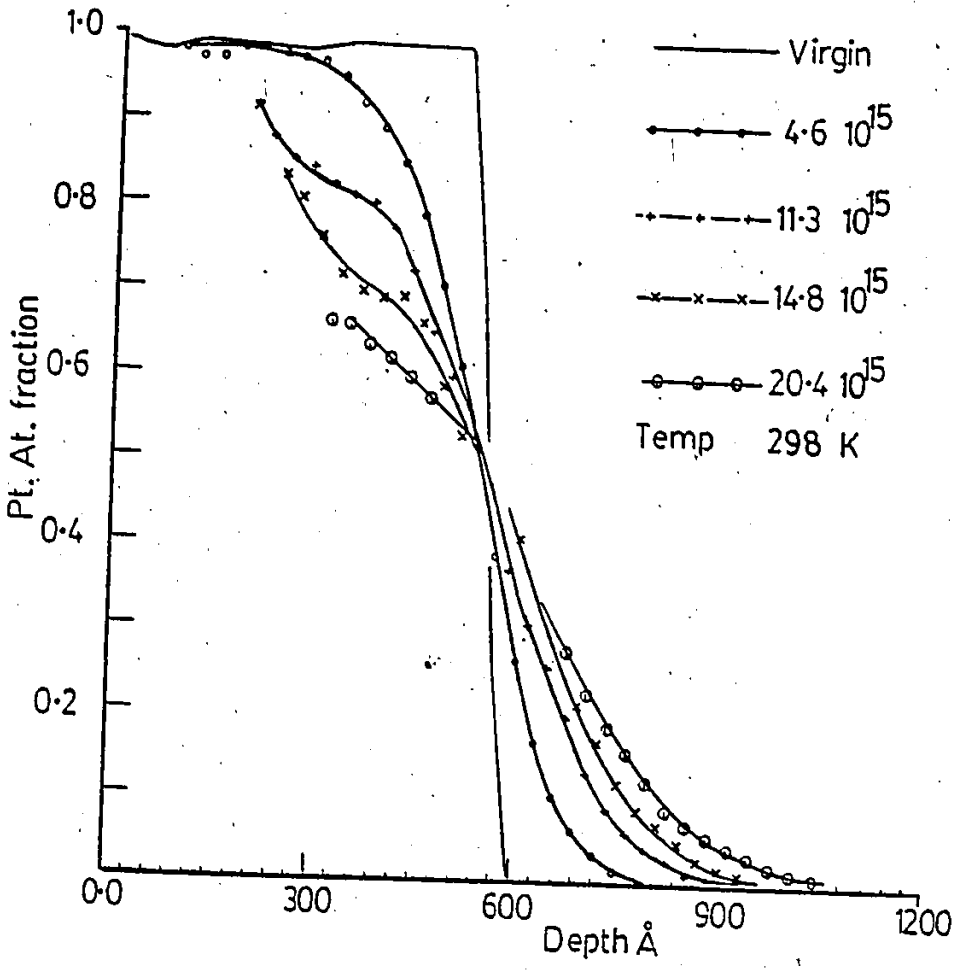

Figure 5.3 (b) Composition profiles generated from the RBS spectra in fig. 5.3 (a).

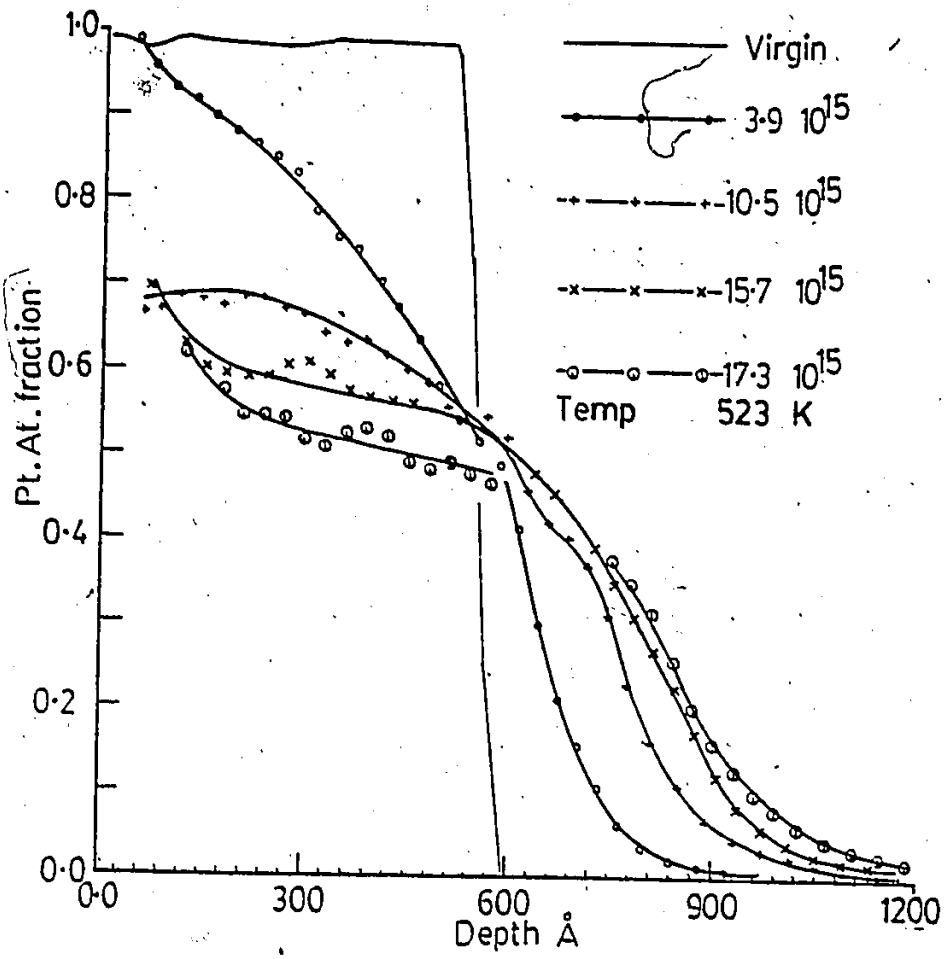

Figure 5.4 (b) Composition profiles generated from the RBS spectra in fig. 5.4 (a).

$$T_s^{Fe} = \frac{N_s^{Fe}}{N^{Fe}} 10^8 \text{ Å} \qquad (5.2a)$$

where N^{Fe} is the number of iron atoms per cm^3. Similarly for platinum the sputtered thickness associated with the ($N^{Pt}{}_s$) is given by

$$T_s^{Pt} = \frac{N_s^{Pt}}{N^{Pt}} 10^8 \text{ Å} \qquad (5.2b)$$

The total sputtered thickness is the sum of the above two equations. Each profile in fig 5.3b and 5.4b is then shifted to correct for the sputtered thickness, so that the point of zero depth refers to the unsputtered surface. The sputtering yield is higher for samples mixed below 373 K; the reduction in sputtering at elevated temperatures is caused by carbon containing gases in the vacuum chamber adsorbing on to the surface of platinum. It is expected that the profiles in fig 5.2b would have a sharp platinum iron interface; the slope associated with the interface is caused by the inaccuracy of the variance in the Gaussian function. The FWHM can be estimated from the width required for a composition change from 88% to 12% in the profile of the virgin sample. This amounts to 64 Å of platinum, which represents an electronic energy loss of about 8 keV. The error in the spreading functions is largely determined by the uncertainty in the calculated value of energy straggling for the helium beam as it penetrates the solid. The straggling formulation due to Bohr was

used. Harris and Nicolet (1975) have shown that the Bohr formulation underestimates the straggling for low atomic number targets such as aluminum, that the estimation is good for the mid-atomic number elements like nickel, and that the straggling is overestimated for heavy elements like gold. The data of Harris and Nicolet show that the error in the Bohr's straggling is about 20% at a depth of 500 A. This error increases with depth. However, since the error is the same for all the profiles, quantities like the activation energy will not be affected.

All the profiles have a smoothly decreasing composition after the interface. Before the interface, the composition is not a smoothly decreasing function. There is a sudden decrease in slope about 60 to 90 A below the sputtered surface that extends about 60 to 75 A. This indicates a local increase in the effective diffusion coefficient. This change in slope is clearly observable and reproducible in the spectra taken from samples mixed at 298 and 398 K. At higher temperatures where the diffusion is greater, the change in slope is less pronounced and the width of the region is greater.

Figure 5.6 shows the total energy deposited to recoil generation. The shape of the energy deposition function in platinum is strongly peaked having a maximum at about 95 A; the region around this peak will be highly damaged. The energy deposited into nuclear collisions (F_D)

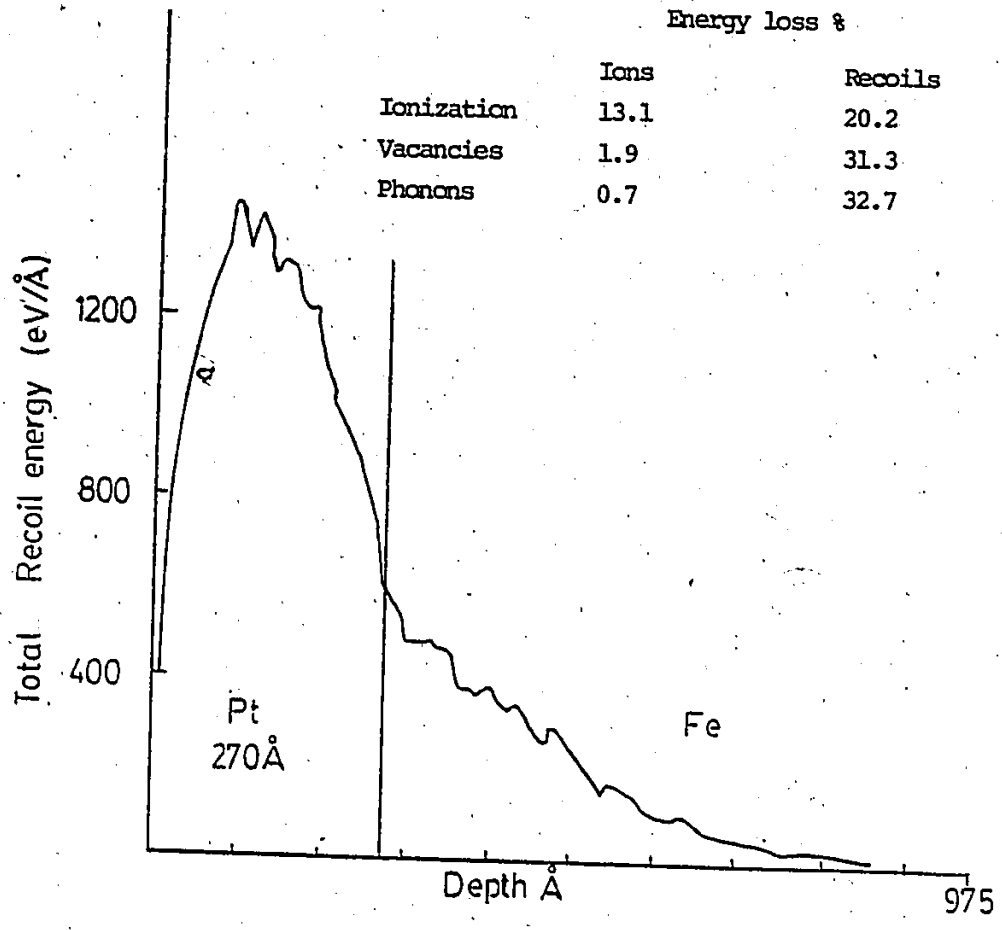

Figure 5.6 Computer generated TRIM profile showing energy deposited into recoil generation. The platinum film is 270 A and the iron film is 700 A. Only about 1/3 of the total energy deposited goes into vacancy production.

at the peak is about 480 eV/A; the mean F_D in platinum is about 270 eV/A. The D_{eff} and cascade mixing increase with increasing F_D and hence there is a decrease in slope in the composition profile around the region of maximum damage.

There appears to be a discontinuity of the slope at the platinum iron interface. The discontinuity is believed to result from the sharp change in the value of F_D at the interface (fig. 5.6). The structural change from fcc to bcc across the interface, will result in different mobilities for the impurity atoms. These discontinuities in the slope become less pronounced at higher temperatures where the importance of cascade mixing is diminished.

5.2.2 The mixing versus dose curve

Mixing is defined as the number of iron atoms crossing over the original platinum-iron interface to the platinum side. This parameter, used to characterize the mixing, is similar to that used by Battaglin et al. (1984). In RBS the electronic energy lost (ΔE) is given by

$$\Delta E = N\ t\ [\varepsilon] \qquad (5.3)$$

where N is the number of atoms per cm^3, t is the length of target traversed by beam, and ε is the areal stopping cross-section in units of eV cm^2. The values of ε are experimentally determined and are available in Chu et al. (1978). In order to determine t, it is necessary to determine N, (the number of atoms per cm^3. Meyer et al. (1981) have shown that

the lattice parameters in several ion beam mixed samples follow a relationship that deviates up to about 10% from Vegard's law. Ion beam mixing does not necessarily produce equilibrium phases which can have a sharp discontinuity in the lattice parameter with composition. Although deviations from Vegard's law may exist for the Pt-Fe system, the fact that the deviations in several cases are not large makes Vegard's law a reasonable assumption. Using Vegard's law the value of N can be determined.

The number of atoms crossing the interface (N_{Fe}) can be calculated from the composition profiles using

$$N_{Fe} = \sum_{1}^{T^{Pt}_{v}} (1.0 - C_i)\, N(C_i) \qquad (5.4)$$

where $N(C_i) = (N^{Pt}\, C^{Pt}) + [N^{Fe}\, (1 - C^{Pt})]$ is the number of atoms in the i^{th} layer. C_i is the atom fraction of platinum in the i^{th} layer $T^{Pt}{}_{v}$ is the thickness of the initial platinum layer and N^{Pt} and N^{Fe} are the number of platinum atoms and iron atoms per cm^3 respectively.

The number of iron atoms crossing the interface is plotted versus $dose^{1/2}$ in fig. 5.7. The graphs show that the mixing increases linearly with $dose^{1/2}$. Cascade theory (section 2.3.3) suggests that the motion of the atoms in a cascade are randomly directed allowing iron atoms to move in a direction opposite to that of the beam. The slope of the lines in fig. 5.7 changes between 373 K and 473 K, this

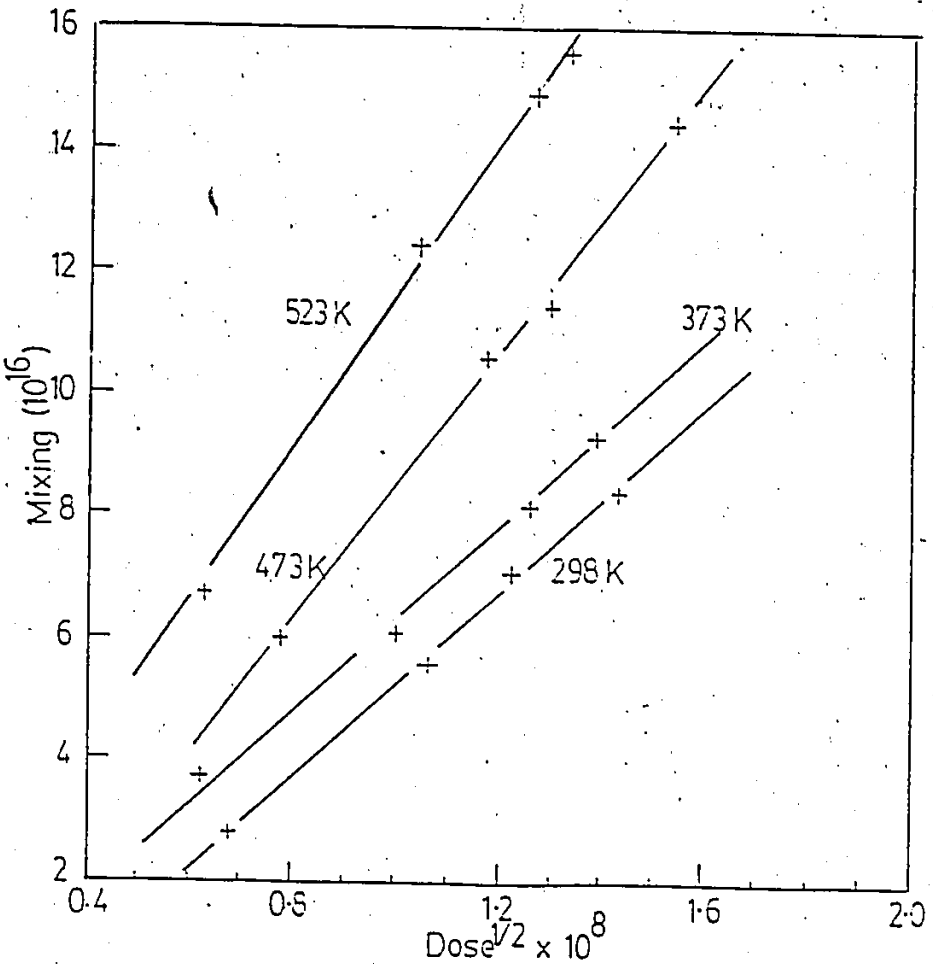

Figure 5.7 Mixing (defined in 5.2.2) versus (dose)$^{1/2}$.

suggests that there is a change in the mechanism associated with the mixing process. The vacancies are mobile in platinum above 420 K. Below this temperature, the atom movement in the platinum film takes place by the interstitial mechanism and by cascade mixing. However, above this temperature the vacancy mechanism can also operate.

5.2.3 The effective diffusion coefficient D_{eff}.

The thin film or the instantaneous source approximation is used to calculate the effective diffusion coefficients (D_{eff}).

$$c(x) = \frac{\alpha}{(4\ D_{eff}t)^{1/2}} \exp\left(\frac{-x^2}{4\ D_{eff}t}\right) \qquad (5.5)$$

where α is the total amount of solute and x is the depth. The slope of ln c(x) versus x^2 will give the D_{eff}. The diffusion coefficients calculated using cascade theory (setion 2.3.3) are about 10^{-14} to 10^{-15} cm^2/s, at a current density of $1\mu A/cm^2$. The implantation takes 15 to 60 minutes and the mean diffusion length in 15 minutes is expected to be about 300 to 900 Å. The thickness of the evaporated film is about 270 Å. Since the diffusion lengths are comparable to the thickness of the film, the thin-film approximation would be reasonable. The diffusion coefficients calculated for the smallest dose at 298 and 398 K, using the thin film approximation, are higher than those

calculated for subsequent doses. The mean diffusion lengths ($(D_{eff}\ t)^{1/2}$) for higher doses are much greater than 300 Å and the values of the diffusion coefficients calculated for the higher doses are almost the same, indicating that the thin film approximation is applicable.

An Arrhenius plot of D_{eff} versus the reciprocal of temperature is plotted in fig. 5.8. Above 473 K the activation energy is about 0.5 eV which is about half the vacancy diffusion activation energy for iron, indicating that the vacancy mechanism of diffusion is operational in the iron film (section 2.3.4). Below 473 K the activation energy is zero; hence, the atom relocation takes place by cascade mixing and possibly by the movement of interstitials. The activation energy for the migration of interstitials is expected to be less than 0.25 eV (Huntington 1953). Because of the error in the slope below 473 K, one can not be sure that the interstitial mechanism is operational.

Platinum iron bilayers were annealed thermally at 623 K and 673 K for 20 minutes. The anneals were carried out in a vacuum of 10^{-6} torr. RBS spectra taken from the thermally annealed samples and composition profiles similar to those in figures 5.3(b) and 5.4(b) were generated by using an RBS simulation code. The thin film approximation (equation 5.5) was used to determine the diffusion coefficients. These are plotted in fig. (5.8). The slope of the Arrhenius curve (Q) for the thermally annealed samples is ~ 0.78 eV.

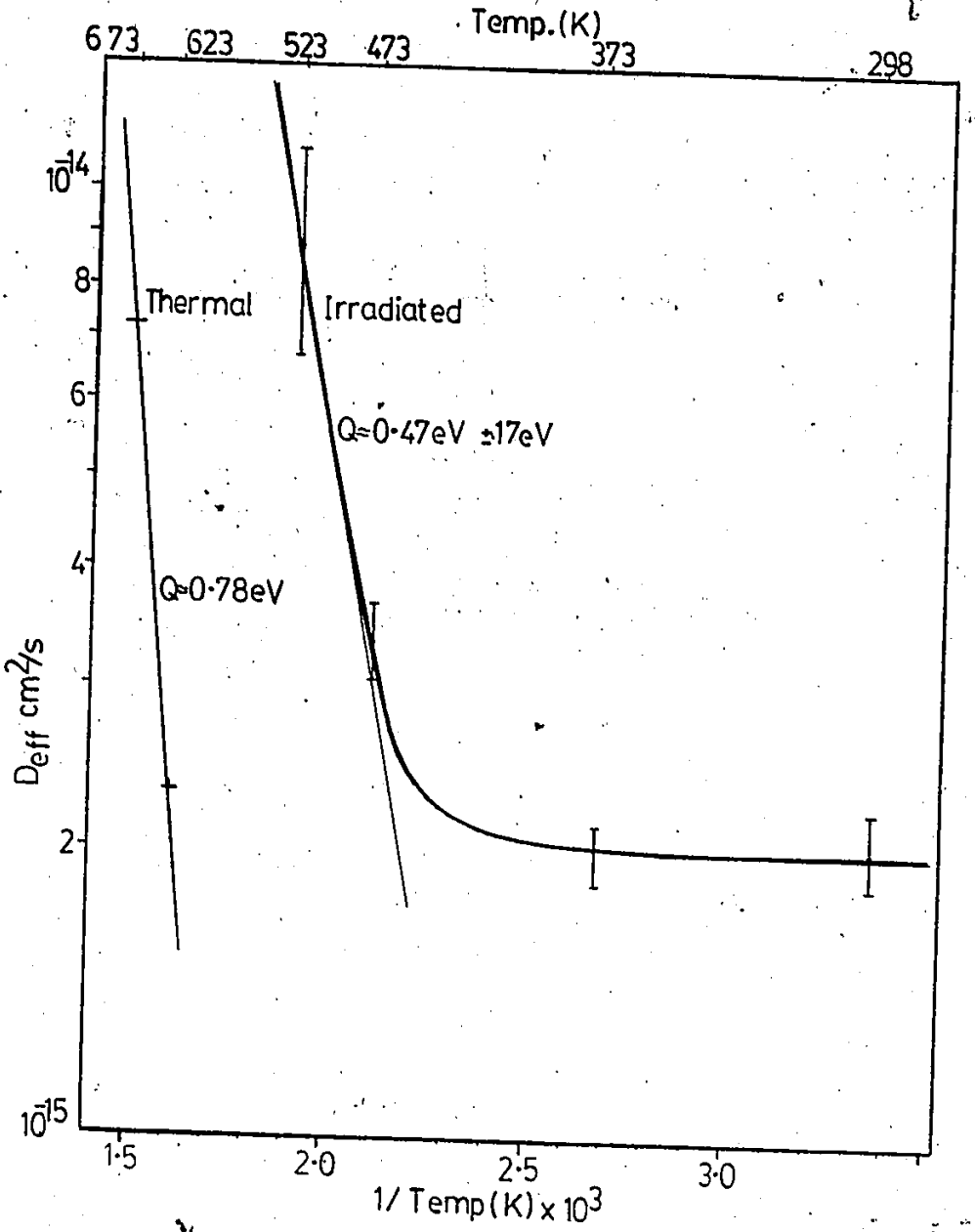

Figure 5.8 Arrhenius plot of D_{eff} versus 1/T.

This value is much smaller than the value of ~ 3.07 (Smithell 1983) given for the diffusion of Pt in γ-Fe in the temperature range 1233 K to 1533 K. No data is known to exist for the diffusion of Pt in α-Fe, which would be the case at 623 K and 673 K. The value of Q for Ni, Cu and Au in α-Fe are 2.69 eV, 2.95 eV and 2.7 eV respectively. The value of Q for Pt into α-Fe is expected to be in the range of $\sim$2.5 to 3 eV. The smaller value of $\sim$ 0.78 eV found in this work indicates that there is a substantial amount of grain boundary diffusion in the Pt-Fe couples.

There is extremely little work done on the formation energies of interstitials. Huntington and Seitz (1941) have estimated the activation energy for the migration of copper atoms in copper. To determine the approximate wave function (and hence the energy) associated with the electrons of a copper atom in copper, they assume that the "nearly free electron" approximation, which is applicable to the alkali metals, is also applicable to copper. Three migration modes were studied: the mechanism of direct exchange, the interstitial mechanism and the vacancy mechanism. To determine the formation energy of interstitials, they assume that an atom is taken from the surface and placed interstitially in the crystal. The electron gas in the crystal is compressed and there is an increase in electrostatic energy which amounts to 7.34 eV. There is also an increase of about 4 eV in the short range repulsive energy (ion core repulsion),

which depends strongly on the size of the atom. It is expected that the formation energy for a large platinum atom, atomic radius 1.39 Å, (Sargent-Welch periodic tables) in an iron lattice will be greater than that of an iron interstitial (1.26 Å). A platinum interstitial in the iron lattice will be unstable and will go into the substitutional position and the iron atom will become an interstitial. Hence the platinum will not be able to move by the interstitial mechanism in the iron lattice, while iron because of its smaller size, is favoured to move interstitially in platinum. Below 473 K, cascade mixing is mostly responsible for platinum atoms moving into the iron lattice, while iron can move into the platinum lattice by both cascade mixing and the interstitial mechanism. Johnson (1962) has studied the movement of copper atoms in copper. The migration mechanism is applicable to fcc structures and is shown in fig. 5.9. The interstitial atom is stable in the <100> dumbell configuration and moves by 90 degree rotations. The saddle point is located in the <110> direction and about 0.22a from the body-centered position in the fcc lattice (a is the lattice spacing).

Above 473 K, where the vacancies are mobile in iron, the platinum atoms penetrate deeper into the iron. For a dose of about 10^{16} Fe^{+}/cm^{2}, the depth below the interface where platinum has a composition of 10 at.% is plotted in fig. 5.10. The sharp change in slope after the 373 K implant

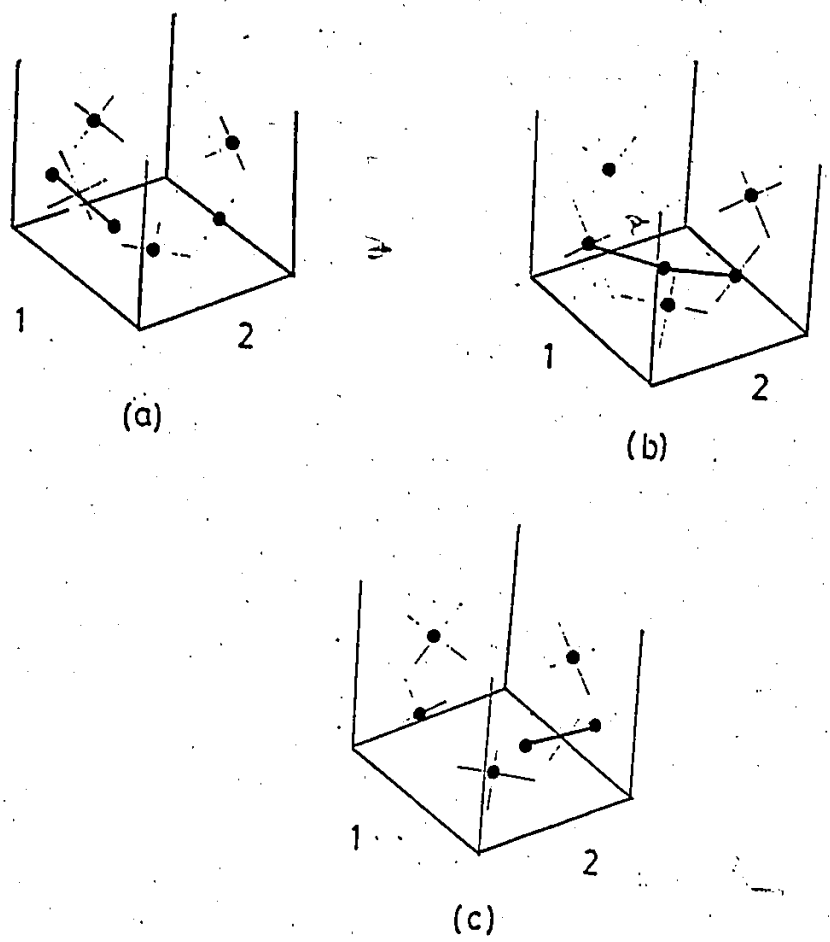

Figure 5.9 Shows the <100> split interstitial moving from face-1 in (a) to face 2 in (c) via the saddle point configuration in (b)

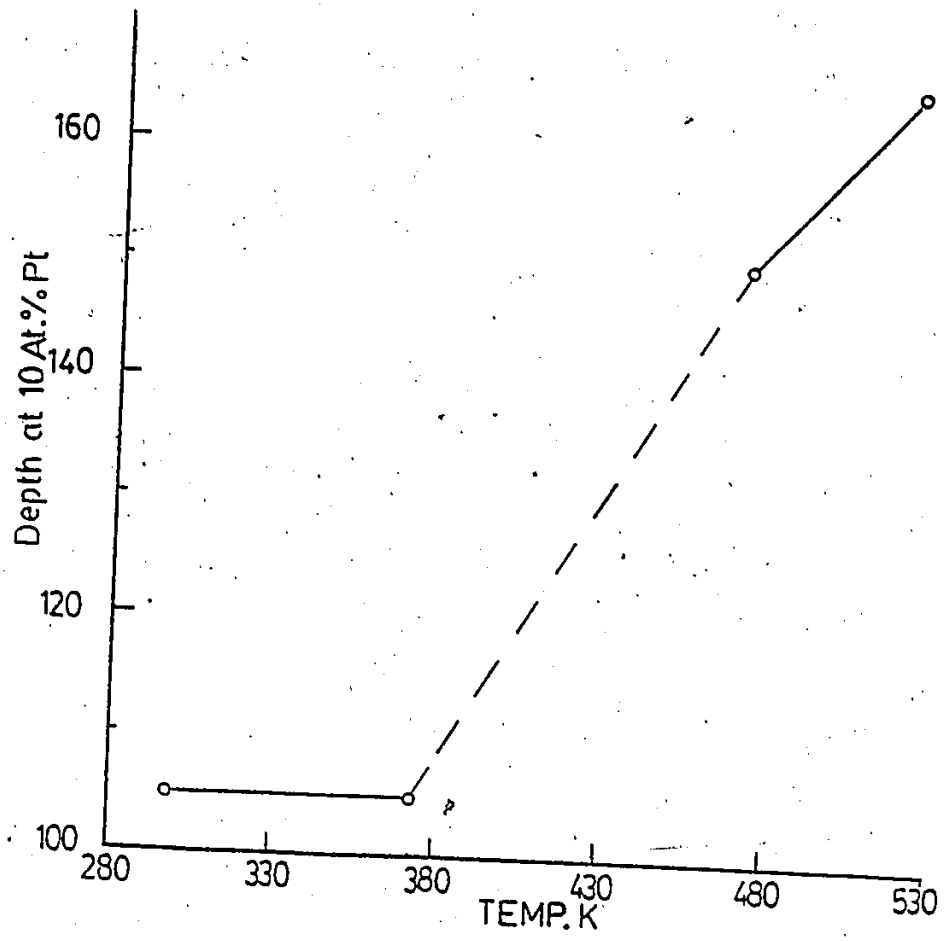

Figure 5.10 Depth below the orignal interface where the platinum fraction is 10% for a dose of ~$10_x10^{15}/cm^2$. The doses are $11.2x10^{15}$ at 298 K, $9.96x10^{15}$ at 373 K, $11.7x10^{15}$ at 473 K and $10.5x10^{15}$ at 523 K. Note that there is no increase in the penetration between 298 and 373 K.

is caused by the vacancy mechanism that can transport platinum deeper into iron.

5.2.4 Characterization of the bombarded films using electron microscopy

Morphological and structural studies were carried out on the platinum film using the TEM. In addition, the STEM was used to determine if there was any lateral variation in composition between different grains and between the grains and the grain boundary after ion bombardment. The TEM specimens consist only of the platinum-rich mixed surface layer as the iron and silicon dioxide are dissolved in the etch. Figure 5.11 shows the morphology of the evaporated platinum film.

Figures 5.12 and 5.13 show the change in morphologies that occur when the samples are subjected to the ion beam at 298 K and 523 K respectively. There is an increase in grain size with increasing dose. EDAX studies were done on the samples in the STEM. The results show no variation in composition between different grains or between any grain and the grain boundary. The composition appears to be uniform across the film. The samples mixed at a temperature of 298 K and below have a number of twins, while no twins are observable in the samples mixed at a temperature of 523 K and above. The twins are believed to be caused by stress in the platinum layer that comes about because of the more mob-

Figure 5.11 Bright field TEM micrograph of platinum film deposited on to the evaporated iron substrate at 298 K. The grain size is ~ 100 Å.

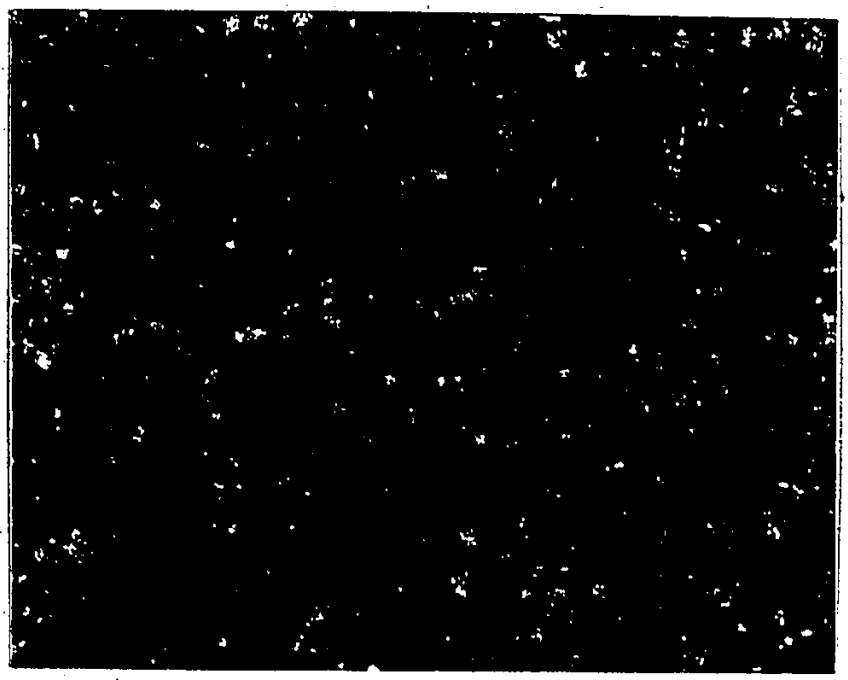

0.1 um.

Figure 5.12 (a) Bright field TEM micrograph of platinum iron alloy. The film was irradiated at 298 K using 120 keV Fe^+ ions for a dose of 4.5×10^{15}.

Figure 5.12 (b) Bright field TEM micrograph of platinum iron alloy. The film was irradiated at 298 K using 120 keV Fe^+ ions for a dose of 11.2×10^{15}. The micrograph shows that there are a number of twins, these appear as dark parallal lines.

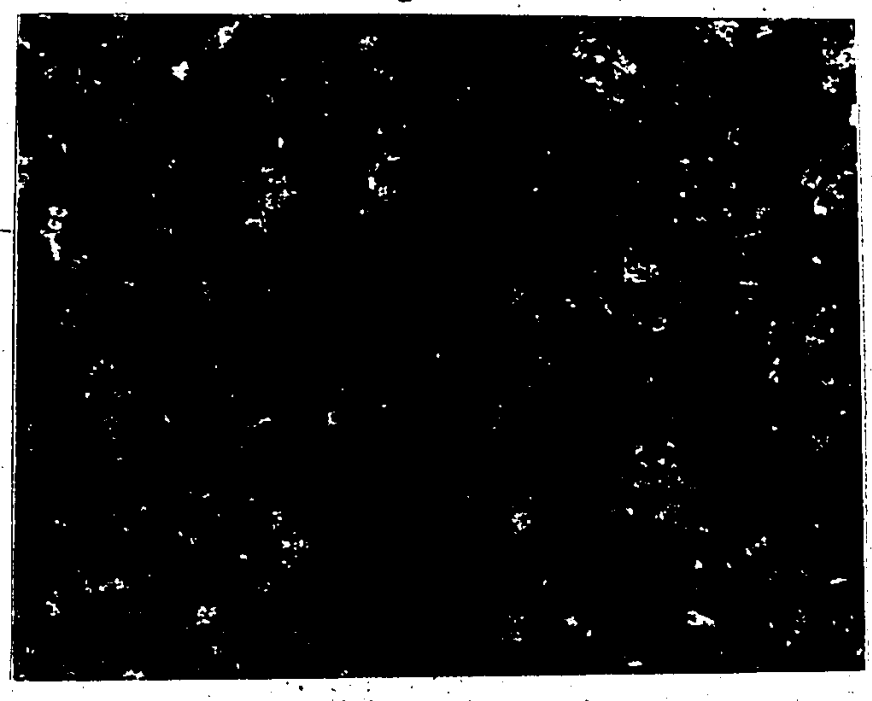

0.1 um.

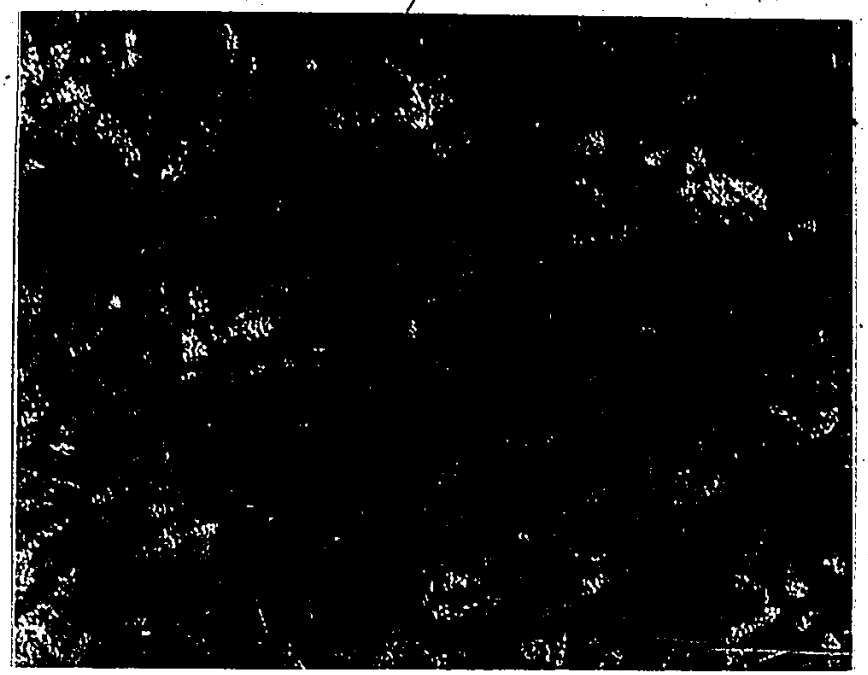

Figure 5.12 (c) Bright field TEM micrograph of platinum iron alloy. The film was irradiated at 298 K using 120 keV Fe^+ ions for a dose of 14.8×10^{15}.

Figure 5.12 (d) Bright field TEM micrograph of platinum iron alloy. The film was irradiated at 298 K using 120 keV Fe^+ ions for a dose of 20.0×10^{15}.

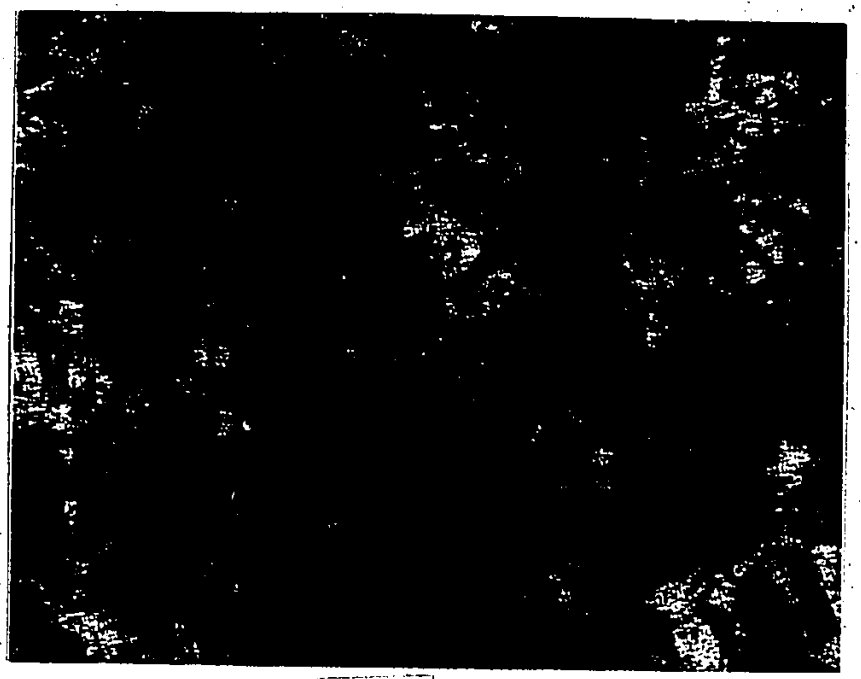

0.1 um.

Figure 5.12 (e) Diffraction patern of fig 5.12 (a). The diffraction patterns of figs. (b) to (d) were very similar showing a single phase platinum-iron alloy.

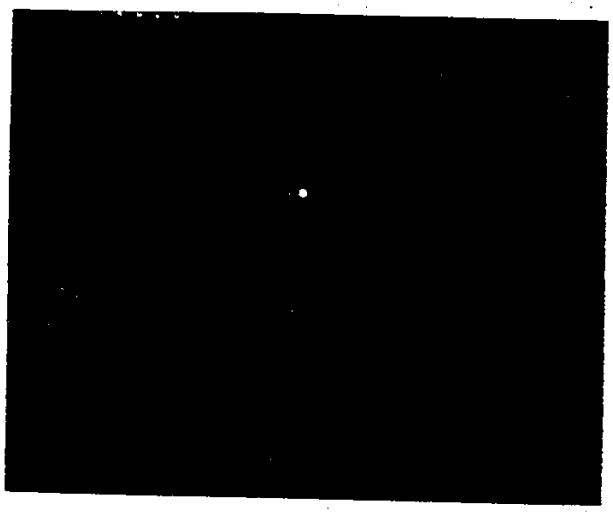

Figure 5.13 (a) Bright field TEM micrograph of platinum iron alloy. The film was irradiated at 523 K using 120 keV Fe^+ ions for a dose of 3.9×10^{15}.

Figure 5.13 (b) Bright field TEM micrograph of platinum iron alloy. The film was irradiated at 523 K using 120 keV Fe^+ ions for a dose of 10.5×10^{15}.

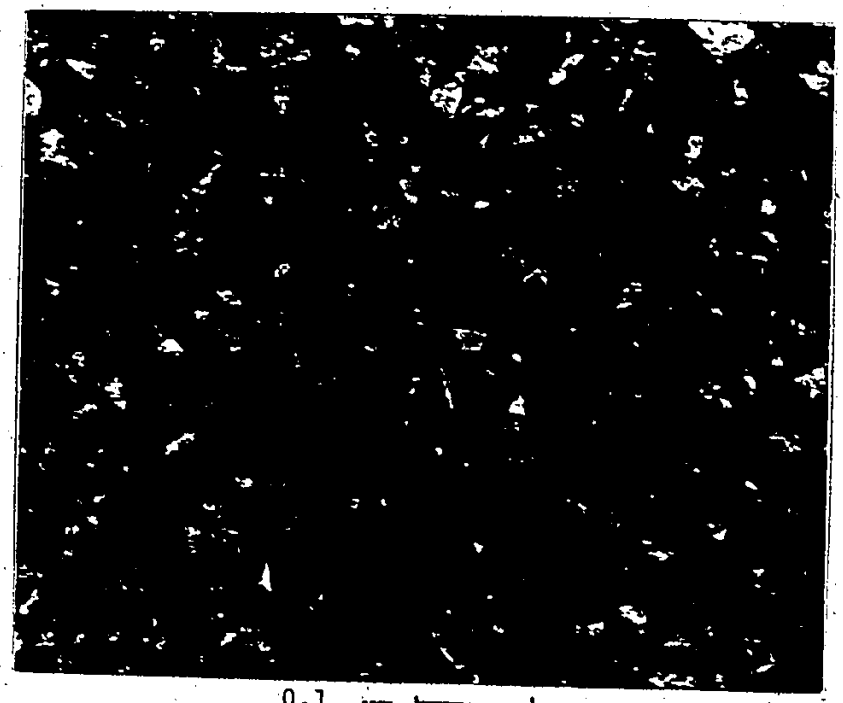

0.1 um.

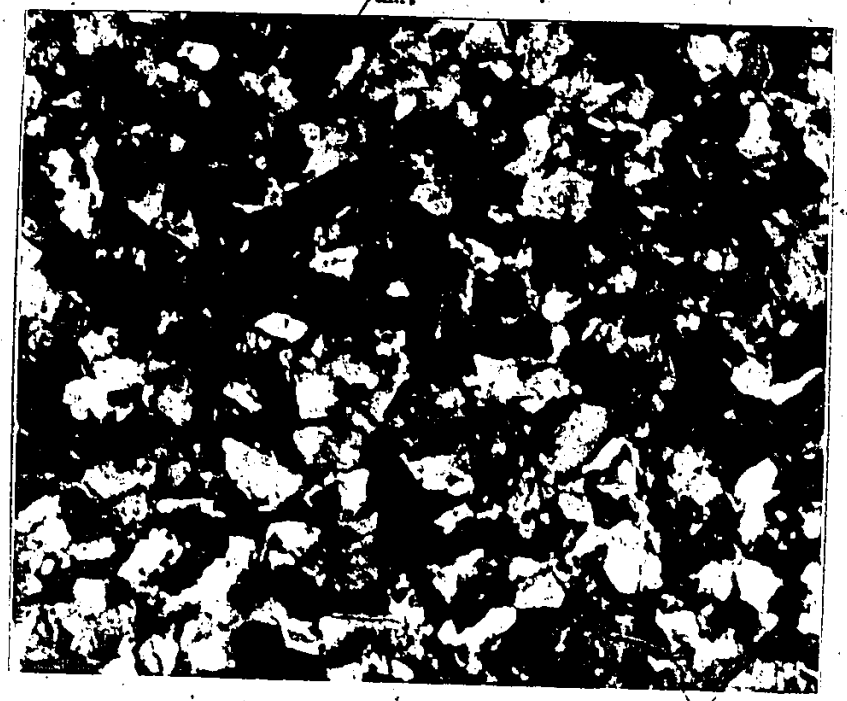

Figure 5.13 (c) Bright field TEM micrograph of platinum iron alloy. The film was irradiated at 523 K using 120 keV Fe^+ ions for a dose of 15.7×10^{15}.

Figure 5.13 (d) Bright field TEM micrograph of platinum iron alloy. The film was irradiated at 523 K using 120 keV Fe^+ ions for a dose of 17.3×10^{15}.

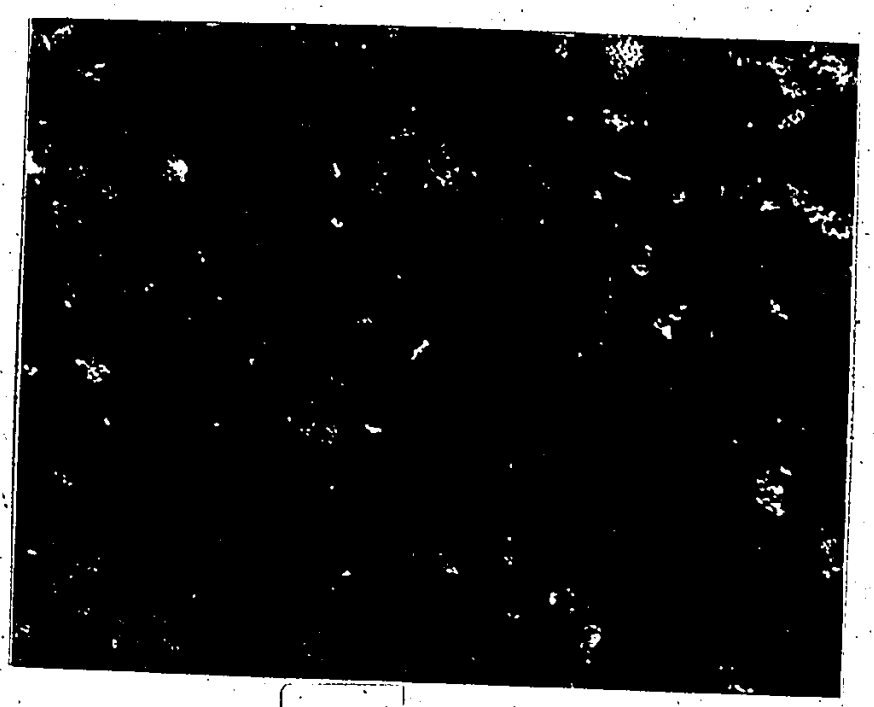

0.1 um.

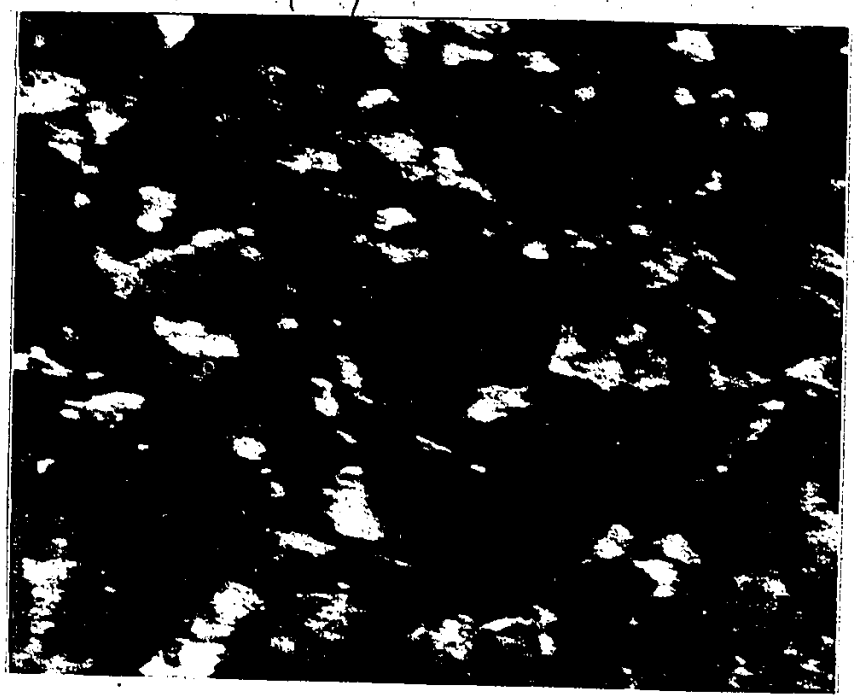

Figure 5.13 (e) Diffraction pattern of area in figure 5.13 (d) showing texture developed after bombardment.

Figure 5.13 (f) Diffraction pattern of fig. 5.13 (e) taken with a long exposure. Faint spots related to the Pt_3Fe superlattice are visible.

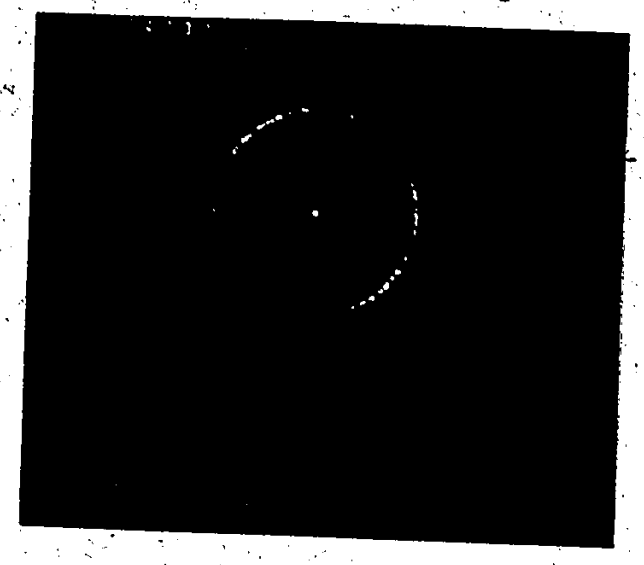

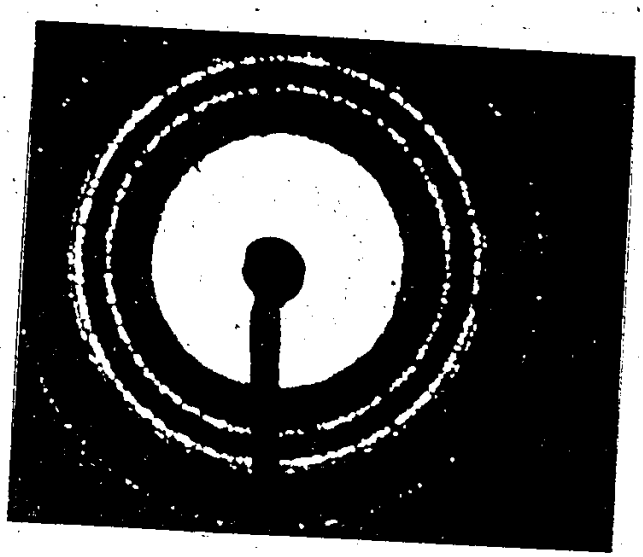

ile Fe atoms moving into the platinum layer. Figure 5.12 and 5.13 show that there is an increase in grain size with dose.

The bright field micrographs from figures 5.12 and 5.13 were used to estimate the mean grain diameter. The procedure is outlined in the Metals Handbook (Volume 8, 1961). The average grain diameter (GD) is given by

$$GD = L_T / PM \qquad (5.6)$$

where L_T is the total test-line length, P is the number of grain boundary intersections, and M is the magnification. The mean grain size for the virgin sample is estimated to be $\sim$104 Å. In figure 5.14 the mean grain diameter is plotted versus dose and the temperature at which the mixing was carried out. The graph in figure 5.14 shows that there is an increase in the mean grain diameter with dose. The mean grain size for samples mixed at a temperature $>$ 473 K generally lie on the higher curve. Although there appears to be some effect of the temperature on the mean grain diameter, this effect does not appear to be very large. For a dose of 20×10^{15} and a temperature of 373 K the mean grain size is $\sim$ 400 Å; while at 523 K and the same dose the mean grain diameter is estimated at $\sim$ 480 Å.

At lower temperatures, ie. at and below 373 K, the diffraction patterns show no evidence of any texture or any indication of the formation of any intermetallic phase (fig. 5.12). For temperatures at and above 473 K, and a dose greater than 10^{16} Fe^+/cm^2, there appears to be a considerable

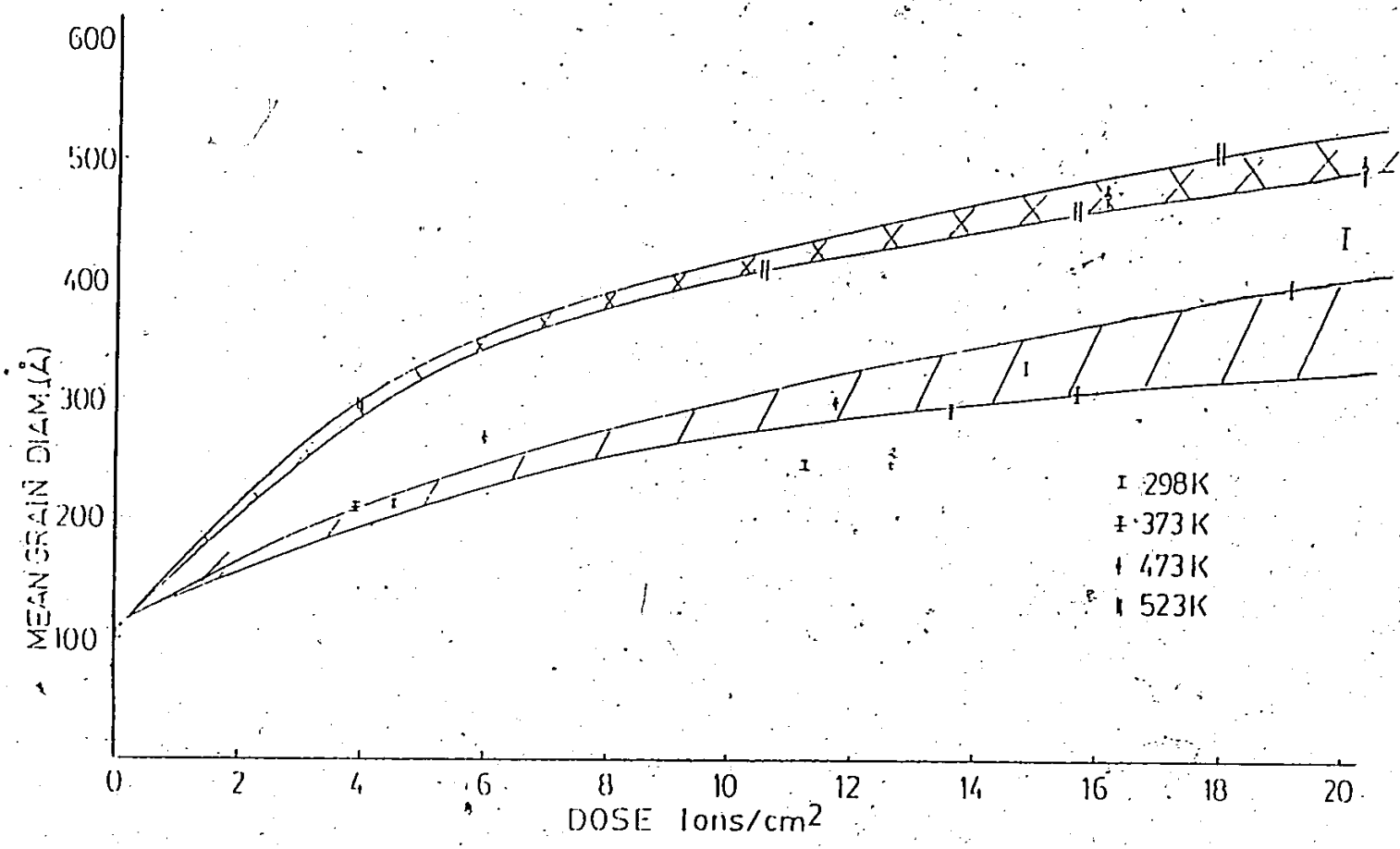

Figure 5.14 Graph shows the mean grain diameter of the bombarded films as a function of dose at different temperatures. The results appear to fit within two bands. One for temperatures <373 K and one for temperatures >473 K.

texture formed and there is a clear indication of the formation of an intermetallic ordered phase (fig. 5.13). However, there is no noticeable texture associated with the intermetallic reflections in the diffraction pattern. The intermetallic spots consist of a few scattered disallowed reflections, indicating that the whole film is not ordered. In films that were thermally annealed at 623 and 673 K, the reflections due to the ordering appear to form a continuous ring, indicating that the ordering takes place throughout the film; these films do not have a texture (fig. 5.15).

Cascade mixing is not expected to cause ordering effects as the atom relocation process is random. Iron interstitials are expected to be mobile in platinum at 298 and 373 K, while the vacancies are not mobile in platinum and there is no evidence of any ordering. At 420 K and above the vacancies are mobile in platinum and there is some evidence of an ordered phase; however the amount of ordering is not extensive. In the annealed samples where atom motion takes place by the movement of vacancies and by grain boundary diffusion, the amount of ordering is found to be extensive. It appears as though the interstitial motion is not conducive to the formation of an ordered phase, and that the ordering takes place by the vacancy mechanism. At 473 K and above the vacancy mechanism would cause some ordering; however, the cascade mixing would tend to limit the extent of ordering.

Figure 5.15 Bright field TEM micrograph of platinum-iron alloy annealed at 673 K for 20 minutes. The diffraction pattern shows faint lines due to the Pt_3Fe superlattice.

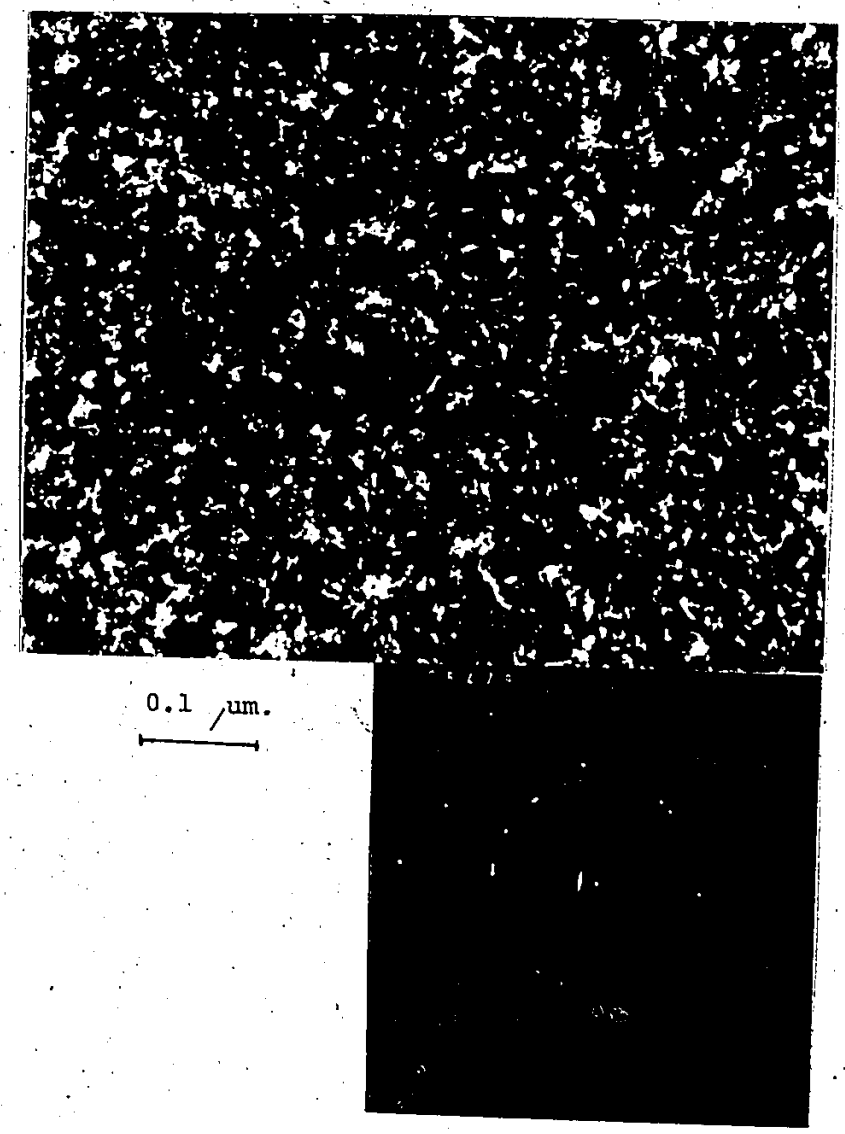
0.1 um.

Loiu and Wilkes (1979) have shown the steps required for the ordering reaction to take place by the vacancy and interstitial mechanism. These are shown in fig. 5.16a and b respectively. The ordering reaction by the vacancy mechanism requires a two step process as shown in fig. 5.16a. The interstitial mechanism requires three atomic steps for the ordering reaction to take place, however both species must be mobile for the ordering reaction to take place. If the B atom is in an α site and cannot move by the interstitial mechanism, the ordering reaction cannot take place by the interstitial mechanism. The fact that there is no ordering at and below 373 K supports the belief that only one species, i.e. iron, moves by the interstitial mechanism in the platinum-iron alloy, while above the vacancy migration temperature ordering occurs, as both iron and platinum atoms can move by the vacancy mechanism.

5.3 Electrocatalysis Studies in Alkaline Solution

5.3.1 Tafel curves for the cathodic reaction

Tafel curves for the cathodic reaction are presented in Fig. 5.17a and Fig. 5.17b. The curves in fig. 5.17a are for an iron electrode, and those in fig. 5.17b are for iron, platinum, platinized platinum and the mixed samples. The curves for iron are the average of five samples. Polarization measurements were carried out for over 72 hours in each case. The polarization measurements showed a considerable

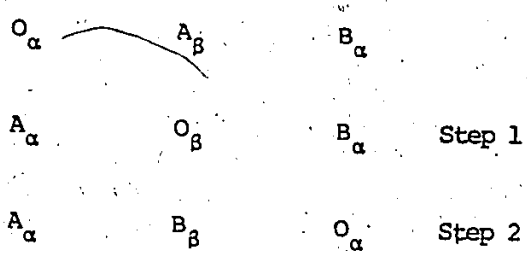

Fig 5.16 (a)

The vacancy (O) jumps from left to right in a lattice made up of two sub-lattices (α and β sites) resulting in an ordered lattice, with A atoms in α sites and B atoms in β sites. The ordering process requires two jumps.

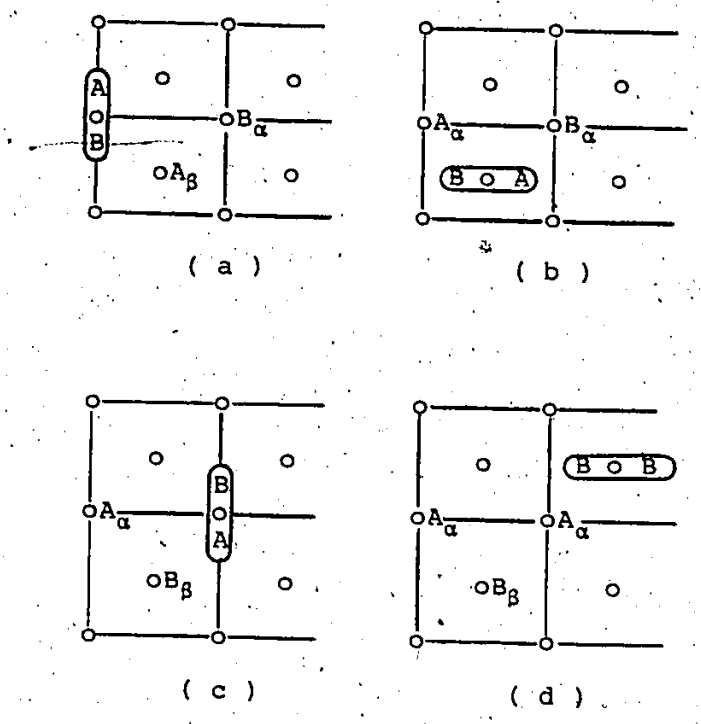

Fig 5.16 (b)

The interstitial dumbell is ringed. As the interstitial atom moves (fig. (a) to fig. (d)) the A atoms end up in the α sites (linked by lines) and the B atoms end up in the β sites.

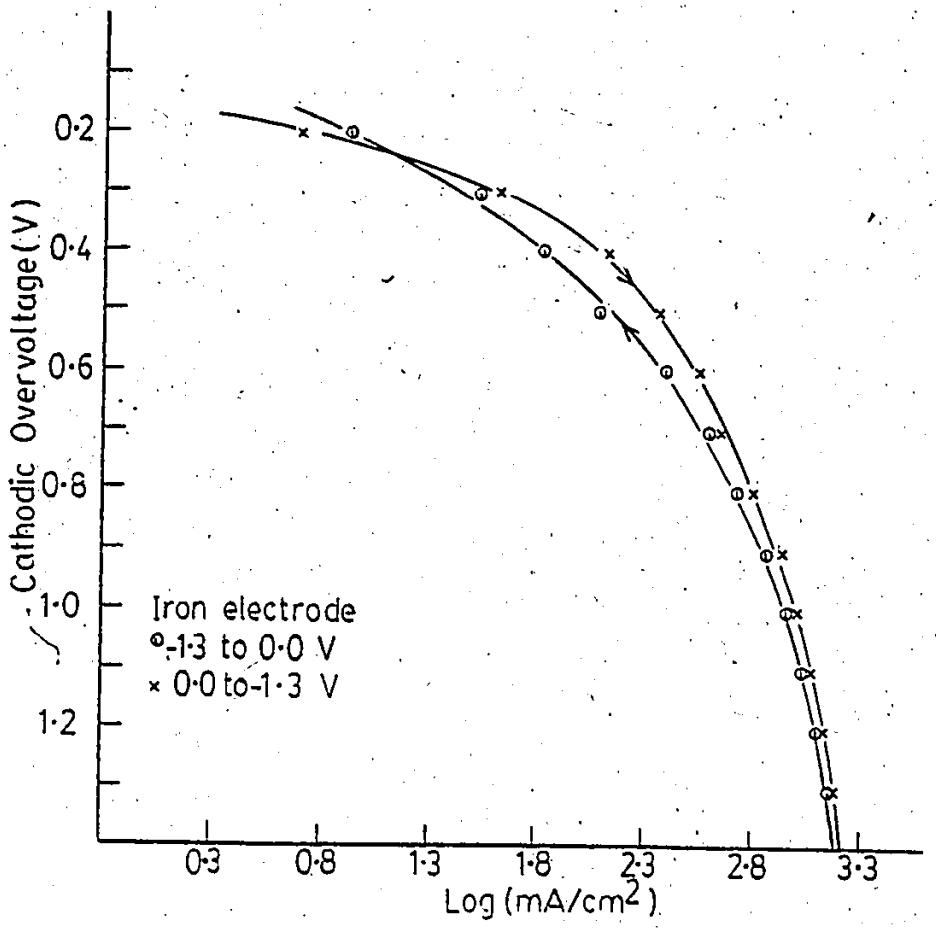

Figure 5.17 (a) Tafel plots for iron electrode.

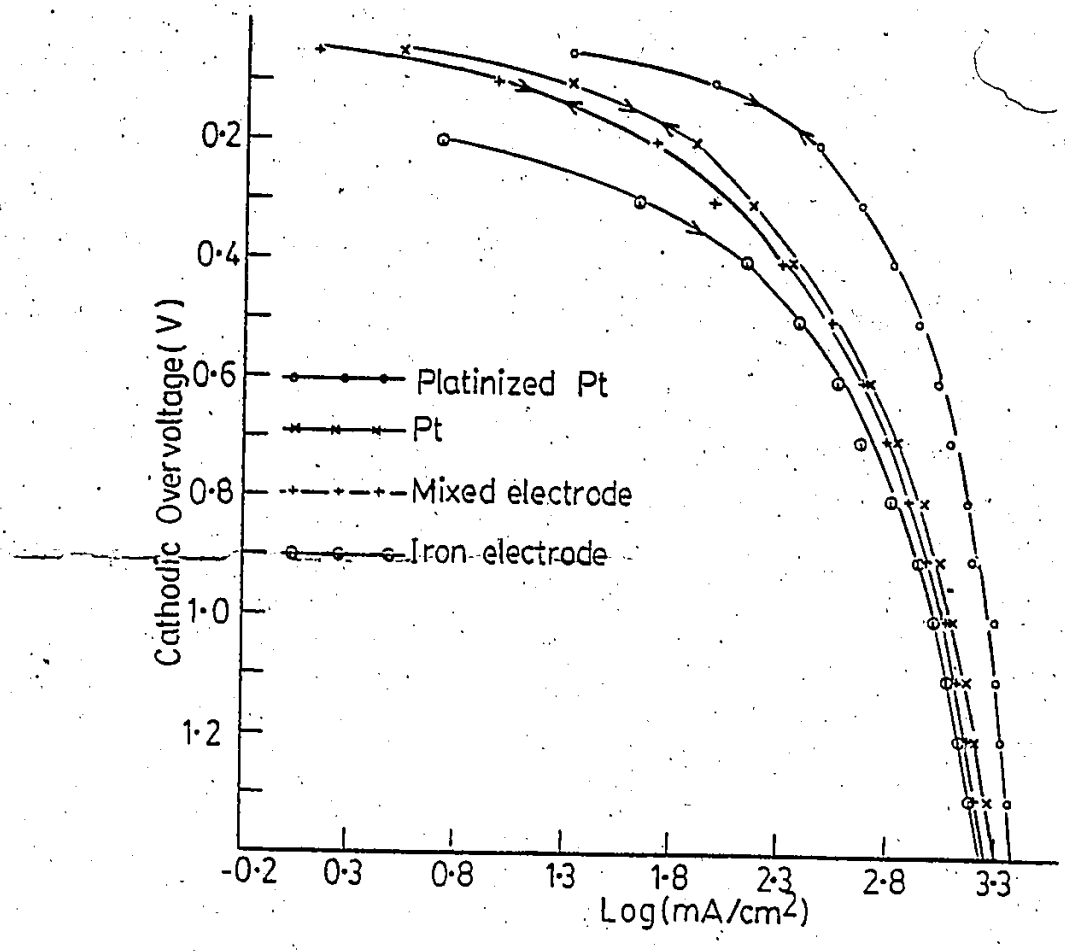

Figure 5.17 (b) Tafel plots for Platinized platinum, platinum, mixed electrode and the iron electrode.

amount of hysteresis. The voltage was scanned from - 1.3 V to 0.0 RHE, then back to -1.3 V. There appears to be a reduction in overpotential in the negative scan. After about 48 hours the electrode surface appeared to have some coloration, even though the electrolyte had been purified for 15 days prior to the polarization scans. EDAX was done on the surface of the iron electrodes in the SEM. Along with the iron there appeared to be traces of copper; a substantial oxygen signal was also observed. The copper is believed to have electroplated out from the solution, contaminating the surface of the electrode. Silverman (1982) has recently modified the EMF-pH diagram of Pourbaix (1974) to show that there is an $Fe(OH)_2$ phase formed around -0.6 V SHE. Gernov et al. (1974) have done Mossbauer studies on iron electrodes at cathodic potentials in a cell. The cell contained 5 N potassium hydroxide. Their results suggest that the iron electrodes form a β-FeOOH phase which, at a slightly negative potential, gets converted to an $Fe(OH)_2$ phase. At more negative potentials a part of the $Fe(OH)_2$ phase is converted to Fe, but the remainder of the $Fe(OH)_2$ remains stable for a prolonged period. The reduction in overpotential is believed to occur because of surface roughening caused by the formation of the oxide layer.

Electrodes were prepared by the evaporation of platinum onto iron disks after the surface oxide on the iron was reduced in hydrogen. The thickness of the platinum layer was

250 Å. In addition, five samples with 500 Å of platinum were prepared and tested in the cell without any ion beam mixing. The unmixed samples initially showed a catalytic improvement but this effect did not last more than one scan. A considerable hysterysis effect was also observed. RBS spectra taken after polarization showed that the platinum layer was buried and a layer of iron oxide had formed on the surface. Subsequent curves were similar to those obtained for pure iron. Disks with 250 Å of platinum were mixed, using a 120 KeV Fe^+ beam. The dose was varied from $5x10^{15}$ to $2x10^{16}$ ions per cm^2. It was found that the samples mixed with $5x10^{15}$ ions per cm^2, which would produce a platinum-rich surface (as seen in fig. 5.3b), lasted longer than those mixed with a greater dose. The samples mixed with a dose of $5x10^{15}$ Fe^+/cm^2 remained stable for up to 48 hours. The polarization curve was similar to that of platinum with no observable hysteresis. After 48 hours in the cell, some hysteresis was observable and the measured overvoltage curve was between the iron and the ion beam mixed values. RBS measurements were caried out on the samples before and after polarization measurements; the spectra are shown in fig. 5.18a and 5.18b respectively. The spectra in fig. 5.18a were taken after using the mixed electrode for over 72 hours in the cell. The spectra show that the surface is partially covered with iron oxide; however there is still a substantial amount of platinum present on the surface. Samples were also mixed at 200°C

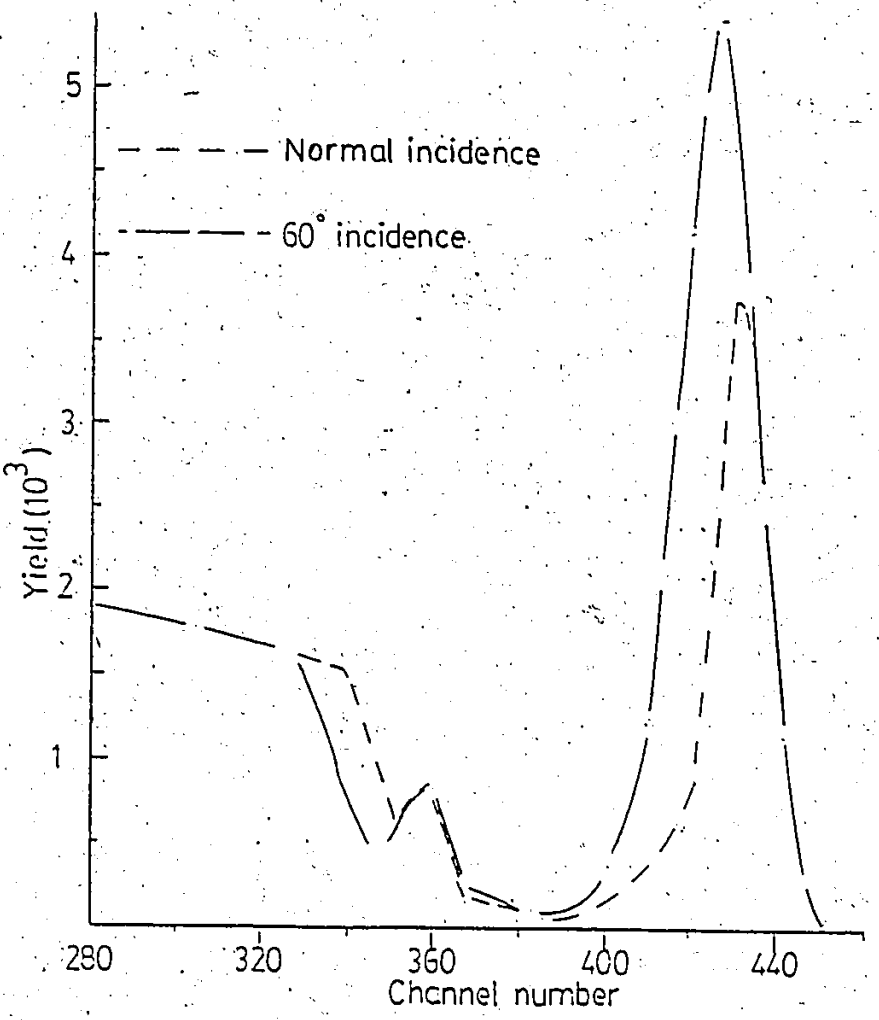

Figure 5.18 (a) RBS spectra of mixed electrode after 72 hours polarization in the electrochemical cell. The peak between channels 400 and 440 is due to platinum, while the peak around channel 360 is due to iron on the surface of the electrode. The edge at channel 340 is due to He+ ions backscattered from iron which is below the platinum.

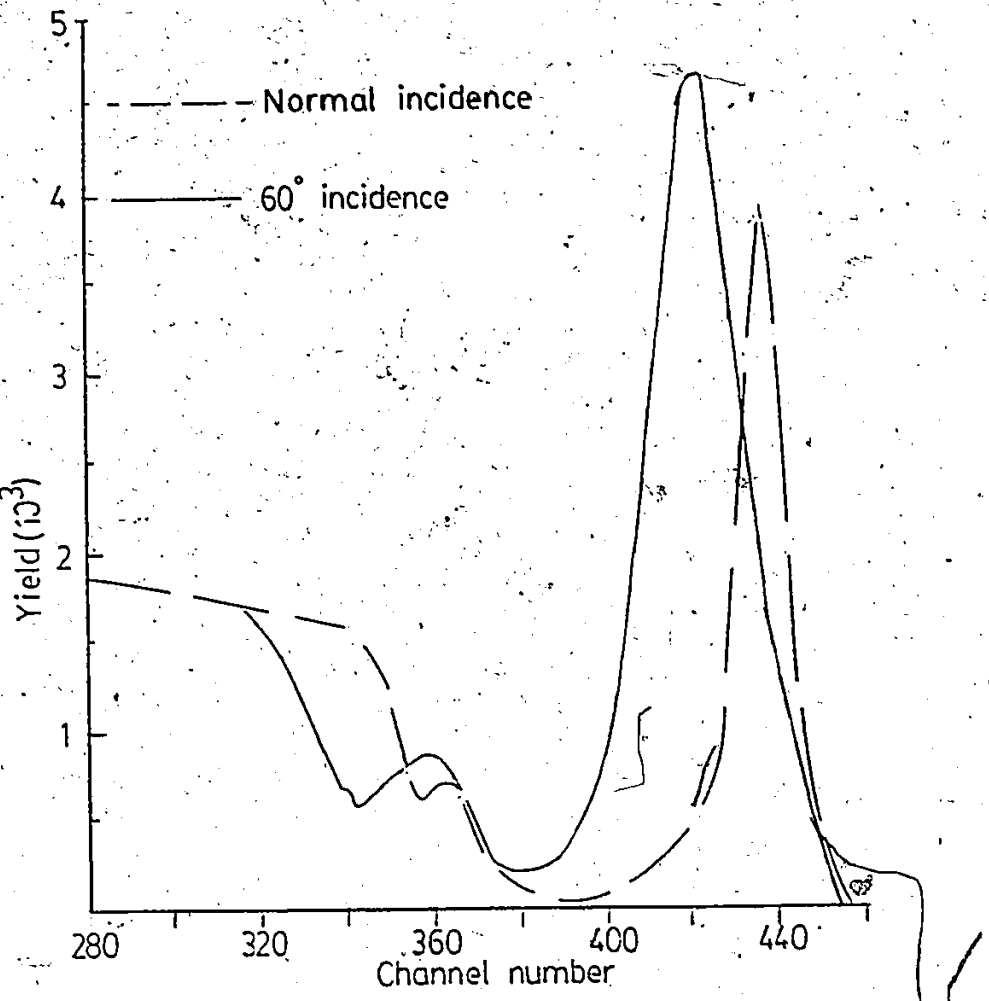

Figure 5.18 (b) RBS spectra of (unmixed) electrode with evaporated platinum after 24 hours polarization in the electrochemical cell. The peaks between channels 400 and 440 are due to platinum. The peak at channels 360 is due to iron atoms which have covered the surface of the electrode.

with a dose of 5×10^{15} Fe^{+}/cm^{2}. The polarization results were similar to those obtained for the samples mixed at room temperature.

For a comparison, polarization measurements were carried out on pure platinum and platinized platinum. The results are included in fig. 5.17b. RBS measurements show that the surface is substantially covered with platinum after 72 hours. Although there is some coloration, there is no observable change in the Tafel curve. EDAX measurements indicate that there is some copper on the surface. A small anodic pulse (up to 0.2 V and a duration of 0.1 msec.) was used to clean the surface of the platinum. The surface of the platinum appeared to be completely clean after three such pulses. When anodic pulses were applied to the mixed electrodes to remove the surface contaminants, the colour became black, and there was a considerable reduction in overpotential. Subsequent SEM micrographs showed that the sample had been severely pitted fig. 5.19. The change in colour and reduction in overpotential is believed to be due to the pitting action.

The reduction in overpotential in the mixed samples at a current density of 100 mA/cm^{2} is about 26% relative to pure iron, while the reduction for pure platinum is about 34%. The large reduction in overpotential for the platinized platinum is believed to come about because of the large surface area of the platinized platinum electrode.

Figure 5.19 SEM micrograph of mixed electrode after anodic pulse. (M x 2400)

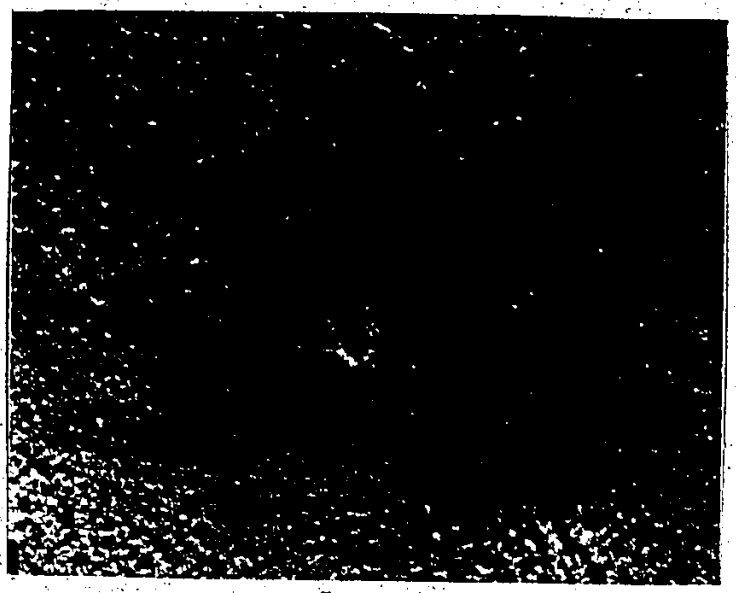

5 um.

CHAPTER 6

SUMMARY AND CONCLUSIONS

In order to study the ion beam mixing process it was found necessary to make samples that are free of contaminants and that do not have an oxide layer at the interface. Initial mixing experiments carried out without using the hydrogen reduction unit had an oxide layer on the surface. It was found that the oxide layer acts as a barrier to the mixing process; the rate of mixing is lower and the data is not reproducible. An evaporation chamber, integrated with a hydrogen reduction unit was developed, making it possible to produce samples without an oxide layer at the interface.

There are several atom relocation process that take place in ion beam mixing. In order to study the different atom relocation processes, experiments were designed by which the various mixing processes could be separated. At low temperatures (< 20 K) cascade mixing dominates in the platinum iron system (Bottiger et al. 1983). In this work the ion beam mixing of the platinum iron system has been investigated over a temperature range from 298 K to 523 K.

It was found that the transition to a predominantly thermally activated processes occurs at about 423 K; above this temperature, atom relocation can also take place by the vacancy mechanism. This fact is also illustrated by the increased penetration of platinum into iron observed above 373 K (fig. 5.10). The activation energy for the movement of platinum into iron by radiation enhanced diffusion is found to be about 0.5 eV. At temperatures $\leq$ 423 K platinum is believed to move into iron through a ballistic process. The diffusion coefficients obtained are found to vary from ~ 2×10^{-15} cm^2/s at 298 K to ~ 10^{-14} cm^2/s at 523 K.

The determination of diffusion coefficients for the movement of iron into platinum is extremely difficult, hence a graph such as that in figure 5.7 is constructed. The number of iron atoms crossing over the orignal interface is found to vary linearly with $(dose)^{1/2}$. The slopes of the lines for temperatures $\leq$ 373 K are the same, however the slope increases for temperatures $>$ 473 K. The vacancies in platinum become mobile at about 423 K and the increase in slope for temperatures 423 K is believed to be caused by the vacancy mechanism contributing to the mixing process. The sense and magnitude of the diffusion coefficients of a species under the defect gradients could not be determined. However, it was possible to identify which specie was mobile using the theoretical arguments of Huntington and Seitz (1941), and the ordering mechanism of Liou and Wilkes

(1979). It was found that at a temperature of 473 K and above, part of the mixed film formed an ordered phase, while no ordering was noticed at 373 K and below. Vacancies become mobile at ~ 423 K; hence, it is inferred that ordering and the Pt_3Fe phase formation occurs by the vacancy mechanism. It can be substantiated from the lower temperature data (473 K) that the interstitial mechanism does not contribute to this ordering.

The films mixed above 473 K developed a considerable texture. The grain size of the films was found to increase with dose and temperature. The films mixed at and below 373 K show a number of twins that are believed to be associated with the stress produced in the platinum film via the movement of iron atoms into the platinum film by the interstitial and cascade mechanism. The TEM specimens that were prepared by dissolving the substrate were found bent and wrinkled for those specimens produced at and below 373 K, while the specimens produced above 373 K did not appear to be under any mechanical stress. Platinum-iron bilayers that were annealed at 623 and 673 K show a considerable amount of ordering. In the annealed specimens the atoms can diffuse by the vacancy mechanism and by grain boundary motion. At the temperatures of the anneals, both species are mobile and a considerable amount of the orderd Pt_3Fe phase is observed; also, there is no random relocation process like cascade mixing to disrupt the ordering process. In the mixed samples

the mean grain diameter was found to increase with dose and temperature. The mean grain size increased from ~ 100 Å in the virgin sample to ~ 400 Å at a dose of 20×10^{15} and at temperatures < 373 K. The dependence of mean grain size growth rate on temperature is not large. At a temperature of 523 K and the same dose, the grain size is ~ 480 Å. The grains grow rapidly at first until the dimensions of the grain are about the same size as that of the cascade, for grains much larger than the dimensions of the cascade no grain growth is observed (Thompson D.A. 1986 personal communication)

The phenomenon of grain growth under irradiation may be modelled using equations (2.40). The equations would have to be solved in 3 dimensions assuming that the grain boundaries (gr.b) and the surface act as sinks for the defects. The flux of interstitials and vacancies from two adjacent grains can be calculated using the profiles obtained from the solution of (2.40) and using $J_{i,v} = D_{i,v}(\nabla C_{i,v})_{gr.b}$. The net amount of interstitials and vacancies being absorbed by the grain boundaries from both sides will determine the direction and rate of movement of the grain boundaries. However, it is possible that the highly damaged region near a grain boundary in a grain aligned along a random (high index) direction may 'condense' on to a neighbouring grain which is favourably oriented with respect to the beam. The diffusion model described above does not include this effect, which is likely to be substantial over the tempera-

ture range for which mixing was carried out. A full analysis of such processes is beyond the scope of this work.

A computer program for the simulation of RBS spectra was constructed. The program can simulate an RBS spectrum given a particular composition profile. If the simulated spectrum does not match the experimental one, the program can iterate the composition profile until a satisfactory match is obtained. The amount of platinum and iron sputtered is determined and the composition profiles are shifted to account for the sputtering.

The attempt to produce an electrocatalyst was a qualified success. The mixed electrodes are more stable than the electrodes with evaporated platinum and behave very much like pure platinum electrodes with no hysteresis effects. Iron electrodes have a strong hysteresis effect indicating the formation of an oxide layer. The polarization experiments could be conducted for ~ 48 hours, without contamination problems. During this period the mixed electrodes behave very much like platinum. There is an improvement of about 25% in the overpotential (at 100mA/cm^2) compared to that of pure iron; the improvement in overpotential for pure platinum at the same current density is ~ 36 %.

APPENDIX 1

The computer program RBSSIM presented in this appendix can be used to simulate RBS spectra for a sample containing two elements. The program is divided into eight subroutines and three functions. There are three files that the program requires for data input. The first part of the MAIN program is used to read parameters pertaining to the elements in the target from the file ELEMNT.DAT. These parameters are printed out for the user to check. Should any error be found, the file ELEMNT.DAT would have to be modified. In the rest of MAIN, parameters regarding the detector, beam, energy calibration and the target are read. A factor to change the stopping coefficient can be input. The MAIN then calls SUBROUTINE ENLOS which does most of the numerical work.

ENLOS calculates the energy of the projectile on the way in, till the middle of each layer. The subroutine calls FUNCTION CRO to calculate the cross section of each element (at 1.0 MeV). The backscattering factor for each element is calculated by FUNCTION REL. There are two DO loops; the outer one for the layers and the inner one for the elements in the layer. Here the backscattered yield and energy of the particle is calculated. Each cross section is divided by the

E^2 value to scale for energy. A correction parameter due to L'Ecuyer et al. (1979) for the screening is used to modify the cross section. The subroutine calls ENOUT to calculate the energy of the particle on the way out. FUNCTION EPS is used to calculate the stopping coefficient. Once the yield and energy of the backscattered particle has been determined the subroutine calls SPREDS which uses the data in GAUSS.DAT to spread the counts into a gaussian function, distributing the counts into energy bins. The process is repeated for each layer and element to generate an RBS spectra.

FUNCTION EPS uses the five parameter fit formula available in Chu et al (1979). The Bohr straggling formulation, described in Chu et al. (1979) is used. SUBROUTINE PPREP is used to prepare a data file to plot either the composition profile or the spectra. SUBROUTINE CHQ is used to iterate the composition profile using the experimental spectra as a guide to determine whether the composition in a particular layer is to be increased or decreased. If there is noise in the experimental spectra and the iterated composition is not smoothly varying, the user may smooth the composition profile using a three point smoothing formulation in SUBROUTINE SMO.

The margins required for this document cause the length of a line to be less than that allowed in FORTRAN. Hence a " _ " is used at the begining of a line to indicate the continuation of the previous line.

```
C         programme to simulate R.B.S. spectra for mixing
C       experiments
C
C         input data for target two elements P=evaporated
C       material and
C       F=substrate material A=detector dead layer material
C
C        AP,AF &  AA are the stopping coeffs. for P,F & A
C       respectively
C       PC & FC are the compositions of P & F in each layer
C
        COMMON/STOPPY/AP,AF,AA,TL,PC
        COMMON/BACK/AISO,ABUND
        COMMON/SPEC/AKE,EX,CHY,CC
        DIMENSION AP(6),AF(6),AA(6),TL(50),PC(50),AISO(18),
       1ABUND(18),AKE(310),EX(512),CHY(512),CC(2,50),
        ECAL(5),CHNO(5)
        INTEGER EL,ES,ED,PT,FE,AL,NI,PD,AU
        LOGICAL*1 FAR(15)

C       matrix ake has the gaussian function in matrix form
C       it is read from file GAUSS.DAT

        OPEN (UNIT=1,NAME='GAUSS.DAT',TYPE='OLD',READONLY)
        AKE(1)=0.50000
        READ (1,390) (AKE(I),I=2,301)
390     FORMAT(10(F7.4),2X)
        CLOSE (UNIT=1)

C       the # of iterations is initialized to zero
        ITERAT=0

C         file ELEMNT.DAT has data for the elements e.g.
_atomic weights
C       atomic numbers, stopping coefficients,etc.
C       the file can be expanded to include other elements

11      TYPE 10
10      FORMAT(1X,'DEFAULT DATA INPUT IF MATERIALS ARE',/,
        1X,'ALUMINUM,IRON,PLATINUM,NICKEL,RUTHENIUM   OR
_PALLADIUM')
C     XXXXXXXXXXXXXXXXXXXXXXXXXXXXXXXXXXXXXXXXXXXXXX
C       input from file DK:ELEMNT.DAT
C     XXXXXXXXXXXXXXXXXXXXXXXXXXXXXXXXXXXXXXXXXXXXXX
C
        TYPE 20
20      FORMAT(1X,'INPUT THE EVAPORATED ELEMENTS ATOMIC #')
        ACCEPT 30,IZ1
30      FORMAT(I2)
        OPEN (UNIT=1,NAME='ELEMNT.DAT',TYPE='OLD',READONLY)
35      READ (1,40) EL
```

```
40      FORMAT(A2,70X)
        READ (1,50) (AP(I),I=1,6)
50      FORMAT(6F10.5,2X)
        READ(1,60) IX1
60      FORMAT(I1,71X)
        READ (1,70) (AISO(I),ABUND(I),I=1,IX1)
70      FORMAT(2F14.7)
        READ (1,80) PN
80      FORMAT(E11.4,47X)
        READ (1,90) IPZ
90      FORMAT(I2,70X)
        IF(IPZ.NE.IZ1) GO TO 35
        TYPE 100
100     FORMAT(1X,'INPUT THE SUBSTRATE ELEMENTS ATOMIC #')
        ACCEPT 30,IZ2
        REWIND 1
105     READ (1,40) ES
        READ (1,50) (AF(I),I=1,6)
        READ (1,60) IX2
        READ (1,70) (AISO(I),ABUND(I),I=IX1+1,IX1+IX2)
        READ (1,80) FN
        READ (1,90) IFZ
        IF (IFZ .NE. IZ2) GO TO 105
        TYPE 110
110     FORMAT(1X,'INPUT THE ATOMIC # OF THE DETECTOR DEAD
_LAYER')
        ACCEPT 30,IZ3
        REWIND 1
115     READ (1,40) ED
        READ (1,50) (AA(I),I=1,6)
        READ (1,60) IX3
        READ (1,70) (AISO(I),ABUND(I),I=13,12+IX3)
        READ (1,80) AN
        READ (1,90) IAZ
        IF( IAZ .NE. IZ3) GO TO 115
        CLOSE (UNIT=1)

        ITN=IX1+IX2
        PZ=IPZ
        FZ=IFZ
        AZ=IAZ

C       the data from ELEMNT.DAT is printed out here for the
_user to check
C       the data

        TYPE 120
120     FORMAT(17X,'------ THE STOPPING COEFICIENTS FOLLOW
------')
        TYPE
_130,EL,(AP(I),I=1,6),ES,(AF(I),I=1,6),ED,(AA(I),I=1,6)
```

```
130     FORMAT(3(1X,A2,' : ',F7.4,1X,5(F10.5,1X),/))
        TYPE 140
140     FORMAT(14X,'------ THE ISOTOPE WEIGHTS & ABUNDANCES
_FOLLOW
        1------')
        DO 145 I=1,IX1
        TYPE 150,EL,I,AISO(I),ABUND(I)
150           FORMAT(1X,A2,'   :  ISOTOPE  #  ',I2,'  =
_',F14.7,5X,'ABUNDANCE = '
        1,F7.4)
145     CONTINUE
        DO 155 I=IX1+1,ITN
        TYPE 150,ES,I,AISO(I),ABUND(I)
155     CONTINUE
        DO 165 I=13,12+IX3
        TYPE 150,ED,I,AISO(I),ABUND(I)
165     CONTINUE
        TYPE 160
160     FORMAT(/,5X,'----- THE AT. DENSITIES & AT. NUMBERS
_FOLLOW ----')
        TYPE 170,EL,PN,PZ,ES,FN,FZ,ED,AN,AZ
170     FORMAT(3(1X,A2,' : ',6X,E11.4,10X,F5.1,/))
        TYPE 180
180      FORMAT(1X,'1 ---ALL DATA O.K. --   NO = 1,--- Y=
_C.R.')
        ACCEPT 190,NERR1
190     FORMAT(I1)
        IF(NERR1.EQ.1) GO TO 11

C       input the experimental spectra here

141     TYPE 33
33      FORMAT(1X,'INPUT THE NAME OF THE DATA FILE')
        ACCEPT 34,(FAR(I),I=1,14)
34      FORMAT(14A1)
        OPEN (UNIT=1,NAME=FAR,TYPE='OLD',READONLY)
        READ(1,5)
5       FORMAT(72X)
        READ(1,5)
        DO 37 I=1,510,10
        READ (1,*) IDAM,(EX(J),J=I,I+9)
37      CONTINUE
        TYPE 167
167     FORMAT(1X,'INPUT THE DEAD TIME FOR THE EXPERIMENTAL
_SPECTRA')
        ACCEPT *,DT
        DO 168 I=1,512
        EX(I)=DT*EX(I)
168     CONTINUE
        CLOSE (UNIT=1)
C
```

```
C      XXXXXXXXXXXXXXXXXXXXXXXXXXXXXXXXXXXXXXXXXXXXXXXXXXXX
C       input detector information
C      XXXXXXXXXXXXXXXXXXXXXXXXXXXXXXXXXXXXXXXXXXXXXXXXXXXX
C
195     TYPE 200
200          FORMAT(1X,'FWHM(KEV)                          AREA OF
_DETECTOR(CM2)',/,1X,'DETECT
       1OR    DISTANCE(CM)                                 DETECTOR
_ANGLE(DEG)',/,1X,'WIDTH OF THE DE
       1TECTOR DEAD LAYER(ANGS)')
       ACCEPT *, FWHM,DETAR,DETDIS,THETA,DEDTHK
       SLDANG=(DETAR)/(DETDIS**2.)
       TYPE 210,FWHM,DETAR,DETDIS,SLDANG,THETA,DEDTHK
210          FORMAT(1X,'FWHM=    ',F10.6,19X,'DETECTOR
_AREA=',F10.6,/,1X,'DETECT
       1OR          DISTANCE          =',F10.6,6X,'SOLID
_ANGLE='F10.6,/,1X,'DETECTOR ANGL
       1E= 'F10.6,9X,'DET. DEAD LAYER WIDTH = ',F9.4)
       TYPE 180
       ACCEPT 190,NERR2
       IF(NERR2.EQ.1)GO TO 195
C
C      XXXXXXXXXXXXXXXXXXXXXXXXXXXXXXXXXXXXXXXXXXXXXXXXXXXX
C      input beam information                                X
C      XXXXXXXXXXXXXXXXXXXXXXXXXXXXXXXXXXXXXXXXXXXXXXXXXXXX
C
215    TYPE 220
220    FORMAT(1X,'ENERGY(KEV),      TARGET TILT(DEG),'/,
       11X,'INTEGRATED CURRENT(MIC.COUL.)')
       ACCEPT *,E0,PHI,TMICOU
       TYPE 230,E0,PHI,TMICOU
230    FORMAT(1X,'INITIAL ENERGY= ',F8.3,11X,'TARGET TILT=
_',F8.3,/,1X,
       1'INTEGRATED CURRENT=',F8.3)
       TYPE 180
       ACCEPT 190,NERR3
       IF(NERR3.EQ.1) GO TO 215
C
C      XXXXXXXXXXXXXXXXXXXXXXXXXXXXXXXXXXXXXXXXXXXXXXXXXXXX
C      energy callibration                                   X
C      XXXXXXXXXXXXXXXXXXXXXXXXXXXXXXXXXXXXXXXXXXXXXXXXXXXX
C
235    TYPE 240
240       FORMAT(1X,'INPUT THE # OF CALLIBRATION POINTS
_(MAX.5) THEN C.R.'
       1,/,1X,'ENERGY,CHANNEL # IN PAIRS THEN C.R.')
       ACCEPT 190,NCAL
       DO 245 ICAL=1,NCAL
       ACCEPT *,ECAL(ICAL),CHNO(ICAL)
245    CONTINUE
       TYPE 250,(ECAL(ICAL),CHNO(ICAL),ICAL=1,NCAL)
```

```
250     FORMAT(1X,'ENERGY = ',F7.1,5X,'CHANNEL # = ',F7.2,/)
        TYPE 180
        ACCEPT 190,NERR4
        IF(NERR4.EQ.1) GO TO 235
        THETA=(THETA/180.00)*3.141592653
        PHI=(PHI/180.00)*3.141592653
        CALL CALLIB (ECAL,CHNO,EVKPCH,AOFSET,NCAL)
        TYPE 251,EVKPCH,AOFSET
251             FORMAT(1X,'ENERGY(KEV)   PER   CHANNEL=
_',F10.5,5X,'OFSET= ',F10.5)
C
C      XXXXXXXXXXXXXXXXXXXXXXXXXXXXXXXXXXXXXXXXXX
C       input target information                    X
C       XXXXXXXXXXXXXXXXXXXXXXXXXXXXXXXXXXXXXXXXXX
C
C       Initialize PC & TL matrices
C
        DO 401 I=1,50
        PC(I)=0.0
        TL(I)=0.0
401     CONTINUE

C       Input composition from file 'DK:COMP.DAT'

        TYPE 260
260     FORMAT(1X'INPUT FROM COMPOSITION FILE HIT 1')
        ACCEPT 190,INP
        IF(INP.EQ.0) GO TO 400

        TYPE 33
C33     FORMAT(1X,'INPUT THE NAME OF THE DATA FILE')
        ACCEPT 34,(FAR(I),I=1,14)

        OPEN (UNIT=1,NAME=FAR,TYPE='OLD',READONLY)
        READ (1,320) NL
320     FORMAT(I3)
        DO 335 I=1,NL
        READ (1,330) PC(I),TL(I)
330     FORMAT(2F7.4)
        TL(I)=TL(I)/COS(PHI)
335     CONTINUE
        CLOSE (UNIT=1)
C
C       Check on data input for target composition follows
C
345     TYPE 253,EL
253     FORMAT(1X,'LAYER #',3X,A2,' FRAC',3X,'WIDTH SEEN BY
_BEAM')
        DO 350 I=1,NL
        TYPE 355,I,PC(I),TL(I)
355     FORMAT(2X,I3,5X,F7.4,3X,F7.1)
```

```
350     CONTINUE
        GO TO 543
C
C       To input comp from terminal or change profile
C
400     TYPE 420,NL
420       FORMAT(1X,'THE # OF LAYERS IS ',I3,/,1X,'CHANGE
_COMPOSITION FROM
        1 LAYER N1 TO N2',/,1X'INPUT NEW LAYER # & N1,N2')
        ACCEPT*,NL,NC1,NC2
        YB=0.0
        DO 440 I=1,NL
        IF(I.LT.NC1.OR.I.GT.NC2) GO TO 607
        TYPE 261,I,EL
261      FORMAT(1X,'LAYER #',I2,3X,A2,' FRAC',3X,'WIDTH AS
_SEEN BY BEAM')
        TYPE 262,I,PC(I),TL(I)
262       FORMAT(21X,I3,5X,F7.4,3X,F7.1,/,1X,'INPUT FRAC &
_WIDTH AS
        1 SEEN BY BEAM',$)
        ACCEPT *,PC(I),TL(I)
607     YB=YB+(PC(I)*PN+(1.-PC(I))*FN)*PC(I)*TL(I)*1.0E-8
        TYPE 226,YB
226     FORMAT(1X,'THE CUMULATIVE # OF PT ATOMS= ',E12.4)
440     CONTINUE
        TYPE 263
263     FORMAT(1X,'NEW PROFILE FOLLOWS')
        GO TO 345
543     CONTINUE

C       The target input is over

        TYPE 267,EL,YB
267     FORMAT(1X,'THE # OF ',A2,' ATOMS = ',E12.4,/,1X,'ALL
_DATA O.K.
        1 N==>1 C.R.    Y==>C.R.')
        ACCEPT 190,ILK
        IF(ILK.EQ.1) GO TO 400
C
C         a scaling factor may be input here, the factor
_multiplies with the
C       stopping calculated for the element P, if you do not
_desire to change
C         the stopping by input 1.0, a factor of 1.03 will
_increase the stopping
C       of P by 3%
C
        TYPE 402
402       FORMAT(1X,'input factor to change stopping of
_evaporated element')
        ACCEPT 403,RUMBA
```

```
403     FORMAT(F12.4)

C       Initializing matrix containing simulated spectra

2000    DO 13 I=1,512
        CHY(I)=0.00000
13      CONTINUE

C       calculations to simulate spectra follow

        CALL ENLOS
     _(E0,PZ,FZ,PN,FN,AN,EVKPCH,AOFSET,NL,ITN,THETA,IX1,
       1TMICOU,SLDANG,DEDTHK,FWHM,RUMBA)

C       plotting routines for spectra are called here

        CALL PPREP(2,NL)

C           the yield and channel numbers along with the
     _diviation may be
C       typed here to enable the user to deside weather the
     _simulated spectra
C       acceptable

        TYPE 1022
1022    FORMAT(1X,'DO YOU WANT TO TYPE SPECTRA 1 C.R.')
        ACCEPT 190,KQ
        IF(KQ.EQ.0) GO TO 464
        TYPE 1021
1021    FORMAT(1X,' INPUT THE FIRST,LAST CH # YOU WANT TYPED
     _OUT')
        ACCEPT *,KRAM,KRAM1
        ERL=1.0-ERR
        ERG=1.0+ERR
        DO 1035 I=KRAM,KRAM1
        TYPE 1036,(I,EX(I),CHY(I))
1036    FORMAT(1X,'CH# ',I3,3X,'EXP ',F7.1,3X,'SIM ',F7.1)
        IF(EX(I).LE.1.0) EX(I)=1.0
        RR=CHY(I)/EX(I)
        IF(RR.GT.ERL.AND.RR.LT.ERG) GO TO 1035
        TYPE 1037,I,RR
1037    FORMAT(30X,'CH # = ',I3,3X,'YSIM/YEXP = ',F8.3)
1035    CONTINUE

C           To plot comp profile,create composition file &
     _asimulated spectra

464     TYPE 181
181       FORMAT(1X,'TO CHANGE THE COMP FOR A NEW SPECTRA
     _C.R.',/,
        1X,' TO SAVE CALCULATED SPECTRA 1 C.R.')
```

```
        ACCEPT 190,ICC
        IF(ICC.EQ.1) GO TO 386

C       the value of E0 may be changed here

        TYPE 1000,E0
1000     FORMAT(1X,'THE VALUE OF E0=',F8.2,'TO CHANGE E0 1
_C.R.')
        ACCEPT 190,I1001
        IF(I1001.EQ.0)GO TO 1013
        TYPE 1012
1012    FORMAT(1X,'INPUT THE NEW VALUE OF E0 IN KEV')
        ACCEPT *,E0
        GO TO 2000

C           calls subroutine that changes the composition
_automatically

1013    TYPE 1016,EL,YB,EL
1016    FORMAT(1X,'THE TOTAL # OF ',A2,' ATOMS = ',E12.4,/,
        1X,'TO   CHANGE   CHANNEL   ERROR,   TOTAL   ERROR,
_TOTAL',A2,'1 C.R.')
        ACCEPT 190,I1003
        IF(I1003.EQ.0) GO TO 1005
        TYPE 1015
1015     FORMAT(1X,'INPUT THE CH.  ERROR,TOTAL ERROR,  NEW
_TOTAL',A2,
        1' ATOMS')
        ACCEPT *,ERR,TERR,YB
1005    CALL
 _CHQ(ERR,TERR,YB,E0,EVKPCH,AOFSET,PN,FN,NL,ITERAT)
        GO TO 2000

C       To plot composition spectra

386     TYPE 381
381     FORMAT(1X,'TO PLOT THE COMP. PROFILE  C.R. NO==> 1
_C.R.')
        ACCEPT 190,LC
        IF(LC.EQ.1) GO TO 832
        CALL PPREP (-1,NL)

C       To write spectra memory

832     TYPE 12
12      FORMAT(1X,'TO WRITE SPEC ON DJ: C.R. NO==> 1 C.R.')
        ACCEPT 190,NG
        IF(NG.EQ.1) GO TO 463
        TYPE 392
392     FORMAT(1X,'INPUT THE NAME OF FILE (FILNAM.TYP)',$)
```

```
      ACCEPT 393,(FAR(I),I=1,14)
393   FORMAT(14A1)
      OPEN (UNIT=1,NAME=FAR,TYPE='NEW')
      WRITE (1,394) FWHM,DETAR,DETDIS,THETA,DEDTHK,DT
      WRITE (1,394)
     _TMICOU,E0,CHNO(1),CHNO(2),CHNO(3),CHNO(4)
394   FORMAT(6F9.3)
      DO 14 I=1,510,10
      WRITE(1,380) I,(CHY(J),J=I,I+9)
C     TYPE 380,I,(CHY(J),J=I,I+9)
380   FORMAT(1X,I5.5,2X,10(F5.0,1X))
14    CONTINUE
      I=511
      WRITE(1,16) I,CHY(511),CHY(512)
16    FORMAT(1X,I5.5,2X,F5.0,1X,F5.0)
      CLOSE (UNIT=1)

C     To write composition in memory location

463   TYPE 461
461   FORMAT(1X'TO WRITE COMPOSITION ON [.MARK] C.R. NO==>
     _1 C.R.')
      ACCEPT 190,NH
      IF(NH.EQ.1) GO TO 464
      TYPE 392
      ACCEPT 393,(FAR(I),I=1,14)
      OPEN (UNIT=1,NAME=FAR,TYPE='NEW')
      WRITE(1,320)NL
      DO 465 I=1,NL
      WRITE(1,330)PC(I),TL(I)
465   CONTINUE
      CLOSE(UNIT=1)

C     To try again for another spectra

      TYPE 1014
1014  FORMAT(1X,'DO YOU WANT TO TRY AGAIN 1 C.R.')
      ACCEPT 190,I1014
      IF(I1014.EQ.1) GO TO 141
      STOP
      END
```

```
C       XXXXXXXXXXXXXXXXXXXXXXXXXXXXXXXXXXXXXXXXXXXXXXXXXXXX
C        SUBROUTINE ENLOS CALCULATES ALL THE ENERGY LOSSES
     _BOHR STRAGLING
C        AND THE YIELD
C        XXXXXXXXXXXXXXXXXXXXXXXXXXXXXXXXXXXXXXXXXXXXXXXXXXXX
C
         SUBROUTINE ENLOS
     _(E0,PZ,FZ,PN,FN,AN,EVKPCH,AOFSET,NL,ITN,THETA,
         1IX1,TMICOU,SLDANG,DEDTHK,FWHM, RUMBA)
         COMMON/STOPPY/AP,AF,AA,TL,PC
         COMMON/BACK/AISO,ABUND
         COMMON/SPEC/AKE,EX,CHY,CC
         DIMENSION
     _AP(6),AF(6),AA(6),TL(50),PC(50),AISO(18),ABUND(18),
     _1AKE(310),EX(512),CHY(512),CC(2,50),BKEL(12),CROSS(18),DJ(3
     _)

         BIN=0.0000
         BOUT=0.0000
         PTS=1.0420155E-26*PN*PZ
         FES=1.0420155E-26*FN*FZ
         E=E0
         YFAC=(1.0E5/1.602)*TMICOU*SLDANG
         DO 20 I=1,IX1
         CROSS(I)=CRO(PZ,THETA,AISO(I))
         DJ(I)=0.049*2.0*(PZ**1.33)
20       CONTINUE
         DO 30 I=IX1+1,ITN
         CROSS(I)=CRO(FZ,THETA,AISO(I))
         DJ(I)=0.049*2.0*(FZ**1.33)
30       CONTINUE
         DO 40 I=1,ITN
         BKEL(I)=REL(AISO(I),THETA)
40       CONTINUE
         DO 50 IL=1,NL
         C=PC(IL)
         W=TL(IL)/2.
         ADAV1=C*PN+(1.-C)*FN
         YFAC1=YFAC*ADAV1*2.*W
         S2=((PTS*C/PN)+(FES*(1-C)/FN))*ADAV1
         GIN=S2*W
         GOUT=GIN/COS(3.141592654-THETA)
         BIN=BIN+GIN
         BOUT=BOUT+GOUT
         SPT=EPS(AP,E)*RUMBA
         SFT=EPS(AF,E)
         DELE1=(SPT*C+SFT*(1.-C))*ADAV1*W*1.0E-26
         E=E-DELE1

C        New element
```

```
      DO 60 IT=1,ITN
      TYPE 200,E
200   FORMAT(1X'THE VALUE OF E = ',F12.6)
      IF(IT.GT.IX1) C=1.0-C
      YIELD=(CROSS(IT)/E**2.)*ABUND(IT)*YFACI*C*(1.0-(DJ(
     _IT)/E))
      EBK=E*BKEL(IT)
      BOHR=(BKEL(IT)**2.0)*BIN+BOUT

      CALL ENOUT(IL,EBK,DEDTHK,AN,PN,FN,THETA,RUMBA)

      CC(IT,IL)=(EBK-AOFSET)/EVKPCH

      CALL SPREDS(EBK,YIELD,EVKPCH,AOFSET,FWHM,BOHR)
60    CONTINUE

      E=E-DELE1
      BIN=BIN+GIN
      BOUT=BOUT+GOUT

50    CONTINUE
      RETURN
      END


C     XXXXXXXXXXXXXXXXXXXXXXXXXXXXXXXXXXXXXXXXXXXXXXXXX
C       ENOUT CALCULATES THE ENERGY OF THE PARTICLE ON THE
 WAY OUT     X
C     XXXXXXXXXXXXXXXXXXXXXXXXXXXXXXXXXXXXXXXXXXXXXXXXX
C
      SUBROUTINE ENOUT (IL1,E2,DEDTHK,AN,PN,FN,TH2,RUMBA)
      COMMON/STOPPY/AP,AF,AA,TL,PC
      DIMENSION AP(6),AF(6),AA(6),TL(50),PC(50)
      EK=E2
      TDELE=0.0
      SPT=EPS(AP,E2)*RUMBA
      SFT=EPS(AF,E2)
      W2=TL(IL1)*0.5/COS(3.141592654-TH2)
      ADAV=PC(IL1)*PN+(1.0-PC(IL1))*FN
      DELE=(SPT*PC(IL1)+SFT*(1.-PC(IL1)))*ADAV*W2*1.0E-26
      TDELE=TDELE+DELE
      E2=E2-DELE
      IF(IL1.EQ.1) GO TO 20
      DO 10 I=IL1-1,1,-1
      SPT=EPS(AP,E2)*RUMBA
      SFT=EPS(AF,E2)
      ADAV=PC(I)*PN+(1.0-PC(I))*FN
      W2=TL(I)/COS(3.141592654-TH2)
      DELE=(SPT*PC(I)+SFT*(1.0-PC(I)))*ADAV*W2*1.0E-26
```

```
      TDELE=TDELE+DELE
      E2=E2-DELE
10    CONTINUE
      E2=EK-TDELE
20    SAU=EPS(AA,E2)
      DELAU=AN*SAU*DEDTHK*1.0E-26
      E2=E2-DELAU-14.0
      RETURN
      END


C     XXXXXXXXXXXXXXXXXXXXXXXXXXXXXXXXXXXXXXXXXXXXXXXXX
C       SPREDS TAKES A CERTAIN # OF COUNTS AT A CERTAIN
 ENERGY AND     X
C     SPREADS THEM INTO GAUSSIANS
C     XXXXXXXXXXXXXXXXXXXXXXXXXXXXXXXXXXXXXXXXXXXXXXXXX
C
      SUBROUTINE SPREDS(E,YIELD,EVKPCH,AOFSET,FWHM,BOHR)
      COMMON/SPEC/AKE,EX,CHY,CC
      DIMENSION AKE(310),EX(512),CHY(512),CC(2,50)
13    FIN=300.0
      AOMEGA=(BOHR+(FWHM**2./5.545177443))**0.5
      ISHFT=1
      CH=(E-AOFSET)/EVKPCH
      ICH=CH
      DIFS=CH-ICH
      IF(DIFS.GT.0.5) ICH=ICH+1
      ICHS=ICH
      N=1
65    IF(N.EQ.1) DIF=ABS(ICHS+0.5-CH)
      IF(N.EQ.2) DIF=ABS(ICHS-0.5-CH)
      APHK=0.5000
35    Z=(DIF*EVKPCH/AOMEGA)*100.0
      IF(Z.GT.FIN) GO TO 25
      IZ=Z
      APHI=((AKE(IZ+2)-AKE(IZ+1))*(Z-IZ))+AKE(IZ+1)
      CHY(ICH)=CHY(ICH)+YIELD*ABS(APHI-APHK)
      DIF=DIF+1.000
      ICH=ICH+ISHFT
      APHK=APHI
      GO TO 35
25    N=N+1
      ISHFT=-ISHFT
      ICH=ICHS
      IF(N.LT.3) GO TO 65
      RETURN
      END
```

```
C       XXXXXXXXXXXXXXXXXXXXXXXXXXXXXXXXXXXXXXXXXXXXXXXXXXXX
C        SUBROUTINE FOR ENERGY CALLIBRATION
C        XXXXXXXXXXXXXXXXXXXXXXXXXXXXXXXXXXXXXXXXXXXXXXXXXXXX
C
         SUBROUTINE CALLIB (ECAL,CHNO,EVKPCH,AOFSET,NCAL)
         DIMENSION ECAL(5),CHNO(5)
         T1=0.0
         T2=0.0
         T3=0.0
         T4=0.0
         DO 10 I=1,NCAL
         T1=T1+CHNO(I)*ECAL(I)
         T2=T2+CHNO(I)**2.
         T3=T3+CHNO(I)
         T4=T4+ECAL(I)
10       CONTINUE
         EVKPCH=(NCAL*(T1/T3)-T4)/(NCAL*(T2/T3)-T3)
         AOFSET=(T1-EVKPCH*T2)/T3
         RETURN
         END


C       XXXXXXXXXXXXXXXXXXXXXXXXXXXXXXXXXXXXXXXXXXXXXXXXXXXX
C        FUNCTION REL CALCULATES THE KINEMATIC FACTOR    X
C       XXXXXXXXXXXXXXXXXXXXXXXXXXXXXXXXXXXXXXXXXXXXXXXXXXXX
C
         FUNCTION REL (AWT,THETA)
        REL=((((AWT**2.-(4.*SIN(THETA))**2.)**.5)+(4.*
_COS(THETA))_)/(AWT+1    4.))**2.
         RETURN
         END


C       XXXXXXXXXXXXXXXXXXXXXXXXXXXXXXXXXXXXXXXXXXXXXXXXXXXX
C           FUNCTION EPS CALCULATES THE STOPPING USING THE
_STOPPING          X
C       POLYNOMIALS
C       XXXXXXXXXXXXXXXXXXXXXXXXXXXXXXXXXXXXXXXXXXXXXXXXXXXX
C
         FUNCTION EPS(A,EE)
         DIMENSION A(6)
         F=EE/1000.0
        EPS=A(1)+A(2)*F+A(3)*F**2.+A(4)*F**3.+A(5)*
_F**4.+A(6)*F**5.
         RETURN
         END
```

```
C       XXXXXXXXXXXXXXXXXXXXXXXXXXXXXXXXXXXXXXXXXXXXXXXXXXXX
C            FUNCTION CRO TO CALCULATE THE YIELD FROM A
     PARTICULAR LAYER & AX
C       PARTICULAR ISOTOPE                                    X
C       XXXXXXXXXXXXXXXXXXXXXXXXXXXXXXXXXXXXXXXXXXXXXXXXXXXX
        FUNCTION CRO (ZE,T,AWT)
        R=4./AWT
        R1=(1.-(R*SIN(T))**2.)**.5
        CRO=((ZE*1.4398E-13/SIN(T)**2.)**2.)*
     _((R1+COS(T))**2.)*1.E6/R1
        RETURN
        END


C       XXXXXXXXXXXXXXXXXXXXXXXXXXXXXXXXXXXXXXXXXXXXXXXXXXXX
C       SUBROUTINE F8 PREPARES THE DATA FOR USE IN FOR
     SUROUTINE PLOT        X
C       XXXXXXXXXXXXXXXXXXXXXXXXXXXXXXXXXXXXXXXXXXXXXXXXXXXX
C 2 IS SPECTRA       1 IS COMP PROFILE

        SUBROUTINE PPREP(NCC,NL)
        COMMON/STOPPY/AP,AF,AA,TL,PC
        COMMON/SPEC/AKE,EX,CHY,CC
        INTEGER*4 LAB(7),LABX(7),TITLE(10)
        DIMENSION
     _AP(6),AF(6),AA(6),TL(50),PC(50),AKE(310),EX(512),
        1CHY(512),CC(2,50)
        IESC=27
        TYPE 191,IESC,IESC
191     FORMAT(1X,A1,'Pp','S(E)',A1,'®')
        OPEN (UNIT=1, FILE='DATA.DAT', STATUS='OLD')
        IF(NCC.EQ.1) GO TO 21
        IF(NCC.EQ.2) GO TO 10

C       This part for plotting the comp profile

21      XDMIN=0.0
        XDMAX=1200.0
        DXMAJ=120.0
        DXMIN=30.0
        YDMIN=0.0
        YDMAX=1.0

        DYMAJ=0.1
        DYMIN=0.05

10      TYPE 113
113     FORMAT(1X,'ENTER THE X-AXIS LABEL')
        TYPE 114
114     FORMAT(1X,'12345678901234567890123456789012345678')
        ACCEPT 1115,(LABX(I),I=1,7)
```

```
      TYPE 116
116      FORMAT(1X,'ENTER THE # OF CHARACTERS IN THE X
_LABEL')
      ACCEPT 41,NCHRSX
41    FORMAT(I2)

      TYPE 117
117     FORMAT(1X,'ENTER THE Y AXIS LABEL WITH ONE SPACE
_BETWEEN'
     1 ,/,'EACH CHARACTER')
      TYPE 114
      ACCEPT 1115,(LAB(I),I=1,7)

      TYPE 119
119      FORMAT(1X,'ENTER THE # OF CHARACTERS IN THE Y
_LABEL')
      ACCEPT 41,NCHRS
      IF(NCC.EQ.1)GO TO 20

C     This part for setting up spectra

      XDMIN=400.0
      XDMAX=470.0
      DXMAJ=20.0
      DXMIN=2.0
      TYPE 1000
1000  FORMAT(1X,'TO PLOT ONLY PT PEAK 1 C.R.')
      ACCEPT *,JACK
      IF(JACK.EQ.1) GO TO 1002
      XDMIN=290.0
      XDMAX=470.0
      DXMAJ=20.0
      DXMIN=2.0
1002  YDMIN=0.0
      YDMAX=10000.0
      DYMAJ=1000.0
      DYMIN=500.0

C     Common area for setting up spectra and comp profile

20    WRITE (1,*) XDMIN,XDMAX
31    FORMAT(1X, 2E10.3)
      WRITE(1,*) DXMAJ,DXMIN
      WRITE (1,*) YDMIN,YDMAX
      WRITE (1,*) DYMAJ,DYMIN
      WRITE (1,115) (LABX(I),I=1,7)
115   FORMAT(1X,7A4)
1115  FORMAT(7A4)
      WRITE (1,*) NCHRSX
      WRITE (1,115) (LAB(I),I=1,7)
```

```
      WRITE (1,*) NCHRS
      IF(NCC.EQ.2) GO TO 30

C     Composition profile data input

      WRITE (1,*) NCC
      NL1=3*NL
      WRITE (1,*) NL1
      TO=0.0
      DO 120 I=1,NL
      WRITE (1,*) TO,PC(I)
      TO=TO+TL(I)
      WRITE (1,*) TO,PC(I)
      WRITE (1,*) TO,YDMIN
120   CONTINUE
      GO TO 40

C     This part for spectra data input

30    WRITE (1,*) NCC
      IXDMAX=XDMAX
      IXDMIN=XDMIN
      NDATA=IXDMAX-IXDMIN+1
      WRITE (1,*) NDATA
541   FORMAT(I3)
      DO 130 I=IXDMIN,IXDMAX
      CNO=I*1.0
      WRITE (1,*) CNO,CHY(I)
130   CONTINUE
      WRITE (1,*) NDATA
      DO 131,I=IXDMIN,IXDMAX
      CNO=I*1.0
      WRITE (1,*) CNO,EX(I)
131   CONTINUE


40    TYPE 141
141     FORMAT(1X,'TO SAVE PLOT ON BACKGROUND HIT 1 C.R.
_OTHER CLEAR')
      ACCEPT 190,NHOW
190   FORMAT(I1)
      CLOSE (1)
      CALL PL3(NHOW)
      RETURN
      END
C      this subroutine is used to iterate the composition
_profile

      SUBROUTINE CHQ
_(ERR,TERR,YB,E0,EVKPCH,AOFSET,PN,FN,NL,ITERAT)
      COMMON/STOPPY/AP,AF,AA,TL,PC
```

```
      COMMON/SPEC/AKE,EX,CHY,CC
      DIMENSION
     _AP(6),AF(6),AA(6),TL(50),PC(50),AKE(310),EX(512),
     1CHY(512),CC(2,50)

C     To avoid itterating

      TYPE 40
40    FORMAT(1X,'TO AVOID ITTERATING 1 C.R.')
      ACCEPT *,NOITT
      IF(NOITT.EQ.1) GO TO 500

      ITERAT=ITERAT+1
      TYPE 111,ITERAT
111   FORMAT(1X,'ITERATION # = ',I3)

C     this part canges the CC matrix to integers

      DO 80 I=1,2
      DO 90 J=1,NL
      H=CC(I,J)
      KE=H
      IF((H-KE).GE.0.5) KE=KE+1
      CC(I,J)=KE
90    CONTINUE
80    CONTINUE

C     this part can iterate between channels I1 and I2
C       between I1 and the crossover channel for the peak
     for the element P
C     and between the cross over channel for the element F

      TYPE 10
10    FORMAT(1X,'MODIFY BETWEEN CHANNELS I1 & I2',/,
     11X,'INPUT I1,I2,& ONE CHANNEL BEFORE CROSS OVER')
      ACCEPT *,ISTA,ISTO,ISWT

      DO 20 MCH=ISTA,ISTO,-1
      NUT=0
      DO 30 LAY=1,NL
      IV=CC(1,LAY)
      IF(IV.EQ.MCH) NUT=NUT+1
      IF(IV.EQ.MCH) NB=LAY
30    CONTINUE
      MUM=MCH

      DO 5 LZ=NB,NB-NUT+1,-1
      IF(MUM.GT.ISWT) GO TO 32
      MUM=CC(2,LZ)
      RAT=(EX(MUM)/CHY(MUM))*(1.0-PC(LZ))
      IF(RAT.GT. 1.0) RAT=1.0
```

```
          PC(LZ)=1.0-RAT
          IF(PC(LZ).LT.0) PC(LZ)=0.0
          IF(EX(MUM).LE.0) EX(MUM)=1.0
 32       RAT=CHY(MUM)/EX(MUM)

          IF(RAT.LE.0) RAT=1.0
          PC(LZ)=PC(LZ)/RAT

          IF(PC(LZ).GT.1.0) PC(LZ)=1.0
 5        CONTINUE
          NUT=0.0
 20       CONTINUE

 500      CALL
     _SMO(ERR,TERR,YB,E0,EVKPCH,AOFSET,PN,FN,NL,ITERAT)
          RETURN
          END
 C        subroutine used to display comp spectra & smoth it
          SUBROUTINE
     _SMO(ERR,TERR,YB,E0,EVKPCH,AOFSET,PN,FN,NL,ITERRAT)
          COMMON/STOPPY/AP,AF,AA,TL,PC
          COMMON/SPEC/AKE,EX,CHY;CC
          DIMENSION
     _AP(6),AF(6),AA(6),TL(50),PC(50),AKE(310),EX(512),
          1CHY(512),CC(2,50)

 C        To calculate the total # of atoms

          YBM=0.0
          DO 10 I=1,NL
          YBM=YBM+(PC(I)*PN+(1.0-PC(I))*FN)*PC(I)*TL(I)*1.0E-8
 10       CONTINUE

          CALL PPREP(1,NL)

          TYPE 20
 20       FORMAT(1X,'TO CONTINUE AUTO 1 C.R.',/,
          11X,'FOR MANUAL COMP. CHANGE 2 C.R.')
          TYPE 21
 21       FORMAT(1X,'FOR MANUAL THK CHANGE 3 C.R.',/,
          11X,'FOR SMOTHNING 4 C.R.')
          ACCEPT 30,IJ
 30       FORMAT(I1)
          IF(IJ.EQ.4) GO TO 70
          IF(IJ.EQ.3) GO TO 60
          IF(IJ.EQ.2) GO TO 50
          GO TO 210

 50       TYPE 40,NL
 40       FORMAT(1X,I2,2X,'LAYERS TOTAL',/,
          11X,'CHANGE FROM N1 TO N2 ; INPUT eg: N1,N2')
```

```
      ACCEPT *,NC1,NC2
      TYPE 80
80    FORMAT(1X,'INPUT THE NEW BESIDE THE OLD')
      DO 90 IK=NC1,NC2
      IF(IK.LT.NC1.OR.IK.GT.NC2) GO TO 200
      TYPE 110,IK,PC(IK)
110   FORMAT(1X,'LAY # =',I3,1X,'PT FRAC =',F10.4,2X,$)
      ACCEPT *,PC(IK)
90    CONTINUE

      GO TO 200

60    TYPE 40,NL
      ACCEPT *,NC1,NC2
      TYPE 80
      DO 190 IK1=NC1,NC2
      IF(IK1.LT.NC1.OR.IK1.GT.NC2) GO TO 200
      TYPE 111,IK1,TL(IK1)
111   FORMAT(IX,'LAY # =',I3,1X,'LAY THK =',F10.4,2X,$)
      ACCEPT *,TL(IK1)
190   CONTINUE

      GO TO 200

70    NLN=NL-1
      Y=PC(1)
      DO 120 IY=1,NLN
      YN=(Y+2*PC(IY)+PC(IY+1))/4.0
      Y=PC(IY)
      PC(IY)=YN
120   CONTINUE
      PC(NL)=(Y+3.0*PC(NL))/4.0
      YBA=0.0
      DO 140 I=1,NL
      YBA=YBA+(PC(I)*PN+(1.0-PC(I))*FN)*PC(I)*TL(I)*1.0E-8
140   CONTINUE
      FACT= YBM/YBA
      DO 150 NOR=1,NL
      PC(NOR)=PC(NOR)*FACT
150   CONTINUE
      CALL PPREP (1,NL)
      TYPE 130
130   FORMAT(1X,'TO CONTINUE SMOTH 1 C.R.')
      ACCEPT 30,ISMO
      IF(ISMO.EQ.1) GO TO 70
      GO TO 210

200   CALL PPREP (1,NL)
210   RETURN
      END
```

file GAUSS.DAT; Table from Kreyzig (1979)

```
 0.5040  0.5080  0.5120  0.5160  0.5199  0.5239  0.5279  0.5319
_0.5359 0.5398
 0.5438  0.5478  0.5517  0.5557  0.5596  0.5636  0.5675  0.5714
_0.5753 0.5793
 0.5832  0.5871  0.5910  0.5948  0.5987  0.6026  0.6064  0.6103
_0.6141 0.6179
 0.6217  0.6255  0.6293  0.6331  0.6368  0.6406  0.6443  0.6480
_0.6517 0.6554
...... etc. ......
```

An example of file ELEMNT.DAT FOLLOWS

```
PT
48.78      198.60     -181.1      73.5       -14.38     1.095
1
195.081000     1.0000
 0.6619E+23
78
AL
55.94      0.6773     -4.752     0.3401     0.2662     -0.04046
1
26.981539      1.0000
 0.6022E+23
13
.......
```

To input the target data by COMP.DAT the file should have the number of layers followed by the compostion and layer width all in free format. eg.

```
 3
1.000   30.0
0.900   40.0
0.800   40.0
```

Two simulations of spectra are included as an example. Figure A1 (a) contains a simulated spectrum of the experimental spectrum mixed at 298 K and mixed with a dose of 4.5×10^{15} Fe^{+}/cm^{2}. Figure A1 (b) is a the composition profile used to generate fig. A1 (a). Figure A2 (a) contains a simulated spectrum of the experimental spectrum mixed at 523 K with a dose of 17.3×10^{15} Fe^{+}/cm^{2}. The full width half maximum used was 19.84 keV and the initial energy of the beam for fig. A1 (a) was 1993.0 keV and for fig. A2 (a) 1994.0 keV. The solid angle of the detector was .0026 steradians. The figures show a close match between the simulated and experimental spectra.

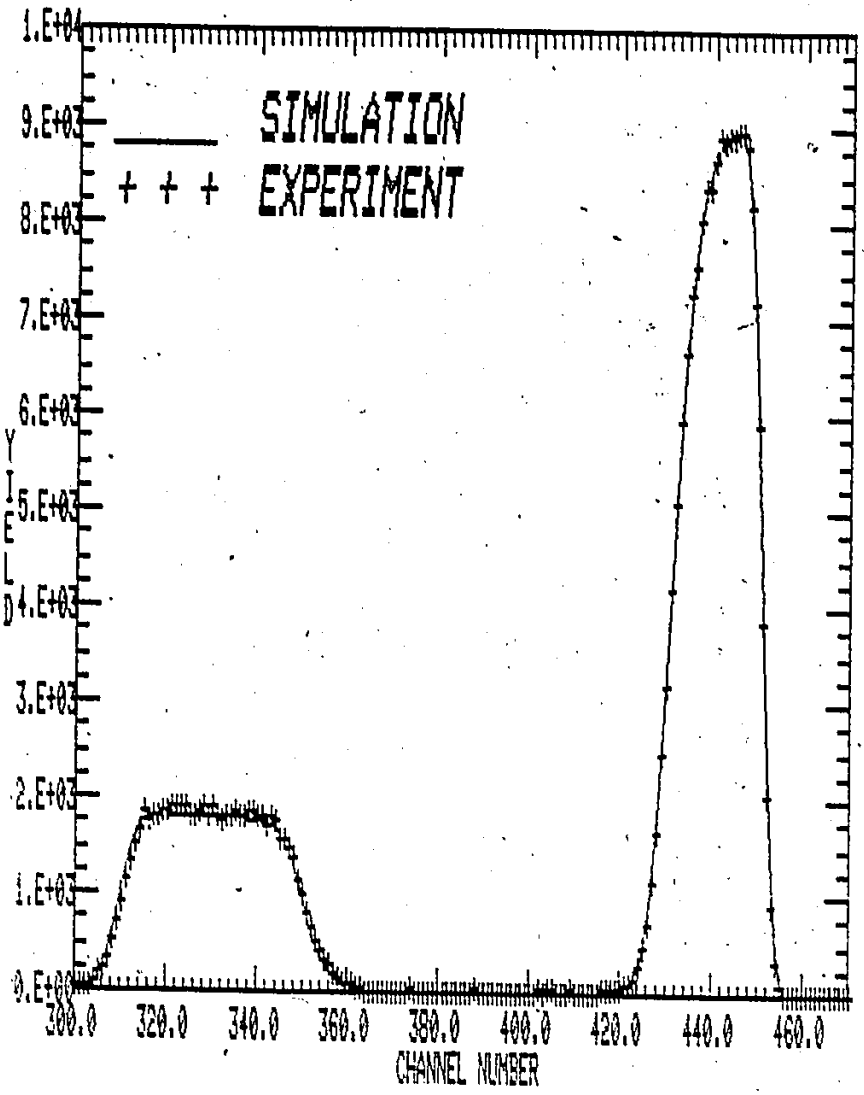

Figure A1 (a) Experimental and simulated RBS spectra.

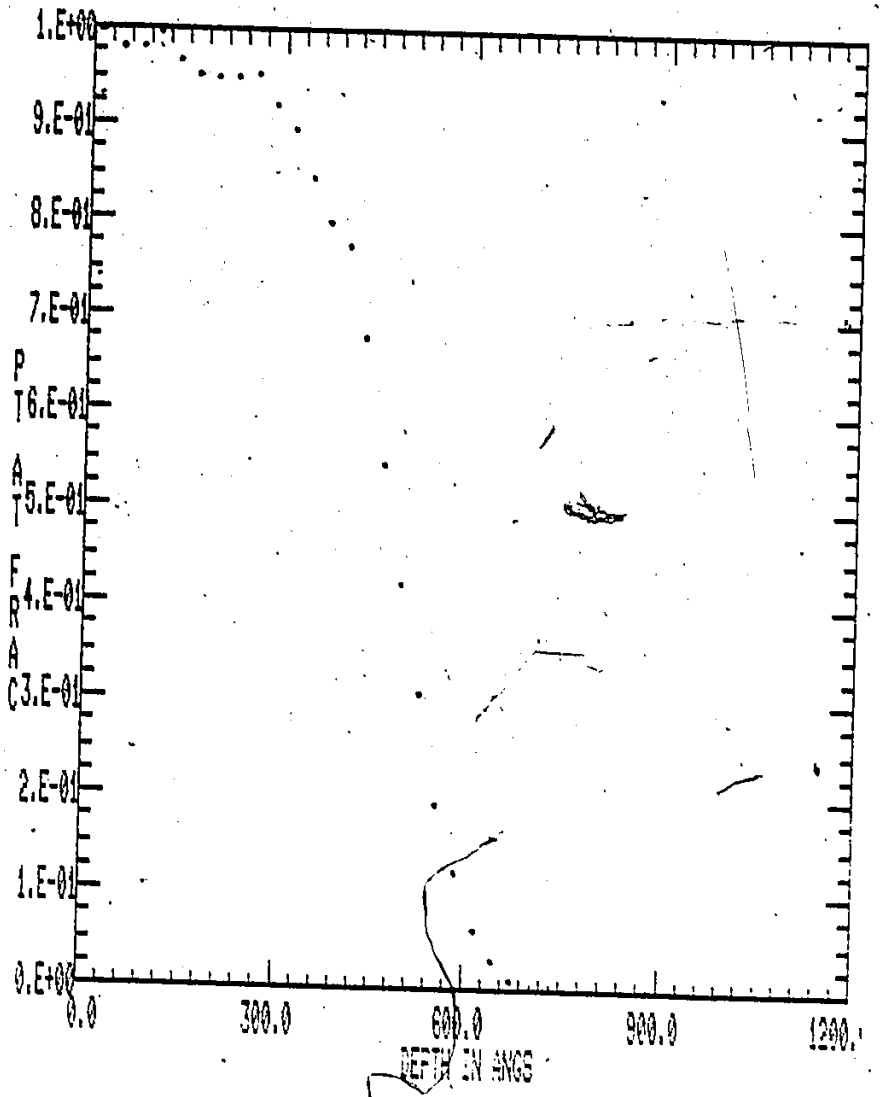

Figure A1 (b) Composition profile used to simulate spectra in fig. A1 (a)

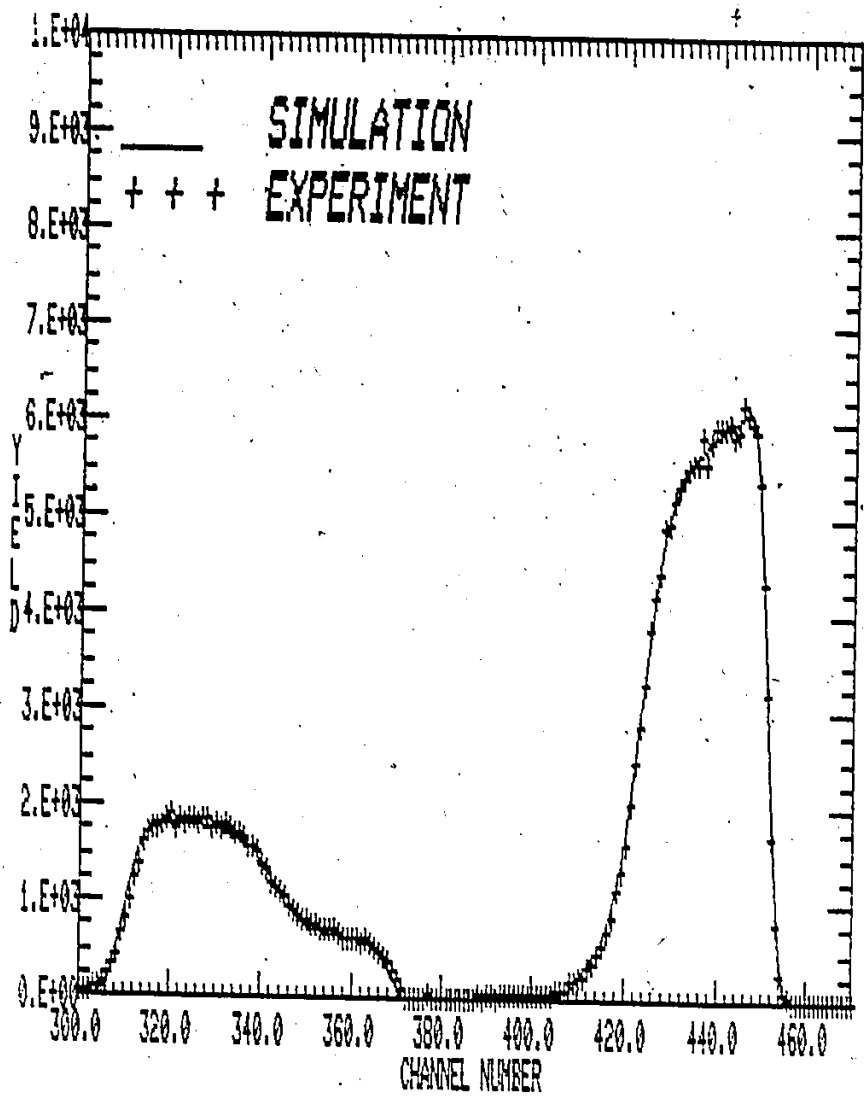

Figure A2 (a) Experimental and simulated RBS spectra.

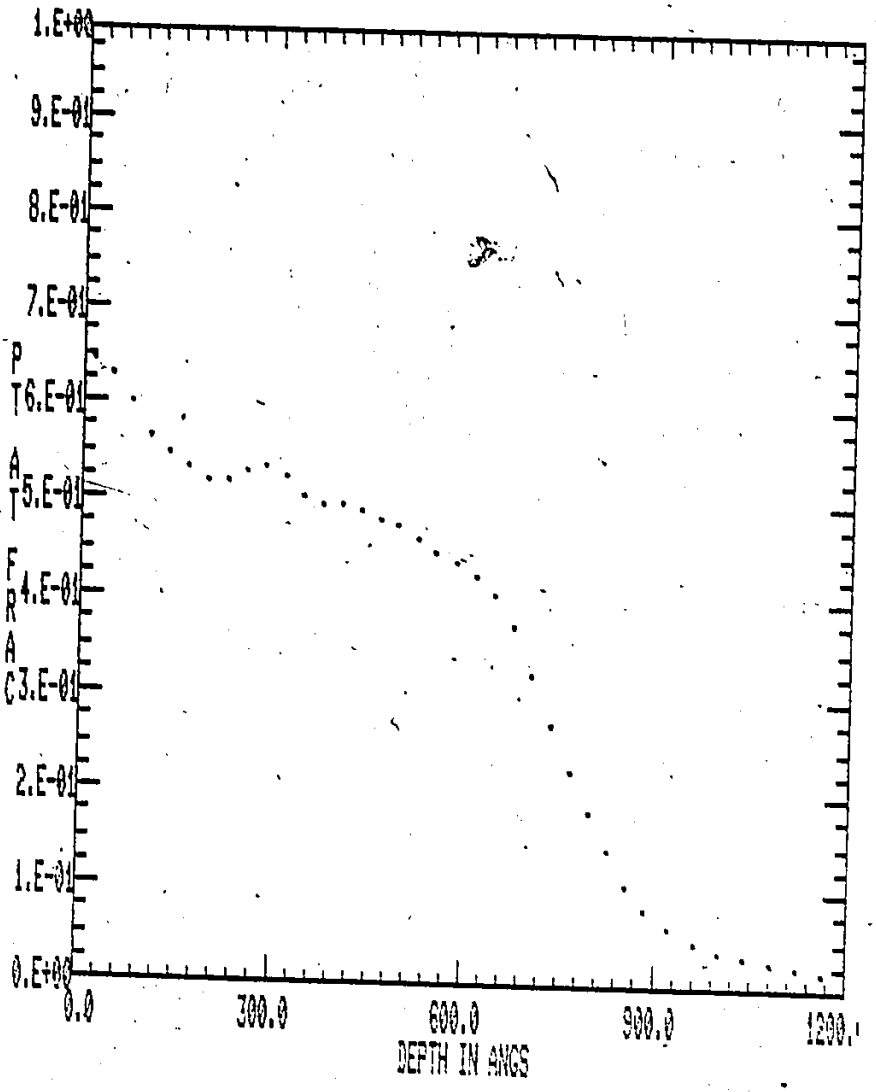

figure A2 (b) Composition profile used to simulate spectra in fig. A2 (a)

REFERENCES

Akano U, Davies J , Smeltzer W, Tashlykov I , Thompson D, Nucl. Inst. and Meth. 182/183, p985, (1981)

Averback R S, Nucl. Inst and Meth. B15, p675 (1986)

Baroody ,J. Appl. Phys. 36, 11, p3565 (1965)

Battaglin G, Carnera A, Celotti G, Della Mea G, Kulkarni V N, Lo Russo S and Mazzoldi P, Mat. Res. Soc. Symp. Proc. Vol. 27, p50, (1984)

Bockris J O'M, and Potter E C, J. Electrochem. Soc. Vol. 99, p169, (1952)

Bockris J O'M, and Reddy A K, Modern Electrochemistry Vol 2. Plenum Press, N.Y. (1970)

Bockris J O'M, and Srinivasan S, (a) Vol. 111, p845 (1964)

Bockris J O'M, and Srinivasan S, (b) Vol. 111, p862 (1964)

Bockris J O'M, and Srinivasan S, (c) Vol. 111, p858 (1964)

Bockris J O'M, and Srinivasan S, (1964) referenced in Srinivasan et al. (1967)

Bottiger J, Nielsen S K, Whitlow H J, Wriedt P, Nucl. Inst. and Meth. 218, p684, (1983)

Bottiger J, Davies J A, Sigmund P, and Winterbon K B, Rad. Eff. 11, 69, (1971)

Brimhall J L, Kissinger H E, Charlot L A, Rad. Eff. 77, p237, (1983)

Chu W-K, Mayer J W, Nicolet M-A, Backscattering Spectrometry Academic Press Inc. (1978)

Collins R, Jiminez-Rodrigues J J, Marsh T, Nucl. Inst. and Meth. B7/8, p632, (1985)

Conway B E, and Bockris J O'M, J. Chem. Phys. 26, #3, p532, (1957)

Davies J, McIntyre J D, Cushing R L, Lounsbury M, Can. J. Chem. 38, 1535, (1960)

Davies J and Sims G A, Can. J. Chem. 39, 601, (1961)

Eyring H, Glasstone S, Laidler K J, J. Chem. Phys. Vol. 7, p1053, (1939)

Fisher G, Carter G, Webb R, Rad. Eff. 38, 81, (1978)

Frank W, Seeger A, Rad. Eff. 31, p7, (1976)

Frank W, Seeger A, Schindler R, Rad. Eff. 40, p239, (1979)

Goldstein H, Classical Mechanics, Addison-Wesley 2nd ed. (1980).

Grant W A, in Application of Ion Beams to Materials. ed. Carter G. Colligon J S, and Grant W A, (1981)

Grenness M, Thompson M W, Cahn R W, J. Appl. Electrochem. 4, p211, (1974)

Haff P K, and Switkowski Z E, J. Appl. Phys. 48, 8, 3383, (1977).

Harris J M, and Nicolet M-A, Vol. 11, Phys. Rev. B #3, (1975)

Hayes M, Kuhn A T, Grant W A, referenced in Application of Ion Beams to Materials. ed. Carter G. Colligon J S, Grant W A, (1975)

Howard R E, and Lidiard A B, Phil. Mag. 11, 1179, (1965)

Huntington H B, Phys. Rev. 91, p1092, (1953)

Huntington H B, and Seitz F, Physical Rev. Vol 61, p315 (1942)

Jacucci G, Nontraditional Methods in Diffusion, Conf. Procd. The Metallurgical Soc. of AIME (1984)

Johnson R A, and Brown E, Phys. Rev. 127, p446 (1962)

Johnson R A, and Lam N Q, Phys. Rev. B 13, 10, p4364, (1976)

Johnson W L, Cheng Y T, Van Rossum M, Nicolet M-A, Nucl. Inst. and Meth. B7/8, p657, (1985)

Kendall M G, Advanced Theory of Statistics Vol. 1 (1969)

Kasten H, and Wolf G K, Elec. Acta. 25, p1581, (1980)

Kinchin G H and Pease R S, Rep. Prog. Phys. 18(1), 143, (1955)

Kreyzig E, Advanced Engineering Mathematics, John Wiley, 4th Ed. (1979)

Kuhn A T, Wright P M, J. Electroanal. Chem. 38, p291 (1972)

Lam N Q, and Rothman S J, in Radiation Damage in Metals and Alloys, ed. Peterson and Harkness, p125 (1975)

Lau S S, Liu B X, Nicolet M-A, 209/210 p97 (1983)

L'Ecuyer J, Matsunami N, Davies J A, Nucl. Inst. and Meth. 160, 337, (1979)

Lindhard J, Nilsen V, Scharff M, Dan. Vid. Sel. Mat. Med. 86, 10 (1986)

Lindhard J, Scharff M, Schiott H E, Dan. Vid. Sel. Mat. Med. 33, 14 (1963)

Lindhard J, Nielsen V, Scharff M, Thomsen P V, Dan. Vid. Sel. Mat. Med. 33, 10 (1963)

Liou K Y, Wilkes P, J. Nucl. Mater. 87, p317, (1979)

Manning I, Mat. Res. Soc. Symp. Proc. 27, p91, (1984)

Matteson S, Nicolet M-A, Ann. Rev. Mat. Sci. 13, 339, (1983)

Mayer J W, Tsaur B Y, Lau S S, Hung L-S, Nucl. Inst. and Meth. 182/183, p1, (1981)

Metals Handbook, Vol 8, American Society of Metals, (1963)

Moller W, Nucl. Inst. and Meth. B15, p688, (1986)

Murch G E, Rothman S J, Nontraditional Methods in Diffusion, Conf. Procd. The Metallurgical Soc. of AIME (1984)

Myers S M, Nicl. Inst. and Meth. 168, p265 (1980)

Neeley H H, and Keefer D W, Phys. Stat. Sol. 24, p217, (1979)

Nelson R S, Rad. Eff. 2, 49, (1969)

Oen O S, Holmes D K, Robinson M T, 1963 J. Appl. Phys. 34, 2, 302 (1963)

Paine B M, Nicolet M-A, Banwell T C, MRS, Vol 7, pg. 79, (1982)

Parsons , Trans. Far. Soc. 54, p1053, (1958)

Picraux S T, Follstaedt P M, Delafond J, MRS, Vol. 7 pg. 71, (1982)

Pourbaix M J N, Atlas of Electrochemical Equilibria in Aquous Solutions. NACE (1974)

Robinson M T, Torrens I M, Phys. Rev. B 9, 12, 5008.

Seeger A, and Frank W, Rad. Eff, 31, p17, (1976)

Sigmund P, Rad. Eff. 1, 15-18, (1969)

Sigmund P, Rev, Roum. Phys. Tome. 17, 9 , 1079 (1972)

Sigmund P, Grass-Marti A, Nucl. Inst. Met. 182/183, p25, (1981).

Silverman D C, Corrosion NACE Vol. 38, #8, p453, (1982)

Smittell, Metals Reference Handbook (1983)

Srinivasan S, Wroblowa H, Bockris J O'M, Adv. Catalysis 17, p351, (1967)

Swanson M L, Parsons J R, Hoelke C W, Rad. Eff. 9, p249, (1971)

Takamura S, Rad. Eff. Let. 43, p69 (1979)

Thompson D A, Akano U, Davies J A, Smeltzer W W, in Ion Implantation into Metals. ed. Ashworth et. al. Permagon Press. (1982)

Tsaur B Y, Lau S S, Hung L S, Mayer J W, Nucl. Inst. and Meth. 182/183 p67, (1981)

Voinov M, Buhler D, Tannenberger H, Proc. Electrochem. Soc. San Fransisco (1974).

Wait T R, Phys. Rev. 107, #2, p463, (1957)

Westendorp H, Wang Z C, Saris F W, Nucl. Inst. and Meth. 194, p453, (1982)

Winterbon K B, Ion Implantation Range and Energy Deposition Distribution Vol. 2, Plenium Data Co. (1975)

Winterbon K B, Sigmund P, Sanders J B, Dan. Vid. Sel. Mat. Med. 37, 14 (1970)

Wollenberger H J, in Vacancies and Interstitials in Metals, ed. Seeger, Schumacher, Schilling and Diehl. North Holland (1970)

Ziegler J F, Biersack J P, Littmark U, The Stopping and Ranges of Ions in Matter, Pergamon Press (1985)